Observational diagnostics of 3D radiation-MHD simulations of solar and stellar atmospheres

Dissertation
zur Erlangung des Doktorgrades
der Mathematisch-Naturwissenschaftlichen Fakultäten
der Georg-August-Universität zu Göttingen

vorgelegt von
Lotfi Yelles Chaouche
aus Tlemcen, Algerien

Göttingen 2008

Contents

Summary

The increasing realism of 3D radiative MHD simulations provides a unique laboratory of solar photospheric processes. In order to confront these simulations with observations, observables have to be computed, including spectropolarimetric quantities, which provide the most powerful tool for probing the properties of solar magnetoconvection. The study of spectropolarimetric properties of electromagnetic waves originating in a realistic simulated solar photosphere allows us to identify suitable diagnostics of the various solar phenomena resulting from the interaction between the plasma and the magnetic field in the photosphere and sub-photospheric layers. In addition, the comparison of the spectropolarimetric properties of light originating from MHD simulations and from actual solar observations allows us to get a better insight into the fascinating and complex photospheric phenomena. In this thesis we have studied the following subjects :

- Small scale magnetic flux concentrations are often modelled as some form of flux tube or flux sheet, having respectively, axial and translational symmetries. A common representation of these flux tubes/sheets is given by the thin flux tube/sheet approximation. We have made a comparative analysis between these forms of models and flux concentrations existing in 3D radiative MHD simulations. We found that the second-order thin flux tube/sheet models are consistent with the fluxtubes/sheets obtained in the MHD simulations.

- A powerful way of studying the properties of magnetic flux concentrations in the photosphere is to observe them near the solar limb. In this situation rays cross flux elements obliquely thus sampling these flux elements laterally. Together with observations at disc center, this allows to better constrain models aiming to represent these flux concentrations and their surrounding plasma. We make a spectropolarimetric study of magnetic elements in 3D MHD simulations at disc center and at a heliocentric angle $\theta = 67°$ ($\mu = \cos\theta$=0.39). We investigate the dependence of the sign of the Stokes-V area asymmetry on the gradients of the line-of-sight components of the velocity and magnetic field. The amplitude asymmetry of the average simulated Stokes-V profile is larger than its area asymmetry. These asymmetries are positive at disc center and negative at μ=0.39. The distribution of the simulated Stokes-V area asymmetry across a magnetic element at disc center is close to the observed one by Hinode's SP.

- We compare the spectropolarimetric signal obtained from simulations with the observed one at μ=0.39. The comparison is made possible by degrading the spectral and spatial resolutions of the simulated signal to mimic the observation conditions. We find that observations are reproduced by simulations with average field strength

varying between 200G and 400G. The magnetic flux is mainly distributed over kilo-Gauss flux elements situated in intergranular lanes.

- Flux emergence into the photosphere is studied by analysing the spectropolarimetric signal obtained from MHD simulations of a buoyant rise of a flux rope into the photosphere. We identify some aspects of the spectropolarimetric signature of this rising event over a time-sequence of snapshots. Following observational procedures we degrade the simulated signal to observation conditions and apply a Milne-Eddington inversion to obtain atmospheric parameters. Comparison with observations reveals that the magnetic field strength and upflow velocity of the observed emerging flux are reasonably well reproduced by the MHD model, whereas the amount of twist applied in the simulations was higher than the one in the considered observations.

1 Introduction

The sun is the star in the center of our solar system. It is the only star on which we can resolve physical processes down to some important scales. The magnetic field plays a key role in solar physics. It is what makes the sun an "active" star. It results in a large variety of fascinating phenomena like: sunspots, faculae, prominences, coronal loops, etc. The magnetic field is generated by hydromagnetic dynamo processes (Ossendrijver 2003) in the presence of differential rotation, turbulent convection, and meridional flows. The most likely location for the intensification of the large-scale azimuthal magnetic field is the tachocline region at the bottom of the convection zone, where there is strong radial and azimuthal differential rotation (Thompson et al. 2003). The intensified azimuthal magnetic fields are then transported to the solar surface and atmosphere through the buoyant rise of Parker-unstable magnetic flux tubes (Fan 2004, and references therein).

1.1 The solar atmosphere

The solar atmosphere is the outermost part of the sun. There, photons can escape to the interstellar medium. Conventionally, the solar atmosphere is divided into three layers : the photosphere, the chromosphere and the corona. One way of quantitatively defining these layers is to look at the altitude distribution of the average kinetic temperature through the solar atmosphere (Gray 2005). We focus here only on the photosphere, which is the layer indicated by the shaded region in Figure 1.1

The photosphere is the lowest layer of the solar atmosphere. Its thickness is only a few hundred kilometers, but most photons escaping from the sun are coming from this region. This is due to a relatively sharp increase of photon mean free path in the photosphere comparing to the underlying sub-photospheric layers. The escaping photons carry information about the plasma they interacted with (see chapter 2). Analysing the photospheric radiation allows us to diagnose about the properties of the plasma in this layer. Here we carry out spectro-polarimetric diagnostics. This means we not only investigate the spectral properties of the electromagnetic radiations but also their polarization state which is encoded in the electric field vector of the radiation. The polarization in the photosphere is mainly introduced by the Zeeman effect. This will allow us to probe the dynamics and properties of magnetic flux elements in the solar plasma via the theory of radiative transfer of polarized light.
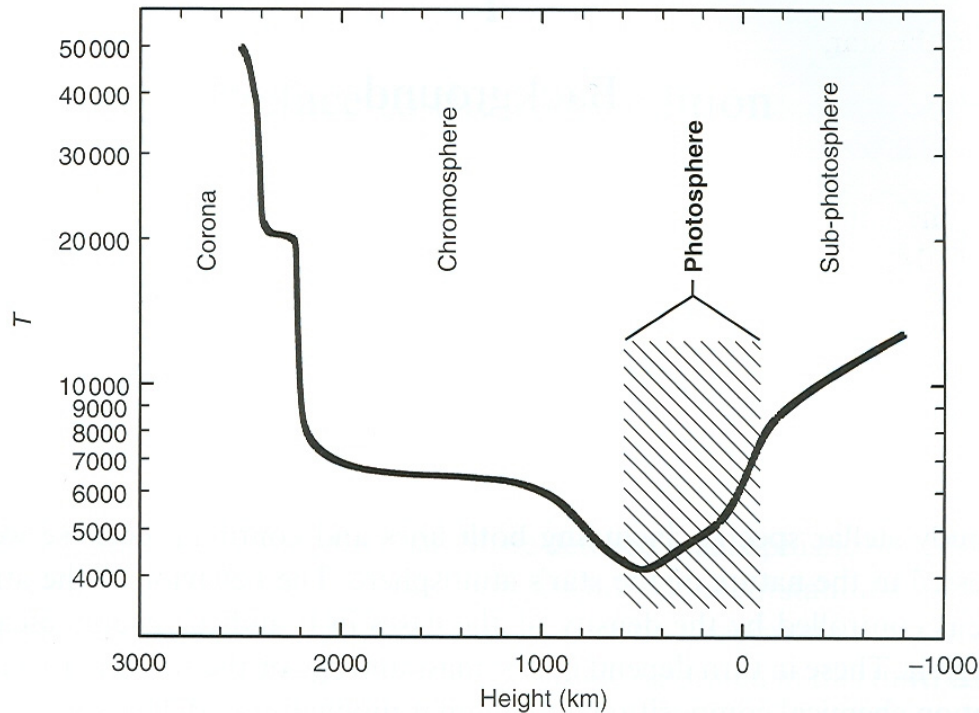
Figure 1.1: The height distribution of temperature in the outer layers of the sun. The height is given in kilometers measured from a zero point where the average optical depth $< \tau_{5000} > = 1$. The photosphere is indicated by the shaded region. Adapted from Gray 2005, based on the work of Vernazza et al. (1973).

1.2   Photospheric magnetic phenomena

Magnetic features covering a wide variety of sizes are observed in the photosphere. Their related magnetic flux varies by six orders of magnitude between the smallest and the largest of these phenomena (Solanki 2001). For convenience we can split these magnetic manifestations into two categories : 1/ sunspots, 2/ small-scale magnetic field elements

Sunspots are the most readily visible manifestations of the interaction between solar magnetic field and the solar plasma (Solanki et al. 2006). They have been systematically observed and studied since about 400 years, starting with the first solar observations using a telescope in 1611 by Galilei and others. The first evidence of their magnetic nature was revealed by Hale (1908) who measured the Zeeman splitting of spectral lines. Sunspots are constituted by a dark central part called the umbra (see Figure 1.2), surrounded by a brighter region characterized by an organized filamentary structure called the penumbra. For recent reviews on sunspots, see Thomas and Weiss (1992) and Solanki (2003).

Small scale magnetic features contain most of the solar magnetic flux. Using line ratio technique Frazier and Stenflo (1972), and Howard and Stenflo (1972) have determined that more than 90 percent of the solar magnetic flux is contained in small-scale magnetic features. They are concentrated mainly in active regions and in the network (the latter found all over the sun) outlining the supergranular cells. These flux concentrations have
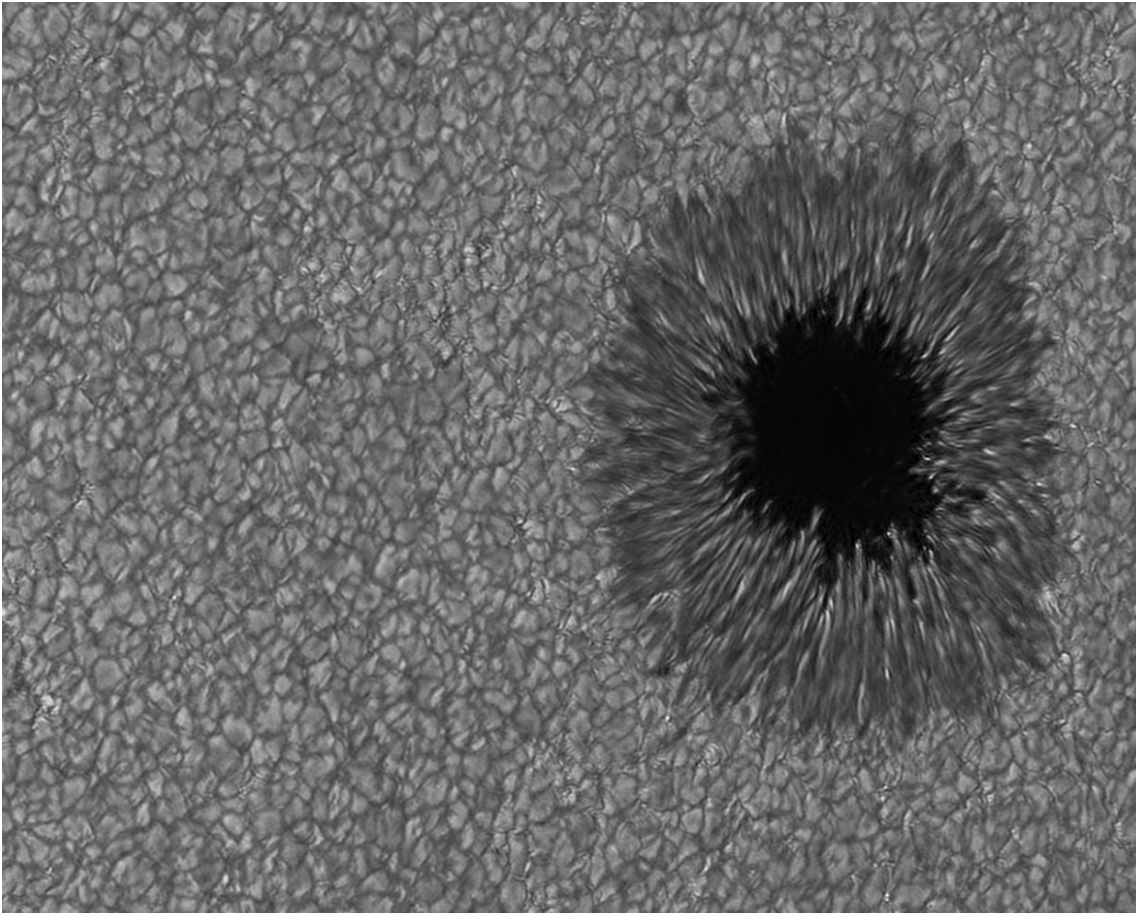
Figure 1.2: Continuum image of a sunspot taken with the Dutch Open Telescope (DOT) operating on La Palma, Tenerife. The image was taken in the blue continuum (around 432nm). The image was downloaded from the DOT website

typically field strengths larger than a kilogauss (Stenflo 1973, Wiehr 1978, Rabin 1992, Rüedi et al. 1992, Martínez Pillet et al. 1997), for reviews see (Solanki 1993, 2003). Part of the magnetic field is also forming the so called internetwork elements, which are located in the interiors of supergranular cells. There is also observational evidence of omnipresent turbulent (i.e., randomly oriented on small scales) field of few tens of gauss (Faurobert-Scholl et al. 1995, Faurobert et al. 2001, Trujillo Bueno et al. 2004). These last references have used Hanle depolarization as a diagnostic tool for determining the magnetic field properties (Stenflo 1994). More recent observations using Hinode's SP and Zeeman diagnostic (Lites et al. 2008) have revealed the presence of an average horizontal magnetic field five times larger than the vertical one. These differences suggest the need of higher spatial resolution and more realistic simulations in order to better understand the quiet sun internetwork magnetic field (e.g. Schüssler and Vögler 2008).

1.3   Modelling the solar photospheric features

The photosphere is constituted of electrically conducting plasma. Thus the magnetic field couples to the plasma. The wide variety of magnetic phenomena observed at the photosphere is described by the MHD equations (including a proper treatment of energy transport by radiation). Under some simplifications, it is possible to model photospheric features using an analytical approach. This has revealed some physical processes governing photospheric phenomena (e.g. Chaouche and Abdelatif 2005). Nevertheless the dynamical, three dimensional, and structured nature of the photospheric phenomena makes it necessary to use more elaborate, invariably numerical models in order to capture the complex nature of the considered photospheric features.

The numerical models exhibit a large variety of assumptions and simplifications, making a trade-off between including the necessary physics (which complicates the model) and applying some suitable simplifications due to the limitation in computing resources and available algorithms. We can distinguish two main numerical modelling approaches: empirical (or semi-empirical) models and self consistent MHD models.

The first approach considers empirical or semi-empirical models. In this approach, a model atmosphere with some free parameters (like temperature stratifications, density, etc.) is assumed. These free parameters are adjusted to fit observational data. This is done usually by inversion techniques. Empirical models with increasing sophistication levels have allowed to construct models of various photospheric features. These play a key role in understanding the solar atmosphere (Vernazza et al. 1976, Solanki and Stenflo 1985, Solanki 1986, Fontenla et al. 1990, Solanki et al. 1991). For a review about small scale flux concentrations see Solanki (1993) and Solanki et al. (2006). For reviews about sunspots see Thomas and Weiss (1992), Solanki (2003), Solanki et al. (2006).

The second approach consists of solving numerically the MHD equations, including as much physical processes as possible. One version of these models assumes that magnetic flux elements are represented by magnetic flux tubes or flux slabs, having respectively an axial or translational symmetry (also true for empirical models). These come from solutions of the MHD equations at low order (Defouw 1976, Roberts and Webb 1979, Spruit 1981). This modelling approach is widely used (see Solanki et al. 2006, for a review). Flux tube models are still successfully used (e.g. Khomenko et al. 2008). This last reference presents a study of some properties of magneto-acoustic waves in a vertical flux tube. Due to the 3D nature and the many physical processes involved in photospheric phenomena, a more self consistent way of modelling photospheric features involves using numerical solutions of the MHD equations that are not limited by restrictions to certain symmetries, etc. This is done including as many realistic aspects as possible, like including a proper treatment of radiative energy exchange, and partial ionization of chemical elements. 3D simulations of solar granulation were first carried out by Nordlund (1982). This has been followed by an increasingly large body of work owing to the increasing computing resources and the attractive success of these models (for reviews, see Schüssler 2001, Schüssler and Knölker 2001). In the last few years, realistic magneto-convection simulations have been successfully carried out for studying different photospheric magnetic phenomena and physical processes: Solar surface dynamo (Vögler and Schüssler 2007), flux tube emergence at the solar surface (Cheung et al. 2007, 2008), the formation and evolution of umbral dots (Schüssler and Vögler 2006), the structure

and internal dynamics of a pore (Cameron et al. 2007). Comparison of these simulations with observational data allows to validate the findings of these numerical studies or to determine their shortcomings. Studying the spectropolarimetric properties of the Stokes profiles emerging from a simulated atmosphere and comparing them with observations is the best way of determining similarities and differences between the simulated and observed phenomena. E.g. Schüssler et al. (2003) and Shelyag et al. (2004), have carried out a spectral synthesis of the G-band spectrum emerging of a 3D radiative MHD simulation, and compared it with observations. This has been successful in explaining the origin of G-band bright points. Khomenko et al. (2005) have carried out a comparison between the observed and synthesized (from 3D MHD simulations) Stokes signal for Fe I spectral lines at 6301.5, 6302.5, 15648 and 15652 Å for several simulations with average field strengths ranging from 10 to 140 Gauss. They found that the synthetic spectra show many properties in common with the observed ones. Nevertheless, they pointed out that the seeing conditions affect the resulting Stokes spectra leading to different possible diagnostic, of the same data, depending on the degrading seeing conditions.

The advent of 3D radiative MHD simulations with a high degree of sophistication including a non-grey and non-local treatment of radiative energy exchange (see MURaM code Vögler et al. 2005), raises some key questions:

As mentioned earlier there exists a large body of work explaining some aspect of photospheric flux elements using the concept of thin flux tube or flux slab. How do these models compare with 3D MHD simulations? This is a key question which may clarify the validity of some widely used empirical and numerical models. In order to find an answer to this question we will compute thin flux tube and thin flux sheet models and compare them with magnetic flux elements existing in high resolution MHD simulations. This will be done in chapter 3.

Another fundamental question is: to what extent do the 3D radiation MHD simulations reproduce photospheric phenomena? To address this question, we need to make a comparison between the simulations and spectropolarimetric observations. We have analysed two simulation scenarios. The first one (chapter 4) aims to study the spectropolarimetric properties of small scale flux elements at disc-center and near the solar limb. The emerging Stokes spectra from such simulations have been calculated using the STOPRO code in the SPINOR package (Solanki 1987, Frutiger et al. 2000). This allows us to study the line formation process in a realistic atmosphere. Then, in order to compare these synthesized Stokes spectra with spectropolarimetric observations, we reduce the spatial and spectral resolution of the synthetic Stokes spectra to make them comparable with those of the observations. The comparison is presented in section 4 of the fourth chapter. The second simulation scenario will be analysed in chapter 5. It considers a flux tube emerging into the solar photosphere (Cheung et al. 2007). From an observational point of view, the properties of flux emergence have been studied since a few decades (Brants 1985a,b). Our aim is to determine the spectropolarimetric signature of the simulated flux emergence event and discuss it in terms of its origin in the MHD simulations. In order to define similarities and differences between the simulations and the actual flux emergence in the solar photosphere, we perform a comparison of the synthetic spectropolarimetric data with recorded observations.

2 Radiative transfer in a magnetized medium under Zeeman regime

2.1 Introduction

A spectral line results from the interaction of an electromagnetic wave with a quantum system (usually atoms, ions or molecules). In an astrophysical context the ensemble of quantum systems appears macroscopically often as a plasma. The resulting spectral line will be affected by the characteristics of the atoms or other constituents of the plasma interacting with the electromagnetic wave. In the presence of a magnetic field, the spectral lines may exhibit some polarization properties. In the next sections we will discuss the processes producing an atomic spectral line in a magnetized plasma. The first section is dedicated to the effect of the magnetic field on spectral line formation in the Zeeman regime. The absorbtion and dispersion of electromagnetic waves in a plasma will be discussed in the second section. The transfer of a polarized electromagnetic wave is described by a transport equation developed by Unno (1956) and further by Rachkovsky (1962). This radiative transfer equation will be treated in the last section.

2.2 The Zeeman effect

The Zeeman effect is the splitting of spectral lines into several components in the presence of an external magnetic filed. It was fist recorded by Pieter Zeeman in 1896. An early attempt to explain the origin of the Zeeman effect was given by Lorentz in term of the classical Larmor's precession theory. The quantum mechanical approach offers a more adequate and general explanation of the Zeeman effect (e.g. the text book by Cohen-Tannoudji et al. 1973). The splitting of spectral lines into several components is due to a change in energy levels of the electrons involved in the quantum transitions. To understand that, we turn to the Hamiltonian characterizing an electron bound to an atom in the presence of an external magnetic field.

$$\mathbf{H} = \mathbf{H_0} + \mathbf{H_M}, \tag{2.1}$$

where $\mathbf{H_0}$ is the Hamiltonian of the system without magnetic field, $\mathbf{H_M}$ is the Hamiltonian associated with the perturbation introduced by the external magnetic field. We will first describe $\mathbf{H_0}$ and then talk about $\mathbf{H_M}$.

The main contribution to $\mathbf{H_0}$ is coming from the kinetic and potential energy operators associated with the motion of an electron in the potential created by the nucleus of the

atom. In the case of multi-electronic atoms, we have to take into account contributions from the other electrons on the considered one. An orbiting electron will have an orbital angular momentum $\mathbf{L}$, such that the eigenvalues of the operator $\mathbf{L}^2$ will be $\hbar l(l+1)$, and l being the orbital quantum number, with $l = 0, 1, 2, ...$ depending on the considered orbital. The electron will have a spin momentum $\mathbf{S}$, with $\mathbf{S}^2$ having the eigenvalues $(\hbar s(s+1))$, and the spin quantum number taking the values $s = 0, 1/2, 1, ...$ depending on the electronic configuration.

The momenta $\mathbf{L}$ and $\mathbf{S}$ will have magnetic moments $\boldsymbol{\mu}_l$ and $\boldsymbol{\mu}_s$ respectively. This will make the two momenta interact with each other.

$$\boldsymbol{\mu}_l = -g_l \frac{\mu_B}{\hbar} \mathbf{L}, \tag{2.2}$$

with $\mu_B = e\,\hbar/(2\,m)$ being the Bohr magneton. e is the electron's charge, m the electron's mass and $\hbar$ the reduced Planck constant. $g_l = 1$ is the Landé factor corresponding to the orbital momentum. It is a proportionality factor between the magnetic and orbital momenta, which might be retrieved in a more fundamental formulation of the magnetic momentum in terms of the field resulting of an electron in an orbital motion.

For the spin we can write a similar formula:

$$\boldsymbol{\mu}_s = -g_s \frac{\mu_B}{\hbar} \mathbf{S}, \tag{2.3}$$

where $g_s = 2$ is the Landé factor for the Spin of the electron

We only consider interaction between orbital and spin magnetic moments, and neglect the nuclear magnetic moment which is shown to be at least 3 orders of magnitude smaller than the electronic moments (Sobel'man 1972). We consider only a spin-orbit (L-S) interaction. The Hamiltonian $\mathbf{H_0}$ will then include a small contribution due to the L-S coupling. We define the total angular momentum $\mathbf{J} = \mathbf{L} + \mathbf{S}$, with $\mathbf{J}^2$ having the eigenvalues $\hbar j(j+1)$, and j varying between $|l+s|$ and $|l-s|$

The external magnetic field will also interact with the magnetic moment of the bound electron. If the L-S coupling dominates over the interaction of the external magnetic field with the magnetic moment of the bound electron, $\mathbf{H_M}$ can be treated as a perturbation to $\mathbf{H_0}$. This is the so called Zeeman regime. This is a common situation with relatively weak magnetic field (like in the solar photosphere). But if the interaction of the external $\mathbf{B}$ dominates over the L-S coupling, the magnetic orbital moment and the spin moment interact separately with $\mathbf{B}$. This is the so called Paschen-Back effect. We will describe here the Zeeman effect only.

The total magnetic moment of the electron will couple to the external magnetic field, such that the Hamiltonian $\mathbf{H_M}$ has eigenvalues E_M, such that:

$$E_M = -\boldsymbol{\mu}_j . \mathbf{B} \tag{2.4}$$

with $\boldsymbol{\mu}_j$ being the magnetic moment associated with the total angular momentum $\mathbf{J}$.

$$\boldsymbol{\mu}_j = -g \frac{\mu_B}{\hbar} \mathbf{J} \tag{2.5}$$

where "g" is the Landé factor associated with the total magnetic moment.

In term of **L** and **S**, we get:

$$E_M = \frac{\mu_B}{\hbar}(g_l\mathbf{L} + g_s\mathbf{S}).\mathbf{B} \tag{2.6}$$

L and **S** are not separately conserved, only the total angular momentum **J** is conserved. The spin and orbital angular momentum vectors can be thought of as precessing about the total angular momentum vector **J**. We can write:

$$E_M = \frac{\mu_B}{\hbar}(g_l < \mathbf{L} > + g_s < \mathbf{S} >)\mathbf{B} \tag{2.7}$$

Where $< \mathbf{L} >$ and $< \mathbf{S} >$ are the time-averaged spin and angular momenta. They are the projection of the spin and angular momenta on the direction of **J** :

$$< \mathbf{S} >= \frac{\mathbf{SJ}}{\mathbf{J^2}}\mathbf{J}, \tag{2.8}$$

and

$$< \mathbf{L} >= \frac{\mathbf{LJ}}{\mathbf{J^2}}\mathbf{J}. \tag{2.9}$$

Thus the eigenvalue associated with a Zeeman perturbation can be written:

$$E_M = \frac{\mu_B}{\hbar}\mathbf{J}(g_l\frac{\mathbf{LJ}}{\mathbf{J^2}} + g_s\frac{\mathbf{SJ}}{\mathbf{J^2}})\mathbf{B}. \tag{2.10}$$

Using the square of the relation $\mathbf{L} = \mathbf{J} - \mathbf{S}$, we get:

$$\mathbf{SJ} = \frac{1}{2}(\mathbf{J^2} - \mathbf{L^2} + \mathbf{S^2}) = \frac{\hbar^2}{2}[j(j+1) - l(l-1) + s(s+1)] \tag{2.11}$$

Using the square of the relation $\mathbf{S} = \mathbf{J} - \mathbf{L}$, we also get:

$$\mathbf{LJ} = \frac{1}{2}(\mathbf{J^2} + \mathbf{L^2} - \mathbf{S^2}) = \frac{\hbar^2}{2}[j(j+1) + l(l-1) - s(s+1)] \tag{2.12}$$

The presence of the external magnetic field introduces a preferential direction (let us call it the z direction in a Cartesian coordinate system (x,y,z)). $\mathbf{J_z}$ is the projection of **J** on the direction parallel to **B** such that $\mathbf{J_z} = \hbar M$, with $j \geq M \geq -j$. Substituting the relations 2.11 and 2.12 in equation 2.10 we obtain:

$$E_M = \mu_B MB[g_l\frac{j(j+1) - l(l-1) + s(s+1)}{j(j+1)} + g_s\frac{j(j+1) + l(l-1) - s(s+1)}{j(j+1)}] \tag{2.13}$$

and, considering the Landé factors $g_l = 1$, and $g_s = 2$, we finally get:

$$E_M = \mu_B MBg = \mu_B MB[\frac{3}{2}\frac{s(s+1) - l(l-1)}{j(j+1)}] \tag{2.14}$$

thus, the Landé factor associated with the total angular momentum **J** is:

$$g = \frac{3}{2}\frac{s(s+1) - l(l-1)}{j(j+1)} \tag{2.15}$$

15

E_M is then the energy shift associated with an external magnetic filed in the Zeeman regime. In this case, an original state (without external magnetic field) characterized by a set of quantum numbers (l, s, and j) will split (in the presence of an external magnetic field) into (2j+1) sub-states corresponding to all possible values of M. Thus the external magnetic field has removed the degeneracy of the initial state (without magnetic field).

A quantum transition starting from a lower state (with $j = j_l$) to an upper state ($j = j_u$), will start from one of the sub-states (with $j = j_l$ and also $M = M_l$, ($j_l > M > -j_l$)) to one of the upper sub-states (with $j = j_u$ and also $M = M_u$ ($j_u > M > -j_u$)). Not all the transitions between two given states are allowed. The electric dipole radiation selection rules allow only certain transitions to happen. These selection rules are : $\Delta j = j_u - j_l = 0, \pm 1$ and $\Delta M = M_u - M_l = 0, \pm 1$. An exception to these rules is the case when $j_u = j_l = 0$, which is forbidden.

The central frequency ν_0 of the wave associated with each transition is then:

$$\nu_0 = \frac{E_M}{h} = \frac{\mu_B}{h} B (M_l g_l - M_u g_u) \tag{2.16}$$

The transitions with $\Delta M = 0$ are called "π-components". Those with $\Delta M = \pm 1$ are called "$\sigma_{\pm}$-components" respectively. In some textbooks σ_+ and σ_--components are also referred to as σ_b and σ_r-components respectively.

If we define $j_{min} \equiv min(j_l, j_u)$, then the selection rules will give us the total number of possible transitions for each ΔM case. We have :

$$N_\pi = (2 j_{min} + 1) \quad \text{possible } \pi - \text{components} (\Delta M = 0) \tag{2.17}$$
$$N_{\sigma_{+1}} = (j_u + j_l) \quad \text{possible } \sigma_+ - \text{components} (\Delta M = 1) \tag{2.18}$$
$$N_{\sigma_{-1}} = N_{\sigma_{+1}} = (j_u + j_l) \quad \text{possible } \sigma_- - \text{components} (\Delta M = -1) \tag{2.19}$$

The strength $S_{\alpha,i}$ of the different Zeeman components (not to be confused with the spin) is given by:

$$S_{\alpha,i} = \frac{\tilde{S}_{\alpha,i}}{\sum_i \tilde{S}_{\alpha,i}}, \alpha = \Delta M = +1, 0, -1, \tag{2.20}$$

The non-normalized strengths $\tilde{S}_{\alpha,i}$ are given in table 2.1. $i = 0, 1, 2, ...N_\pi$ for π-components, $i = 0, 1, 2, ...N_{\sigma_{+1}}$ for σ_{+1}-components and $i = 0, 1, 2, ...N_{\sigma_{-1}}$ for σ_{-1}-components.

These strengths are defined for the case where the magnetic field vector is perpendicular to the line-of-sight (i.e. the inclination angle $\gamma = \pi/2$). In the general case, the strengths ($S_{\alpha,i,\gamma}$) of Zeeman components at an arbitrary angle γ are calculated from the strengths ($S_{\alpha,i}$) at $\pi/2$ via the Seares formulae (Seares 1913):

$$S_{0,i,\gamma} = S_{0,i} \sin^2(\gamma) \tag{2.21}$$

$$S_{+1,i,\gamma} = S_{+1,i} (1 \pm \cos(\gamma))^2 \tag{2.22}$$

$$S_{-1,i,\gamma} = S_{-1,i} (1 \mp \cos(\gamma))^2 \tag{2.23}$$

	$\Delta M = +1\ (\sigma_b)$	$\Delta M = 0\ (\pi)$	$\Delta M = -1\ (\sigma_b)$
$\Delta J = +1$	$(J_u + M_u)(J_l + M_u)$	$2(J_u^2 - M_u^2)$	$(J_u - M_u)(J_l - M_u)$
$\Delta J = 0$	$(J_u + M_u)(J_u - M_u + 1)$	$2M_u^2$	$(J_u - M_u)(J_u + M_u + 1)$
$\Delta J = -1$	$(J_l - M_u)(J_u - M_u + 2)$	$2(J_l^2 - M_u^2)$	$(J_l + M_u)(J_u + M_u + 2)$

Figure 2.1: Non-normalized strengths $\tilde{S}_{\alpha,i}$ for the possible values of $\alpha = \Delta$ M and ΔJ. Adapted from Borrero (2004).

where the upper and lower signs in the right-hand-sides of equations 2.22 and 2.23 are relevant for right- and left-handed circular analysers respectively.

2.3 Absorption and dispersion in a conducting plasma

Throughout this section we have been mainly using the following sources : Mihalas (1970), Solanki (1987), Rutten (2003), del Toro Iniesta (2003), Borrero (2004), Gray (2005).

   We consider a quasi-monochromatic electromagnetic wave propagation parallel to the Z axis in a Cartesian coordinate system (X, Y, Z) (del Toro Iniesta 2003). The electric field associated with this wave is defined in the plane (X, Y) perpendicular to the direction of propagation of the wave. The projections of the electric vector on the X and Y axes are:

$$E_x(t) = a_x(t) \exp[-i(2\pi\nu_0(t) - \delta_x(t))] \tag{2.24}$$

$$E_y(t) = a_y(t) \exp[-i(2\pi\nu_0(t) - \delta_y(t))] \tag{2.25}$$

a_x and a_y are the amplitudes of each component of the electric field. $\delta_x(t)$ and $\delta_y(t)$ are phase factors to account for time lags between the components of the electric field vector. $\delta(t) = \delta_x(t) - \delta_y(t)$ is defined as the phase difference between the x and y components of the electric field. $\nu_0(t)$ is the central frequency of the quasi-monochromatic light beam. The Stokes parameters associated to this light beam are defined as averages over an entire period :

$$I = \langle a_x^2 \rangle + \langle a_y^2 \rangle \tag{2.26}$$
$$Q = \langle a_x^2 \rangle - \langle a_y^2 \rangle \tag{2.27}$$
$$U = 2\langle a_x a_y \cos(\delta(t)) \rangle \tag{2.28}$$
$$V = 2\langle a_x a_y \sin(\delta(t)) \rangle \tag{2.29}$$

Let us consider an initial Stokes vector $\mathbf{I}$

$$\mathbf{I} = \begin{pmatrix} I \\ Q \\ U \\ V \end{pmatrix} \tag{2.30}$$

The infinitesimal change on that vector experienced when passing through an infinitesimal path ds is given by the transport equation:

$$\frac{d\mathbf{I}}{ds} = -\mathbf{KI} + \mathbf{j} \tag{2.31}$$

$\mathbf{K}$ is the 4×4 absorption matrix, and $\mathbf{j}$ is the emissivity vector. This radiative transfer equation (RTE) for polarized light has been first derived by Unno (1956), and completed by Rachkovsky (1962) to include magneto-optical effects. It tells us that the first term on the right hand side represents infinitesimal subtraction from the Stokes beam and the second term represents infinitesimal additions to the Stokes beam.

The absorption matrix is formed by two terms:

$$\mathbf{K} = \chi_{cont}\mathbb{1} + \chi_{line} = \chi_{cont}\mathbb{1} + \chi_0\boldsymbol{\phi}, \tag{2.32}$$

where χ_{cont} is the continuum absorption coefficient. $\mathbb{1}$ represents the 4×4 unity matrix. χ_0 is the line center absorption coefficient, and $\boldsymbol{\phi}$ is the 4x4 dimensionless frequency-dependent absorption matrix.

χ_{cont} is included isotropically to the absorption matrix since the continuum light is unpolarized. χ_{cont} reflects the properties of the medium in absorbing photons in a large wavelength range. This is by opposition to spectral line formation which comes from the absorption (or emission) of photons associated with the transition of an electron between two bound states. Thus a bound-bound transition produces an absorption in a narrow range of frequency leading to a spectral line. Whereas the continuum absorption coefficient will have much larger variation scales (not at absorption edges or ionization edges), which makes it often approximately constant over a given spectral line. There are two main physical processes that add up to produce χ_{cont}. The first is ionization, where bound-free transition happens, the second is free-free transitions. In these two processes, photons might be absorbed with an infinity of frequencies since the free state can have any energy. One might mention a third process of lower contribution to χ_{cont}, that is bound-bound transition which gives "spectral bands". Normally, bound-bound transitions are not included in χ_{cont}, but in the case where many spectral lines are overlapping in a very dense way (like in the case of neutral hydrogen series near absorption or ionization edges), their contribution becomes much like the two other continuous absorption processes.

Let us have a look to the term $\chi_0\boldsymbol{\phi}$ in equation 2.32. It is formed by the line center absorption coefficient χ_0 multiplied by a 4×4 matrix $\boldsymbol{\phi}$ which is a function of the frequency ν.

Let us start with a simpler case where we have no polarization. We assume also Local Thermodynamical Equilibrium (LTE). Thus equation 2.31 reduces to the transfer of I which is then a scalar quantity. In this case the absorption matrix becomes a scalar absorption profile. In order to keep a clear notation we represent the 4×4 absorption matrix by the "bold character" $\boldsymbol{\phi}$, and the scalar absorption profile by the "normal character" ϕ. We might not always write it, but ϕ is naturally a function of the frequency (ν), since it modulates the line shape over the spectrum. We can also write it as function of ($\nu - \nu_0$) the frequency distance from the center of the line at ν_0. From a quantum mechanical approach, for an absorption line, we have:

$$\chi_{line} = \chi_0 \phi(\nu - \nu_0) = \frac{h\nu_0}{4\pi}[n_l B_{lu} - n_u B_{ul}]\phi(\nu - \nu_0) \tag{2.33}$$

where n_l and n_u are the populations of the lower and upper states of the transition. These populations are determined through the Saha-Boltzmann statistics (Mihalas 1970, Rutten 2003). B_{lu} and B_{ul} are the Einstein coefficients for radiative excitation and induced deexcitation, respectively. h is Plank's constant, and ν_0 is the frequency at the center of the line.

B_{lu} gives the probability per unit time per unit energy density of the radiation field, that an electron in a state "l" with energy E_l will absorb a photon with an energy $E_u - E_l = h\nu$ and jump to a state "u" with energy E_u.

Similarly B_{ul} gives the probability per unit time per unit energy density of the radiation field, that an electron in a state "u" with energy E_u will decay to a state "l" with energy E_l.

Using the relations between Einstein's coefficients and applying Boltzmann statistics (Mihalas 1970, Gray 2005), we find:

$$\chi_0\phi(\nu - \nu_0) = \frac{h\nu_0}{4\pi}n_l B_{lu}[1 - e^{h\nu/kT}]\phi(\nu - \nu_0) \tag{2.34}$$

the factor between brackets is referred to as the "correction factor for stimulated emission". It is shown that for photospheric temperatures, we have: $[1 - e^{h\nu/kT}] \simeq 1$ (Gray 2005, page 149). Thus for photospheric temperatures we may write:

$$\chi_0\phi(\nu - \nu_0) \simeq \frac{h\nu_0}{4\pi}n_l B_{lu}\phi(\nu - \nu_0) \tag{2.35}$$

The lifetime of an electron in an exited state is Δt, thus following Heisenberg, the corresponding energy spread is $\Delta E = h/(2\pi\Delta t)$. Thus, the corresponding frequency spread is: $\Delta\nu = \gamma^{rad}/(2\pi)$ with $\gamma^{rad} \equiv 1/\Delta t$ is called the radiative damping constant. This natural broadening process defines a distribution function around the line center ($\nu = \nu_0$). This "distribution function" $\phi(\nu - \nu_0)$ which we were using in equation 2.35 is:

$$\phi(\nu - \nu_0) = \frac{\gamma_{rad}/(4\pi^2)}{(\nu - \nu_0)^2 + (\gamma_{rad}/4\pi)^2} \tag{2.36}$$

2.3.1   Classical derivation of the absorption and dispersion profiles

The quantum mechanical approach introduced above, has a classical counterpart which is the Lorentz theory considering bound electrons as damped oscillators. Although mainly phenomenological, the classical approach brings several clarifications concerning the interaction of an electromagnetic wave with a plasma. We will proceed now to the calculation of the absorption and dispersion profiles associated with the absorption, dispersion or emission of an electromagnetic wave in a conducting plasma. Considering an electron bound in an atom and perturbed by the electric field of an electromagnetic wave, Newton's second law for this electron can be written:

$$m\ddot{r}(t) = -eE(t) - qr(t) - m\gamma\dot{r}(t), \tag{2.37}$$

The first term on the right-hand-side expresses a force exerted by the external electric field $E(t)$. The second one is the quasi-elastic restoring force, which keeps an electron bound to its equilibrium state. The third term represents a resisting force which damps the oscillator's motion. $r(t)$ is the displacement, e is the electron's charge and m its mass. q is a proportionality factor associated with the restoring electrostatic forces, and γ is a damping constant. Dots over $r(t)$ represent time-derivatives.

Assuming that the $E(t)$ and $r(t)$ are proportional to $e^{-i\omega t}$, we obtain:

$$r(t) = -\frac{e_0}{m}\frac{E(t)}{(q/m) - \omega^2 - i\omega\gamma}, \tag{2.38}$$

where ω is the frequency of the damped oscillator. In the absence of damping ($\gamma = 0$), the oscillator will have a resonant frequency at $\omega_0^2 = (q/m)$, at which the displacement will have infinite values. The presence of damping has caused the oscillator to only have oscillations with finite amplitude. We can write :

$$r(t) = -\frac{e}{m}\frac{E(t)}{\omega_0^2 - \omega^2 - i\omega\gamma}, \tag{2.39}$$

Since in a spectral line we are dealing with frequencies close to the resonant frequency, we can write $(\omega_0^2 - \omega^2)/\omega^2 \ll 1$. Thus $(\omega_0^2 - \omega^2) \simeq 2\omega(\omega_0 - \omega)$.

Then equation 2.39 can be written :

$$r(t) = -\frac{e}{2 m \omega}\frac{E(t)}{\omega_0 - \omega - i\omega\gamma}, \tag{2.40}$$

replacing $\omega = \nu/2\pi$, $\gamma_{rad}/4\pi = \Gamma$ and multiplying by the denominator we get:

$$r(t) \simeq -\frac{e}{8\pi^2 m\nu}\frac{E(t)}{(\nu_0 - \nu) - i\Gamma} = -\frac{e_0\,E(t)}{8\pi^2 m\nu}\frac{((\nu_0 - \nu) + i\Gamma)}{(\nu_0 - \nu)^2 + \Gamma^2}, \tag{2.41}$$

An electromagnetic wave propagating in a medium with electric permittivity ε and magnetic permeability μ will have a velocity V such that:

$$V^2 = c^2\left(\frac{\varepsilon_0\mu_0}{\varepsilon\mu}\right), \tag{2.42}$$

ε_0 and μ_0 are the electric permittivity and magnetic permeability, respectively, for vacuum. c is the speed of light in vacuum. Since we are dealing with gases of very low density, we can assume that $\mu = \mu_0$ (Gray 2005).

The electric field passing through the plasma will cause a charge displacement (displacement of the negatively charged electrons from their position around the positively charged nuclei). This will lead to the creation of electric dipoles. The electric field created by N displaced charges per unit volume is $4\pi N e\,r(t)$, where $r(t)$ is the displacement of electrons induced by the external field. We can write:

$$\frac{\varepsilon}{\varepsilon_0} = \frac{E + 4\pi N e\,r(t)}{E} = 1 + \frac{4\pi N e\,r(t)}{E}, \tag{2.43}$$

The velocity of an electromagnetic wave in a given medium is proportional to the index of

refraction n of the medium, such as : $V^2 = c^2/n^2$. Here the index of refraction is a complex function $n^2 = 1 + 2(\delta + i\kappa)$. κ will be responsible for the decrease of the amplitude of the electromagnetic wave when travelling through the plasma. δ induces a phase shift to the electromagnetic wave across its path in the plasma.

After replacing $\varepsilon/\varepsilon_0$ from equation 2.43 in equation 2.42, we can write :

$$\frac{c^2}{V^2} = 1 + 2(\delta + i\kappa) = 1 + \frac{4\pi Ner(t)}{E}, \tag{2.44}$$

Replacing $r(t)$ (equation 2.41) in equation 2.44, we obtain :

$$1 + 2(\delta + i\kappa) = 1 + \frac{Ne^2}{2\pi m\nu} \frac{(\nu_0 - \nu) + i\Gamma}{(\nu_0 - \nu)^2 + \Gamma^2}, \tag{2.45}$$

and by identification:

$$\delta = \frac{Ne^2}{4\pi m\nu} \frac{\nu_0 - \nu}{(\nu_0 - \nu)^2 + \Gamma^2}, \tag{2.46}$$

$$\kappa = \frac{Ne^2}{4\pi m\nu} \frac{\Gamma}{(\nu_0 - \nu)^2 + \Gamma^2}, \tag{2.47}$$

We can then obtain the absorption coefficient $\chi_{line} = (4\pi\nu/c)\,\kappa$. Its inverse $1/\chi_{line}$ represents the mean free path of photons, (i.e. the distance covered by photons between two subsequent encounters with atoms).

$$\chi_{line} = \chi_0 \phi(\nu - \nu_0) = \frac{N\pi e^2}{mc} \frac{\Gamma/\pi}{(\nu_0 - \nu)^2 + \Gamma^2}, \tag{2.48}$$

χ_0 is the line center absorption coefficient. We can see that absorbtion is modulated by a function of ν giving maximum at the resonance frequency and decreasing further away. This function of ν is the so called Lorentzian profile $\phi(\nu - \nu_0)$ which we have already seen with the quantum mechanical approach (equations 2.36).

$$\phi(\nu - \nu_0) = \frac{\Gamma/\pi}{(\nu_0 - \nu)^2 + \Gamma^2}, \tag{2.49}$$

The dispersion coefficient $\tilde{\chi}_{line}$ is also modulated by a function of ν which is $\psi(\nu - \nu_0)$

$$\tilde{\chi}_{line} = \frac{N\pi e^2}{mc} \frac{\nu_0 - \nu}{(\nu_0 - \nu)^2 + \Gamma^2}, \tag{2.50}$$

$$\psi(\nu - \nu_0) = \frac{\nu_0 - \nu}{(\nu_0 - \nu)^2 + \Gamma^2}, \tag{2.51}$$

Measurement of the absorption coefficient (especially its integrated value over the line profile) gives values which are usually smaller than that expressed in equation 2.48 by a given factor called "oscillator strength : f ". This proportionality factor is the same for each given spectral line, but is different from one line to the other. This correction is coming from the quantum mechanical nature of the line formation process. We have then

$$\chi_{line} = \chi_0 \phi(\nu - \nu_0) = \frac{N\pi e^2}{mc} f \frac{\Gamma/\pi}{(\nu_0 - \nu)^2 + \Gamma^2}, \tag{2.52}$$

At this stage we may equate the quantum mechanical (equation 2.35) and the classical (equation 2.52) expressions of the absorption coefficient:

$$\chi_{line} = \frac{h\nu_0}{4\pi}[N\,B_{lu}]\frac{\Gamma/\pi}{(\nu_0 - \nu)^2 + \Gamma^2} = \frac{N\pi e^2}{mc}\,f\,\frac{\Gamma/\pi}{(\nu_0 - \nu)^2 + \Gamma^2} \tag{2.53}$$

This gives the oscillator strength:

$$f = \frac{mch\nu_0}{4\pi^2 e^2}B_{lu}, \tag{2.54}$$

Thus the oscillator strength is proportional to Einstein's coefficient for radiative excitation. That means it will depend on the probability of transition between the lower and upper considered states. To account for corrections due to stimulated emission, we can use equation 2.34 instead of equation 2.35 in the above calculations. This straightforward calculation is not needed under photospheric temperatures (Gray 2005).

2.3.2 The Doppler broadening of spectral lines

The thermal agitation in a given plasma will cause atoms and all particles to have a certain distribution of velocities. If local thermodynamical equilibrium is assumed, then the distribution of velocities is Maxwellian. The most probable velocity value is defined as :

$$V_D = \sqrt{\frac{2kT}{m} + \xi_{mic}^2}, \tag{2.55}$$

T is the temperature, k is the Boltzmann constant and m is the mass of the considered particle. The microturbulence ξ_{mic} is an additional parameter which takes into account motions at scales sufficiently smaller than the mean height range of line formation. The Doppler-frequency-shift associated to V_D, will be: $\Delta\nu_D = c\,V_D\,\nu_0$. c is the speed of light and ν_0 is the line center frequency.

If we observe a plasma formed of N atoms having, let's say, a Maxwellian distribution of velocities, the overall absorption or emission profiles will result from the convolution of $\phi(\nu_0 - \nu)$ with a Gaussian profile accounting for the velocity distribution (see Figure 2.2). The resulting profile is:

$$\phi(u, a) = \frac{1}{\sqrt{\pi}}H(u, a), \tag{2.56}$$

with $u = (\nu_0 - \nu)/(\Delta\nu_D)$ expresses the frequency shift with respect to the line center frequency ν_0 in units of the Doppler-frequency-shift $\Delta\nu_D$. The damping constant "a" is defined also in units of Doppler-frequency-shift as: $a = \Gamma/\Delta\nu_D$. The Voigt function $H(u, a)$ is given by :

$$H(u, a) = \frac{a}{\pi}\int_{-\infty}^{+\infty}e^{-y^2}\frac{1}{(u - y)^2 + a^2}dy, \tag{2.57}$$

And similarly for the dispersion profile (right panel of Figure 2.2):

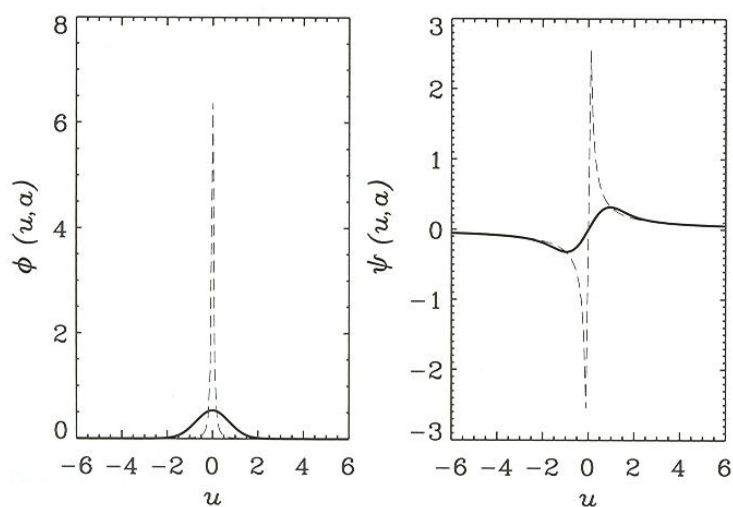$$\psi(u, a) = \frac{1}{\sqrt{\pi}}F(u, a), \tag{2.58}$$

Figure 2.2: In full line, an example of Voigt profile (left panel) and Faraday-Voigt profile (right panel). In dashed line, the original absorption (left panel) and dispersion (right panel) profiles, before taking the Doppler broadening into account. Adapted from del Toro Iniesta (2003).

with $F(u_0, a)$ called the Faraday-Voigt profile, defined as :

$$F(u, a) = \frac{a}{\pi} \int_{-\infty}^{+\infty} e^{-y^2} \frac{u - y}{(u - y)^2 + a^2} dy, \tag{2.59}$$

2.3.3   Pressure broadening effect

In a collisional plasma, an emitting or absorbing atom might be subject to collisions. These collisions can be with similar or different atoms, with molecules, with electrons, or ions. The atomic levels of the emitting or absorbing atom are disturbed by these collisions. The disturbance of the initial energy states is proportional to the distance "R" between the atom and the perturbing particle. The shift of energy levels caused by these interactions is generally expressed in the form of a power law of "R". The presence of theses energy level perturbations will affect the initial line profile in a way that induces an extra broadening to the initial natural one. This acts like additional terms in the damping constant.

2.4   Radiative transfer equation in Zeeman regime

In the previous section we have seen that a Stokes vector is subject to absorption, dispersion and emission processes when passing through a plasma. This is described by equation 2.31:

$$\frac{d\mathbf{I}}{ds} = -\mathbf{K}\mathbf{I} + \mathbf{j} \tag{2.60}$$

From equation 2.32, we can then write:

$$\mathbf{K} = \chi_{cont}(\mathbb{1} + \frac{\chi_{line}}{\chi_{cont}}\boldsymbol{\phi}) \tag{2.61}$$

We can define now $\eta_0 = \frac{\chi_{line}}{\chi_{cont}}$ the line-to-continuum absorption coefficient ratio. After replacing in equation 2.31, we get:

$$\frac{d\mathbf{I}}{d\tau_c} = [\mathbb{1} + \eta_0\boldsymbol{\phi}](\mathbf{I} - \mathbf{S}) \tag{2.62}$$

where $d\tau_c = -\chi_{cont}ds$, and the continuum optical depth is : $\tau_c = -\int_s^{s_0}\chi_{cont}ds$. It is defined in the direction starting from the observer at (s_0) to the specific point in the plasma at (s). This explains the "-" sign in the integral.

The introduction of the source function ($\mathbf{S} = \mathbf{j}/\chi_{cont}$) brings a big advantage to equation 2.62 since in many astrophysical cases where the plasma is in Local Thermodynamical Equilibrium (LTE) the source function is simply a Planck functions ($\mathbf{S} \approx \mathbf{B(T)}$). The combination ($\mathbf{S}, \chi_{cont}[\mathbb{1} + \eta_0\boldsymbol{\phi}]$) presents a more "orthogonal" parameter space to describe the radiative transfer than ($\mathbf{j}, \chi_{cont}[\mathbb{1} + \eta_0\boldsymbol{\phi}]$). Indeed, the parameter $\chi_{cont}[\mathbb{1} + \eta_0\boldsymbol{\phi}]$ takes into account the atomic particle properties (such as the gas composition, the degree of ionization, the probability of spectral line transition). Whereas the parameter $\mathbf{S}$ describes the thermodynamical state of the medium as an ensemble of particles and photons. $\mathbf{j}$ is influenced by both atomic and thermodynamical properties. It is then intrinsically more complicated, and thus less suitable to use.

Equation 2.62 can be written more explicitly:

$$\frac{d}{d\tau_c}\begin{pmatrix} I \\ Q \\ U \\ V \end{pmatrix} = \begin{pmatrix} \eta_I & \eta_Q & \eta_U & \eta_V \\ \eta_Q & \eta_I & \rho_V & -\rho_U \\ \eta_U & -\rho_V & \eta_I & \rho_Q \\ \eta_V & \rho_U & -\rho_Q & \eta_I \end{pmatrix}\begin{pmatrix} I - B(T) \\ Q \\ U \\ V \end{pmatrix} \tag{2.63}$$

where the elements of the propagation matrix are explicitly:

$$\eta_I = \frac{\eta_0}{2}(\phi_0 \sin^2\gamma + \frac{1}{2}[\phi_{+1} + \phi_{-1}](1 + \cos^2\gamma)), \tag{2.64}$$

$$\eta_Q = \frac{\eta_0}{2}(\phi_0 - \frac{1}{2}[\phi_{+1} + \phi_{-1}])\sin^2\gamma\cos 2\varphi, \tag{2.65}$$

$$\eta_U = \frac{\eta_0}{2}(\phi_0 - \frac{1}{2}[\phi_{+1} + \phi_{-1}])\sin^2\gamma\sin 2\varphi, \tag{2.66}$$

$$\eta_V = \frac{\eta_0}{2}[\phi_{-1} - \phi_{+1}]\cos\gamma, \tag{2.67}$$

$$\rho_Q = \frac{\eta_0}{2}(\psi_0 - \frac{1}{2}[\psi_{+1} + \psi_{-1}])\sin^2\gamma\cos 2\varphi, \tag{2.68}$$

$$\rho_U = \frac{\eta_0}{2}(\psi_0 - \frac{1}{2}[\psi_{+1} + \psi_{-1}])\sin^2\gamma\sin 2\varphi, \tag{2.69}$$

$$\rho_V = \frac{\eta_0}{2}[\psi_{-1} - \psi_{+1}]\cos\gamma. \tag{2.70}$$

The absorption profiles $\phi_{0,\pm1}$ in equations 2.64- 2.67, are defined as we have seen in the previous sections:

$$\phi_0 = \sum_{i=1}^{N_\pi} S_{0,i}\,\phi(u_i, a_i), \tag{2.71}$$

where we have summed over all the π-components from 0 to N_π (see relation equation 2.17). $S_{0,i}$ and $\phi(u_i, a_i)$ are respectively the strength and absorption profile of each π-component (see equations 2.20 and 2.56). $u_i = (\nu_{0,i} - \nu)/(\Delta\nu_D)$, where $\nu_{0,i}$ is the line-center frequency of each Zeeman π-component.

Then also ϕ_{+1} and ϕ_{-1} are:

$$\phi_{+1} = \sum_{i=1}^{N_{\sigma_{+1}}} S_{+1,i}\,\phi(u_i, a_i), \tag{2.72}$$

and

$$\phi_{-1} = \sum_{i=1}^{N_{\sigma_{-1}}} S_{-1,i}\,\phi(u_i, a_i), \tag{2.73}$$

The dependence of the line strength on the direction of propagation (equations 2.21- 2.23) is here taken into account directly in equations 2.64- 2.70.

The dispersion profiles $\psi_{0,\pm1}$ are:

$$\psi_0 = \sum_{i=1}^{N_\pi} S_{0,i}\,\psi(u_i, a_i), \tag{2.74}$$

$$\psi_{+1} = \sum_{i=1}^{N_{\sigma_{+1}}} S_{+1,i}\,\psi(u_i, a_i), \tag{2.75}$$

$$\psi_{-1} = \sum_{i=1}^{N_{\sigma_{-1}}} S_{-1,i}\,\psi(u_i, a_i), \tag{2.76}$$

If we consider a simple case e.g. the transition from $j_l = 0$ to $j_u = 1$, we will have $M_l = 0$ and $M_u = -1, 0, +1$. In this situation $N_\pi = N_{\sigma_{+1}} = N_{\sigma_{-1}} = 1$, we will have three Zeeman components, but each one is produced by only one possible transition. In a more general case N_π, $N_{\sigma_{+1}}$ and $N_{\sigma_{-1}}$ can be larger than one. In this case each polarized component (described by ϕ_0, ϕ_{-1} or ϕ_{+1}) might result from the contribution of several different transitions, all with the same polarization for each ϕ_M, ($M = 0, \pm1$).

The Zeeman radiative transfer equation (RTE) can be solved numerically, knowing the atomic parameters of the considered transition and the optical-depth distribution of physical quantities in an atmosphere. There are two widely used numerical methods (among others) that provides solution of the Zeeman RTE, namely a Hermitian method (Bellot Rubio et al. 1999b), and a Diagonal Element Lambda Operator (DELO: Rees et al. 1989). Both methods are implemented in the fast and widely tested STOPRO code in

the SPINOR package (Solanki 1987, Frutiger et al. 2000). This will be used in the next chapters to synthesize Stokes parameters for a given spectral line.

3 Comparison of the thin flux tube approximation with 3D MHD simulations

3.1 Introduction

Most magnetic flux outside sunspots at photospheric level exists in the form of discrete concentrations having a field strength of 1-2 kG, and is concentrated in inter-granular lanes as a result of flux expulsion (Weiss 1966, Galloway and Weiss 1981, Schüssler 1990). These flux concentrations have generally been described as magnetic flux tubes (Howard and Stenflo 1972, Harvey 1977, Spruit and Roberts 1983), for a review see (Solanki 1993)

There has been a large number of attempts to model these flux tubes. An early approach is the so called "thin flux tube approximation ". In its simplest form, we consider the vertical component of the magnetic field to be constant across the tube's cross-section, and the radial component to be a linear function of the tube's radius (Roberts and Webb 1978, 1979). The thin flux tube approximation holds if the diameter of the flux tube is sufficiently small compared to variations of the relevant physical quantities (such as pressure, density,...etc.) along the tube (Spruit 1981, Schüssler 1992). For a vertical tube, this essentially implies that the tube's radius must be small compared with the pressure and density scale heights.

The concept of the thin flux tube can be generalized by writing all physical quantities (magnetic field, temperature, pressure,...etc) in terms of a Taylor expansion in the radial distance from the axis, and injecting them in the MHD equations (or MHS equations). If we only keep 0th order terms, we obtain the 0th-order approximation introduced above. If we then consider higher-order terms, the equations take into account variations across the tube's cross-section.

Such a generalization of the thin flux tube approximation to include variations of the magnetic field across the tube's cross section has been often used. Pneuman et al. (1986) have included in their modelling the effects of field line curvature, internal structures, twist, and the merging of flux tubes with their neighbours. A derivation of linear wave modes of a flux tube including second order radial expansion has been carried out by Ferriz-Mas et al. (1989).

Despite the attractive simplicity of the thin flux tube approximation, it is more self consistent to model magneto-convection at the solar photosphere using a full set of MHD equations including a proper treatment of radiative and convective energy transport (e.g.

Vögler et al. 2005).

The structure and configuration of flux concentrations in such MHD simulations become seemingly complex, owing to their interaction with convection and energy exchange with the neighbouring plasma. Here, we investigate the properties of these flux tubes (or flux sheets) and compare them to a classical thin flux tube approximation (up to 2rd order).

There is a large body of work in the literature based upon the thin flux tube approximation. This includes theoretical work (structure of flux concentrations, equilibrium, oscillations/wave, stability,...etc.) and interpretation of observations (for some reviews, see Solanki 1993, Solanki et al. 2006). We wish to evaluate to which extent the assumption of thin flux tubes has been/is justified in the light of the new 3D MHD simulations. We will then establish a comparative analysis of these two modelling approaches (ie. 3D radiation-MHD model, and thin flux tube/sheet model).

In what follows, we will first present the necessary equations for the thin flux tube and thin flux sheet model. After that we will introduce the 3D MHD simulations used in this chapter.

In Section 5.4, we will present an analysis of a flux sheet in a snapshot of a 3D MHD simulation and compare it with a thin flux sheet model. A study of the gas and total pressures is presented in Section 5.5. Sections 3.6 and 3.7 are dedicated, respectively, to strong and very weak flux concentrations. Concluding remarks are made in Section 3.8.

3.2   A series expansion of the thin flux tube/sheet equations

We consider a magnetic flux tube to be a bundle of magnetic field lines with a circular cross section, which is separated from its non-magnetic surroundings by a tangential discontinuity with a surface current (Schüssler 1992).

For an axisymmetric vertical flux tube, we adopt cylindrical coordinates (r,θ,z), with the z-axis pointing in the vertical direction. Physical quantities are regular at the axis ($r=0$), so that they can be described in terms of a Taylor expansion in the radial coordinate (Roberts and Webb 1978, Spruit 1981, Spruit and Roberts 1983, Pneuman et al. 1986, Ferriz-Mas et al. 1989, Schüssler 1992):

$$w(r,z) = w(0,z) + r\frac{\partial w}{\partial r}(0,z) + \frac{r^2}{2}\frac{\partial^2 w}{\partial r^2}(0,z) + ... \tag{3.1}$$

$$\equiv w_0(z) + rw_1(z) + r^2 w_2(z) + ..., \tag{3.2}$$

Where w_k is defined as:

$$w_k \equiv \frac{1}{k!}\frac{\partial^k w}{\partial r^k}(r=0). \tag{3.3}$$

The properties of the axisymmetric MHD equations (Ferriz-Mas and Schüssler 1989) imply that only even orders ($w_0, w_2, w_4, ...$) are non-zero in the above expansion for scalar quantities (such as temperature or density) and for z-components of vectors, whereas for the radial and θ-components of vectors only the odd orders remain ($w_1, w_3, w_5, ...$).

We then have

$$B_z = B_{z0} + r^2 B_{z2} + r^4 B_{z4} + ..., \tag{3.4}$$

$$B_r = r B_{r1} + r^3 B_{r3} + ..., \tag{3.5}$$

$$B_\theta = r B_{\theta 1} + r^3 B_{\theta 3} + ..., \tag{3.6}$$

and

$$P = P_0 + r^2 P_2 + r^4 P_4 + ..., \tag{3.7}$$

$$T = T_0 + r^2 T_2 + r^4 T_4 + ..., \tag{3.8}$$

where B_r, B_θ, B_z, represent the three components of the magnetic field vector. P and T are the gas pressure and temperature, respectively.

3.2.1 B_z and B_r under the thin flux tube approximation

We now derive the thin tube equations. For the static case (no velocity, time-independent), we consider the momentum equation in the three coordinate dimensions, and the solenoidality relation. We write these four equations in non-dimensional form (Pneuman et al. 1986):

$$\alpha \frac{\partial p}{\partial x} = b_z \left(\frac{\partial b_r}{\partial y} - \frac{\partial b_z}{\partial x} \right) - \frac{b_\theta}{x} \frac{\partial}{\partial x}(x b_\theta), \tag{3.9}$$

$$0 = \frac{b_r}{x} \frac{\partial}{\partial x}(x b_\theta) + b_z \frac{\partial b_\theta}{\partial y}, \tag{3.10}$$

$$\alpha \left(\frac{\partial p}{\partial y} + \frac{p}{\sigma} \right) = -b_r \left(\frac{\partial b_r}{\partial y} - \frac{\partial b_z}{\partial x} \right) - b_\theta \frac{\partial b_\theta}{\partial y}, \tag{3.11}$$

$$0 = \frac{1}{x} \frac{\partial}{\partial x}(x b_r) + \frac{\partial b_z}{\partial y}, \tag{3.12}$$

with $p = P/P^*$, $\sigma = T/T^*$, $b = B/B^*$, $x = r/H^*$, $y = z/H^*$, $H^* = kT^*/(m_p g)$ and $\alpha = 4\pi P^*/B^{*2}$. The quantities with an asterisk are defined at the tube's axis ($x = r = 0$) and at a reference height ($z = y = 0$). k is Boltzmann's constant, m_p the mean particle mass, g the gravitational acceleration, and H the scale height.

Equations(3.4 to 3.8) are written in non-dimensional form, as follows:

$$b_z = h_0 + h_2 x^2 + h_4 x^4 + ... \tag{3.13}$$

$$b_r = f_1 x + f_3 x^3 + f_5 x^5 + ... \tag{3.14}$$

$$b_\theta = s_1 x + s_3 x^3 + s_5 x^5 + ... \tag{3.15}$$

$$p = p_0 + p_2 x^2 + p_4 x^4 + ... \tag{3.16}$$

$$\sigma = \sigma_0 + \sigma_2 x^2 + \sigma_4 x^4 + ... \tag{3.17}$$

Now we insert these equations in equations (3.9 to 3.12) and collect the terms of equal power in x into equations of corresponding order.

We begin with x^0 terms :

$$h_0(f_1' - 2h_2) - 2s_1^2 = 2\alpha p_2, \tag{3.18}$$

$$2f_1 s_1 + h_0 s_1' = 0, \tag{3.19}$$

$$\sigma_0 p_0' + p_0 = 0, \tag{3.20}$$

$$2f_1 + h_0' = 0, \tag{3.21}$$

where prime denotes derivative with respect to y.

The x^2 terms give:

$$\alpha(\sigma_0 p_2' + \sigma_2 p_0' + p_2) = -\sigma_0 f_1(f_1' - 2h_2), \tag{3.22}$$

$$h_0(f_3' - 4h_4) + h_2(f_1' - 2h_2) - 6s_1 s_3 = 4\alpha p_4, \tag{3.23}$$

$$4f_1 s_3 + 2s_1 f_3 + h_0 s_3' + h_2 s_1' = 0, \tag{3.24}$$

$$4f_3 + h_2' = 0, \tag{3.25}$$

At this stage we can determine h_2, f_1 and f_3 as functions of h_0 and p_2.

We can substitute f_1' in equation (3.18) from equation (3.21). After some algebra, we obtain:

$$h_2 = -\frac{1}{4}h_0'' - s_1^2 - \frac{\alpha p_2}{h_0} \tag{3.26}$$

We assume that the magnetic flux tubes studied here have a negligible twist which allows us to neglect the s_1^2-term, we obtain then :

$$h_2 = -\frac{1}{4}h_0'' - \frac{\alpha p_2}{h_0}, \tag{3.27}$$

f_1 and f_3 are determined from equations (3.21) and (3.25) respectively. we get then :

$$f_1 = -\frac{1}{2}h_0', \tag{3.28}$$

and

$$f_3 = -\frac{1}{4}h_2', \tag{3.29}$$

We can then define B_z until the second order, and B_r until the third order.

The system of equations (3.18 to 3.25) contains 12 variables and only 8 equations. In fact, equation (3.23) expresses a relation between p_4 and h_4. We will neglect this equation here since we are interested in orders lower than the 4th. We have then 7 equations with 10 variables. There have been several approaches in the literature, in order to close this system, e.g. using a relation expressing magnetic flux conservation, total pressure conservation at the boundary of the flux tube at any height, and an energy equation (Ferriz-Mas et al. 1989), or by prescribing two quantities like σ_0 and σ_2 allowing more flexibility in defining the atmosphere (Pneuman et al. 1986). In order to construct a thin flux tube which we will compare with the ones in MHD simulations, we take h_0 and p_2 from these MHD simulations. Then B_z and B_r are determined from equations 3.27 to 3.29. The cross section of the flux tube is determined through the magnetic flux conservation relation:

$$\int_0^{x_0} (h_0 + h_2 x^2) dx = \text{Flux at the base of the tube} = \text{constant}, \qquad (3.30)$$

where x_0 is the tube's radius at a given height. This equation and a relation expressing total pressure continuity at the tube's boundary can be used to close the system (3.18 to 3.22, 3.24, 3.25). The total pressure balance can be expressed as follows:

$$(\beta p_i + b_i^2)|_{x=x_0} = (8\pi P_e + B_e^2)/B^{*2}|_{x=x_0}, \qquad (3.31)$$

where $\beta = 8\pi P^*/B^{*2}$, the suffixes i and e indicate internal and external respectively and capital letters indicate dimensional quantities.

Notice that under the 0th-order approximation we get :

$$(\beta p_0 + h_0^2)|_{x=x_0} = (8\pi P_e + B_e^2)/B^{*2}|_{x=x_0}, \qquad (3.32)$$

This relation does not depend on the radius. Thus the total pressure at a given height under the 0th-order approximation is constant across the tube's cross-section.

Under the 2nd-order approximation we get:

$$(\beta p_0 + h_0^2) + x^2(\beta p_2 + f_1^2 + 2h_0 h_2)|_{x=x_0} = (8\pi P_e + B_e^2)/B^{*2}|_{x=x_0}, \qquad (3.33)$$

In this case the total pressure varies inside the flux tube, but has to match the external total pressure at the tube's boundary layer.

3.2.2 B_z and B_x under the thin flux sheet approximation

A flux sheet is a structure which when looked from above the solar surface will look like an elongated line, with a small width (let's call it "*wi*") comparing to its length ("*len*"). At the bottom of the photosphere we have ($wi << len$). When looked from the side with a point of view parallel to the solar surface and perpendicular to the vector **len**, the sheet will look like a wall. A similar approach as described in the previous section can be used for a flux sheet. In this case the magnetic field component parallel to **len** is constant, and thus plays no direct role in the hydrostatic equilibrium. We can then adopt a Cartesian $2D$ geometry in the $X - z$ plane, where z is the vertical coordinate and X is the horizontal coordinate perpendicular to the vector **len**.

Magneto-hydrostatic equilibrium gives:

$$\alpha \frac{\partial p}{\partial x} = b_z \left(\frac{\partial b_x}{\partial y} - \frac{\partial b_z}{\partial x} \right) \tag{3.34}$$

$$\alpha \left(\frac{\partial p}{\partial y} + \frac{p}{\sigma} \right) = -b_x \left(\frac{\partial b_x}{\partial y} - \frac{\partial b_z}{\partial x} \right) \tag{3.35}$$

$$0 = \frac{\partial b_x}{\partial x} + \frac{\partial b_z}{\partial y} \tag{3.36}$$

Proceeding in a similar way to the flux tube case, we insert the series expansion and write terms of equal order. We note that here $x = X/H^*$.

x^0 order terms give :

$$h_0(f_1' - 2h_2) = 2\alpha p_2 \tag{3.37}$$

$$\sigma_0 p_0' + p_0 = 0 \tag{3.38}$$

$$f_1 + h_0' = 0, \tag{3.39}$$

The x^2 terms are:

$$\alpha(\sigma_0 p_2' + \sigma_2 p_0' + p_2) = -\sigma_0 f_1(f_1' - 2h_2) \tag{3.40}$$

$$h_0(f_3' - 4h_4) + h_2(f_1' - 2h_2) = 4\alpha p_4 \tag{3.41}$$

and

$$3f_3 + h_2' = 0, \tag{3.42}$$

In a similar way as before, we can determine h_2, f_1 and f_3 as functions of h_0 and p_2.

$$h_2 = -\frac{1}{2}h_0'' - \frac{\alpha p_2}{h_0} \tag{3.43}$$

f_1 and f_3 are determined from equation (3.39) and (3.42) respectively :

$$f_1 = -h_0' \tag{3.44}$$

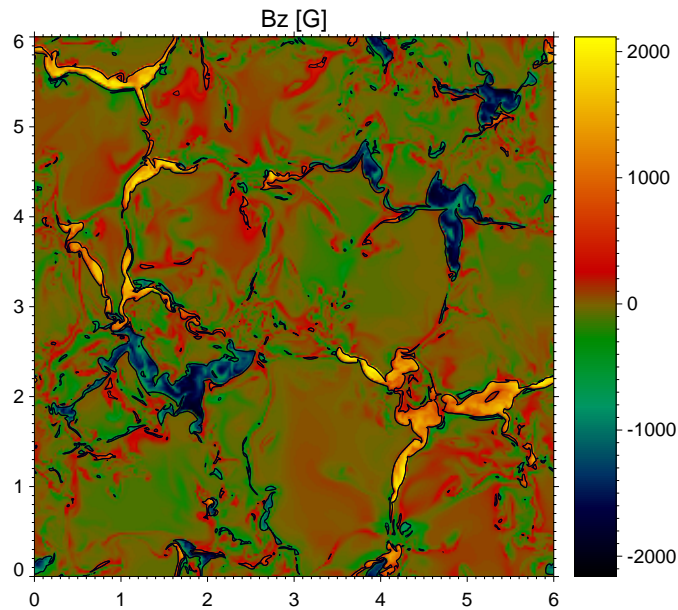and

$$f_3 = -\frac{1}{3}h_2' \tag{3.45}$$

Figure 3.1: Vertical component of the magnetic field at a fixed geometrical height near the averaged visible solar surface ($\tau_{5000} = 1$). The black contours outline regions where $B_z > 500$ G.

3.3   The radiative MHD simulations

There have been several attempts to model the photosphere in a 3D MHD context (Nordlund 1983, Nordlund and Stein 1990, Stein and Nordlund 1998, Bercik 2002, Stein and Nordlund 2003, Vögler and Schüssler 2003, Vögler et al. 2005), for a review see Schüssler (2001). The simulations have demonstrated that the photospheric granulation is a phenomenon where both radiation and convection are necessary ingredients.

The simulation run used here has been obtained with the MURaM code (Vögler 2003, Vögler and Schüssler 2003, Vögler et al. 2005). It takes into account non-local and non-gray radiative energy transport, and includes effects of partial ionization. The simulation box is 6×6 Mm^2 in horizontal extension and 1.4 Mm deep. The cell size is 5 km in the horizontal direction and 7 km in the vertical. The simulation run starts from a plane-parallel atmosphere which extends from -0.8 Mm below to 0.6 Mm above a reference 0, which is roughly situated -100 km below the average continuum optical depth unity ($\tau_{5000} = 1$, which corresponds to the solar surface in the visible). After convection has fully developed, a magnetic field configuration is introduced. This is done such that the simulation domain is divided into four parts with alternate polarities. After some time we choose a representative snapshot (see Figures 3.1- 3.3 taken at a fixed geometrical height roughly representing the solar surface). The mean unsigned field strength at this height is 200 G.
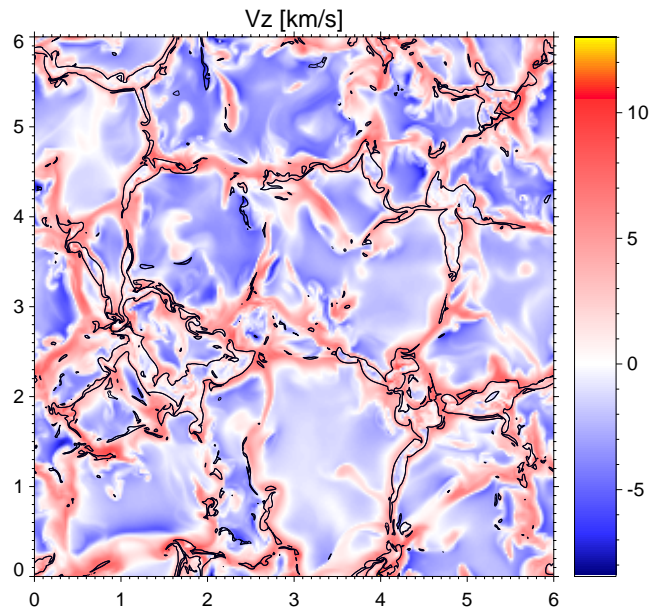
Figure 3.2: Vertical component of the velocity at a fixed geometrical height near the average visible solar surface ($\tau_{5000} = 1$). Downflows are represented in red and upflows in blue.
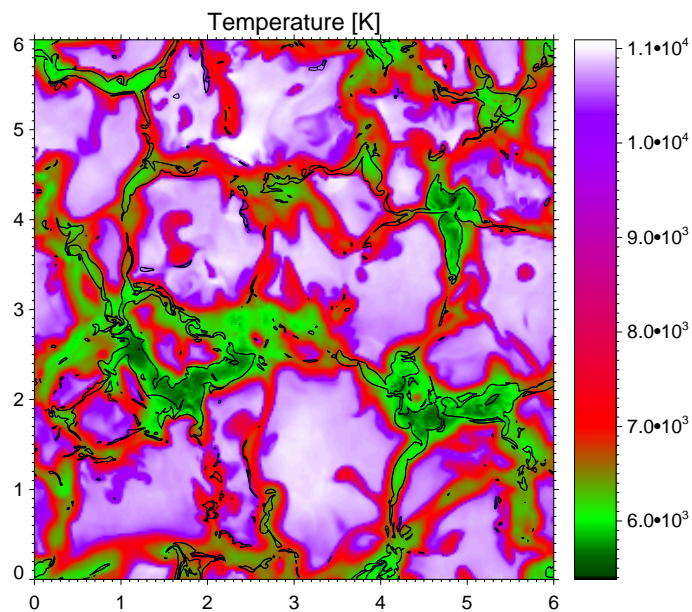

Figure 3.3: Temperature at the same height as the two previous figures.

3.4   Analysis of a thin flux sheet

The approach we want to consider here is aiming to compare the properties of a relatively thin flux sheet in the MHD data (Figure 3.4) with the properties of a second-order thin

flux sheet model presented above (which includes the second order approximation in B_z and third order in B_x). It is important to keep in mind that the flux tubes existing in such a magneto-convection simulation are clearly not in a static state (unlike the assumption made in Section 5.2). They interact with the rest of the plasma, and get distorted dynamically by the granulation motion. They also exchange energy (mainly by radiation) with the surrounding plasma. In order to maintain the numerical stability of the simulation, the gradient of any physical quantity cannot be too important between two neighbouring grid cells. More specifically, the magnetic flux density cannot jump too abruptly from the boundary of a flux tube to the neighbouring non-magnetized plasma (Vögler 2003, PhD thesis). Thus the boundary layer separating a flux tube from the surrounding non-magnetized plasma is a few grid points wide, unlike the tangential discontinuity in the case of an ideal flux tube. We wish to see whether simulations and thin flux sheet/tube approximation are consistent with each other in spite of the fact that MHD flux tubes have finite boundary layers, internal and external dynamics and deviate from an axi- or translationally symmetric configuration. One can qualify where one can hope this comparison to work: 1) Boundary layer thickness $\ll$ sheet's thickness (or tube's diameter). 2) velocities $\ll$ sound speed or Alfvén speed. 3) Internal structuring not inconsistent with low-order truncation of the thin flux tube/sheet equations.

We then select a candidate thin flux sheet in the simulation domain (Figure 3.4). A vertical 2D cut through the flux sheet (Figure 3.5) at the location indicated by the dark line on Figure 3.4 indicates the morphology of the magnetic field. The expansion of the flux sheet with height is mainly determined by magnetic flux conservation with height and a horizontal balance between the magnetic plus gas pressure inside the sheet with the gas pressure outside the sheet. Since the external pressure decreases exponentially with height, it follows that the flux sheet must expand with height (e.g. see Figure 3.5), (Defouw, 1976; Roberts and Webb, 1978).

Figure 3.6 shows profiles of gas pressure (in black), and total pressure (green triangles) along the 5 horizontal lines in Figure 3.5. The location of the sheet is recognizable, by the lower gas pressure. The profiles indicate that the flux sheet's equilibrium in the lower panels is consistent with balance of total pressure in the zeroth-order approximation (see equation 3.32). On the highest panel we see that the total pressure increases somewhat towards the center of the sheet, which is consistent with a second-order approximation (see equation 3.33). In Figure 3.7 we plot the relative difference between the average gas pressure through the whole simulation box and the total pressure, according to the formula:

$$\text{Relative difference in pressure} = \frac{\langle P \rangle - (P + \frac{B^2}{8\pi})}{\langle P \rangle} \qquad (3.46)$$

where $\langle P \rangle$ represents the average gas pressure over the simulation domain and $P + B^2/(8\pi)$ is the total pressure. Orange triangles indicate the location of the flux sheet (where $|B|$ is higher than 75 percent of its maximum value). We notice for the two lower panels that deviations from zero are not specifically correlated with the flux sheet but are rather due to the neighbouring dynamics. For the upper panel we notice a larger relative difference, in the sense that the total pressure is higher than the average pressure, and increases towards the center of the sheet. At this height, the gas pressure, and more precisely the plasma
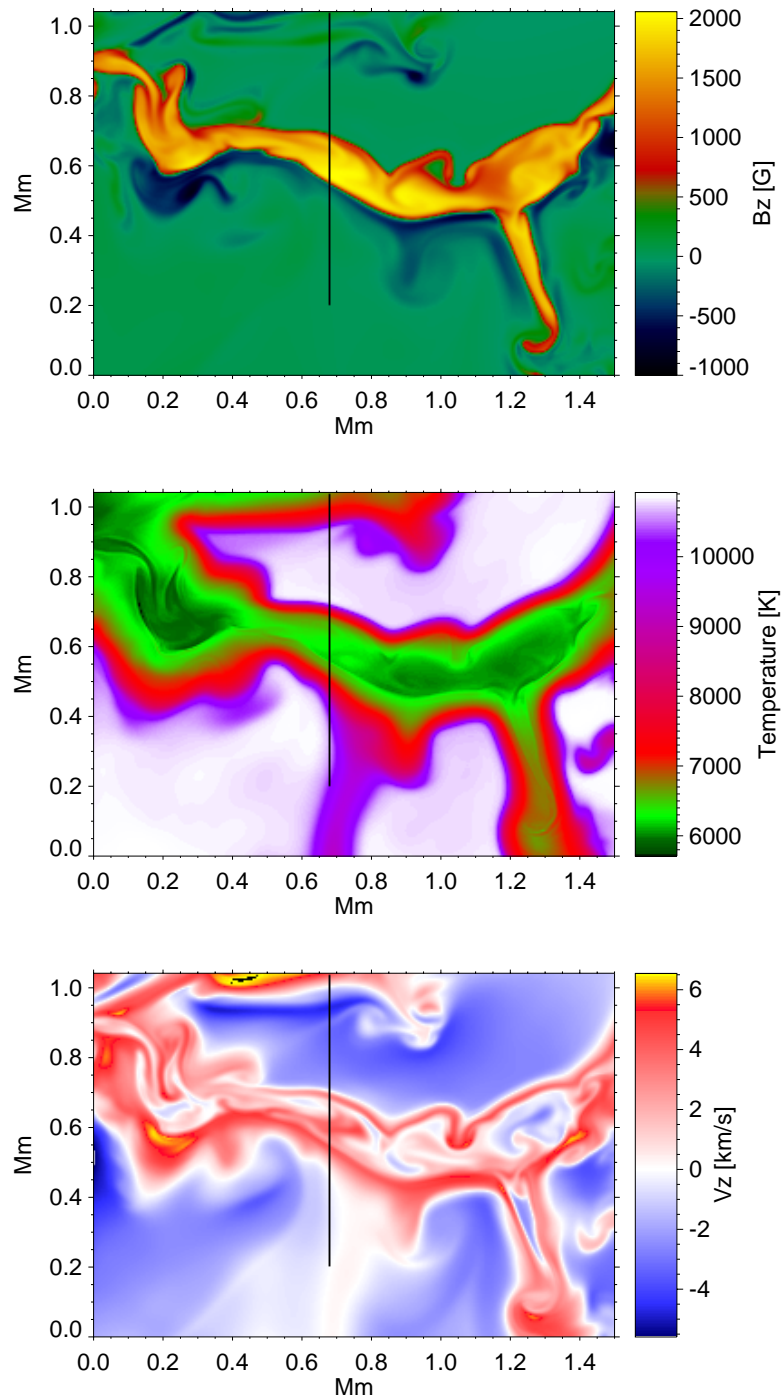
Figure 3.4: From top to bottom : vertical component of the magnetic field, temperature and vertical velocity at the upper left corner of Figure 3.1 at an altitude of 0 km (See Figure 3.5 for height reference). The black lines indicate the location where we will perform a vertical 2D cut in the MHD data.
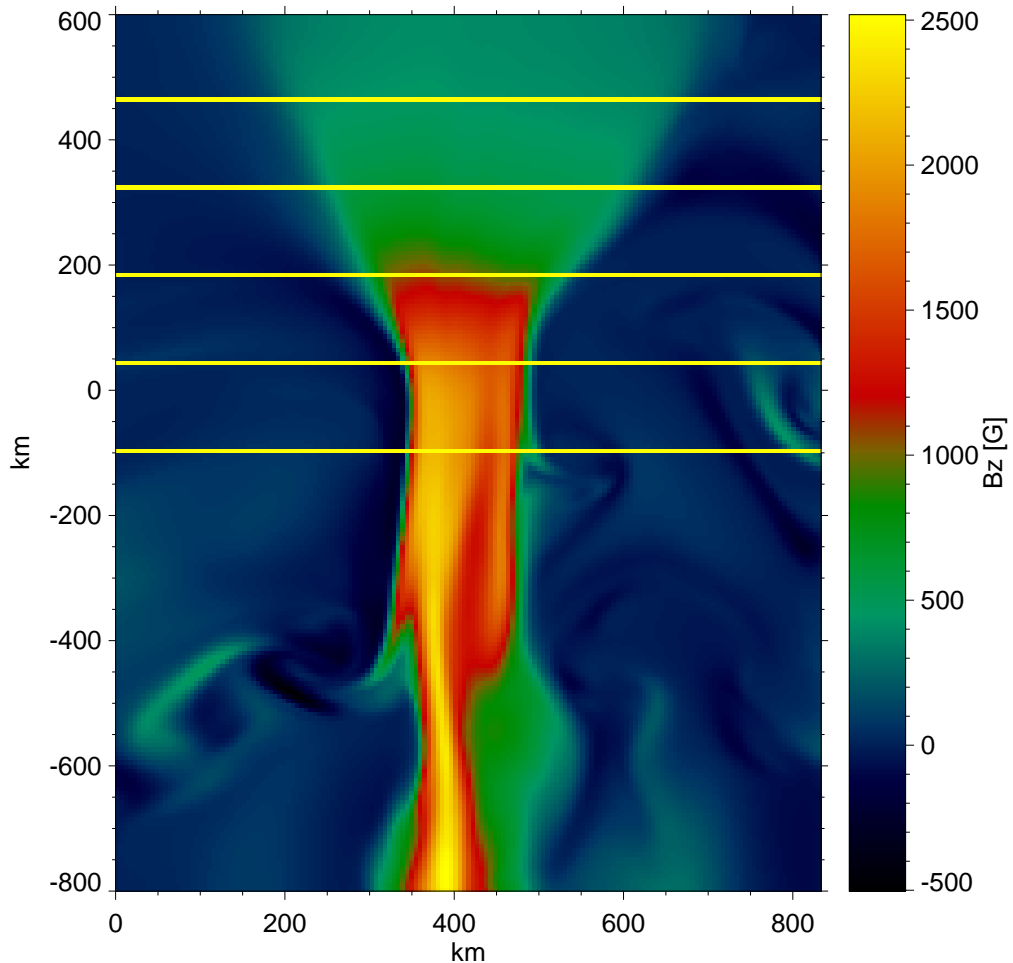
Figure 3.5: Vertical 2D cut in the MHD data at the location shown by the black line in Figure 3.4. The horizontal lines indicate the locations at which we will plot some physical quantities.

$\beta = 8\pi P/B^2$ (see table 3.1) has become so small that the equilibrium tends to become force free, i.e. curvature forces and magnetic pressure gradient balance each other. So the inward tension force will be balanced by outward magnetic pressure force. Thus the magnetic pressure ($\simeq$ total pressure) has to increase inward. Hence the increase of P_{tot} at the center of the sheet in the upper panels of Figure 3.7. This behaviour can be also seen over the whole simulation domain by plotting the horizontally-averaged gas and total pressures as function of height (Figure 3.8). We see the mean gas pressure averaged over regions with field strength smaller than 50 G (black line). The red line shows the mean gas pressure averaged over regions with field strength higher than 500 G, and the green line is for the total pressure over regions with field strength higher than 500 G. We can see that in the lower atmosphere, curvature forces play no role, they only come to play
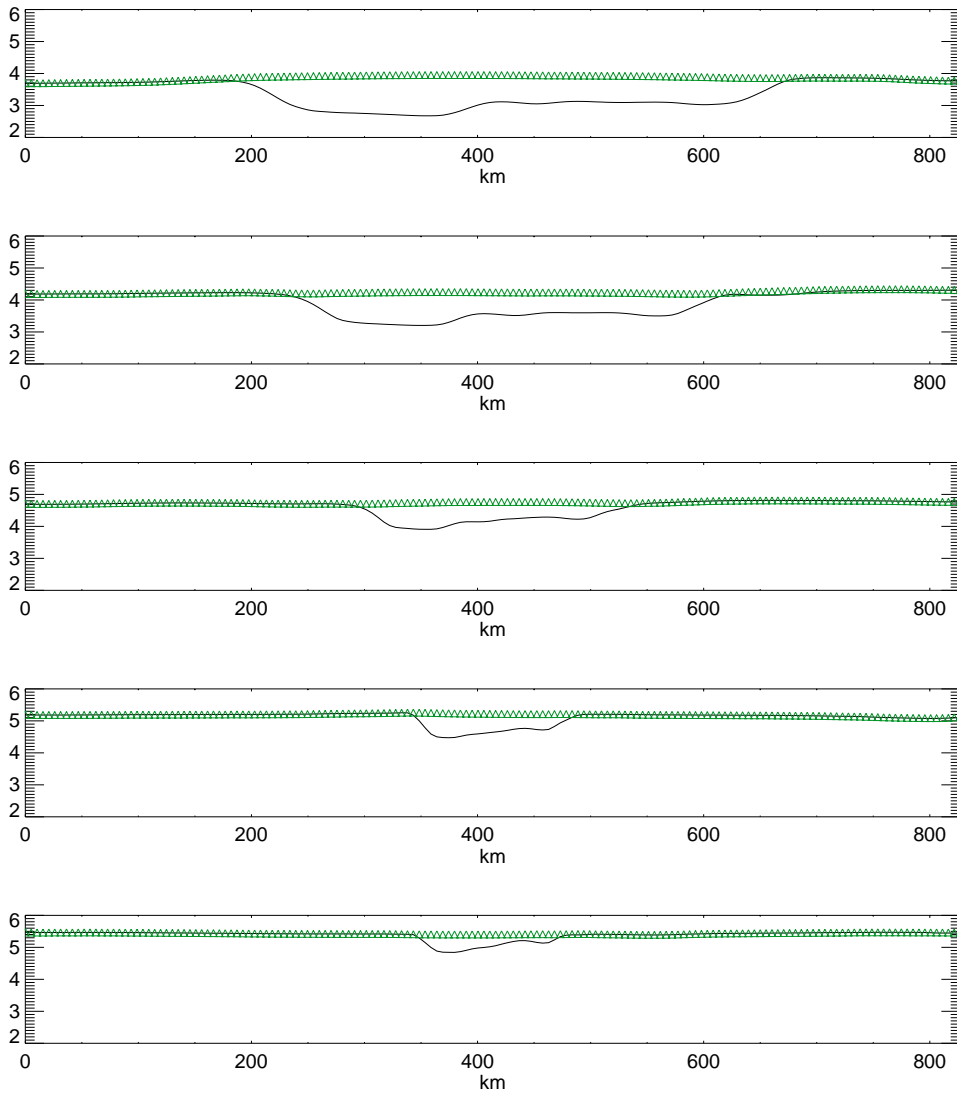
Figure 3.6: Gas pressure (in black) and total pressure (in green), plotted in Logarithmic scale along the 5 horizontal lines in Figure 3.5.

above 250 km. A natural question may be addressed now : Does the divergence between the total pressure (in green) and gas pressure in non-magnetic regions (in black) imply something about the validity of the thin flux sheet/tube model? At this stage we notice that a diagnostic using total pressure does not give a definitive answer on the applicability of a thin flux tube/sheet model to reproduce the MHD sheet. We can only say that the invariance of P_{tot} across a flux tube/sheet is a necessary (but not sufficient) condition for the validity of the 0th-order thin flux tube/sheet approximation. We need then to make a direct comparison of B_z and B_x from the MHD case and from a thin sheet model.

Figure 3.9 indicates the vertical component of the magnetic field, plotted along the 5 horizontal lines in Figure 3.5. The orange triangles represent B_z in the case of a thin flux sheet in the second-order approximation. The dark curves represent B_z from the MHD simulations.
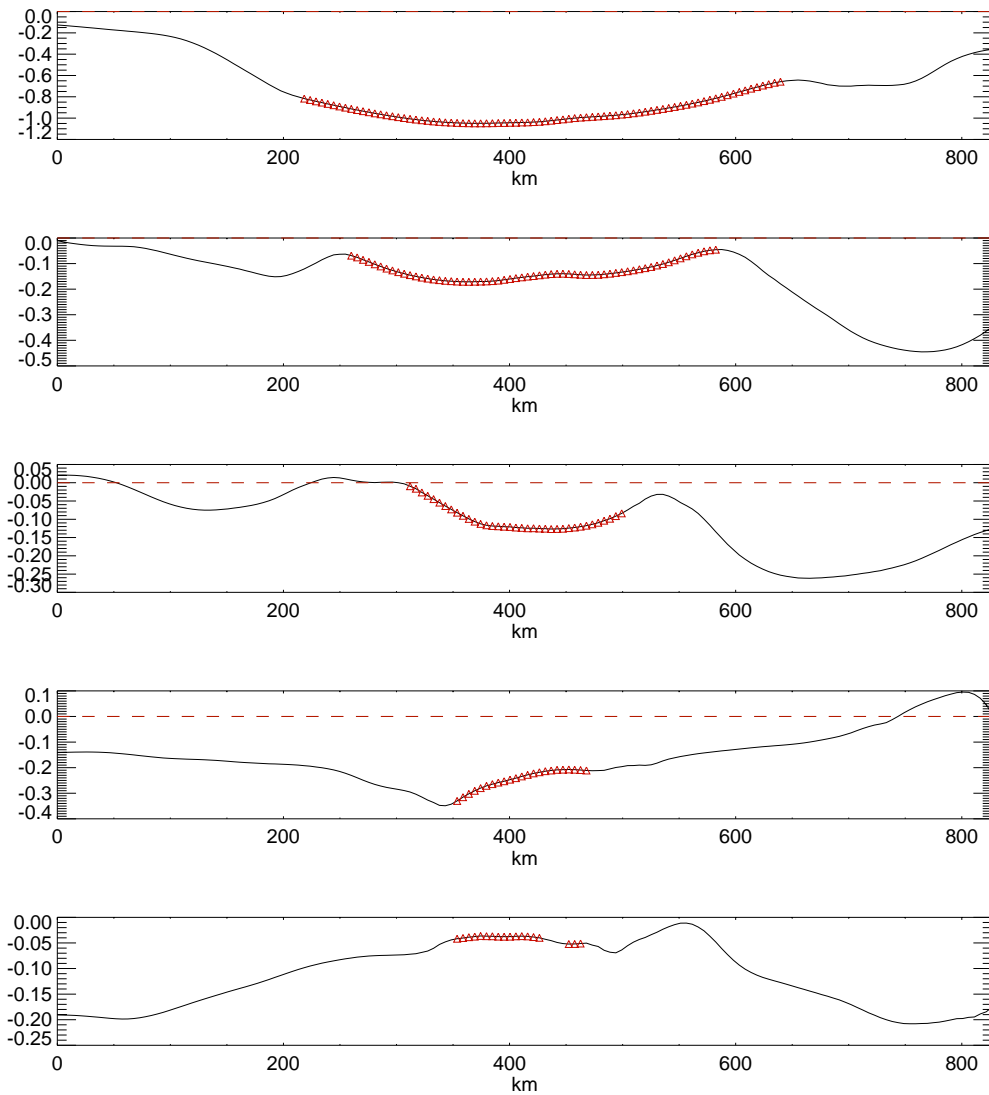
Figure 3.7: Profiles of the relative pressure difference at the 5 heights in the previous figure. It is calculated according to the formula $(\langle P \rangle - (P + B^2/(8\pi)))/\langle P \rangle$, where $\langle P \rangle$ is the average gas pressure over the simulation box at the considered height. The orange triangles indicate the location of the flux sheet.

Table 3.1: Values of β at the 5 heights in Figure 3.5

Line number from bottom to top	1	2	3	4	5
Geometrical height from reference [km]	-98	42	182	322	462
Plasma β	0.85	0.38	0.37	0.26	0.15

We notice that B_z for the thin flux sheet at the two lower panels is close to a constant (small contribution from the 2nd-order terms), whereas at the three upper panels the second-order terms play a clearer role.

We see that low-order approximations (0th and 2nd) reproduce reasonably well the overall B_z profiles obtained from the MHD simulations, especially in the higher layers of
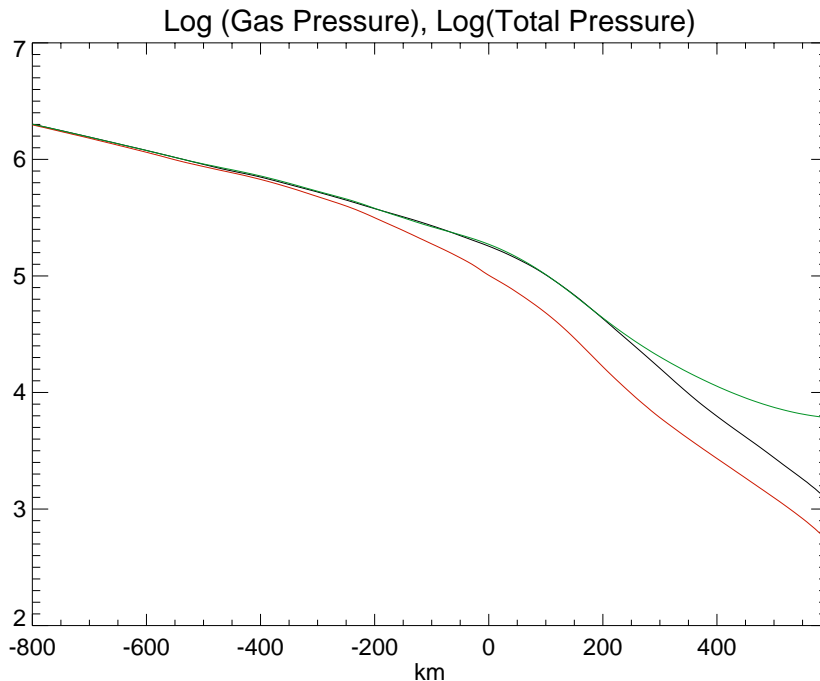
Figure 3.8: Horizontal average of gas and total pressure as function of height. The black line indicates the mean gas pressure averaged over regions with field strength smaller than 50 G. The red line shows the mean gas pressure averaged over magnetic flux concentrations, and the green line is for the total pressure over magnetic flux concentrations.

the atmosphere. The MHD profiles of B_z exhibit some structuring (variation) across the sheet's cross-section, which are not reproduced by the thin sheet model. This is because this latter model produces only symmetric profiles of B_z (Ferriz-Mas et al. 1989). The MHD profiles of B_z are asymmetric primarily in the sense that the left part exhibits larger values than the right part. This is associated with lower values of the pressure at these locations (Figure 3.6). Then B_z has to increase in order to keep P_{tot} balanced (see Figure 3.6). The pressure deficit is due to lower pressure plasma flowing downward in these regions (see Figure 3.10). This strong downflow is associated with convective dynamics where material that has cooled down radiatively becomes anti-buoyant and flows down. The variation of the B_z profile in the MHD case in the lower panel is significant (more than 600 G). This is an extreme case of the scenario described above which produces variations in B_z in order to keep p_{tot} balanced. It is large at this altitude because β has its largest value there (see Table 3.1), which implies that variations of P induce relatively larger variations of B_z compared to higher atmospheric layers.

The distribution of B_x for the thin flux sheet and the MHD case are shown in Figure 3.11. Here B_x is of third order (see section 1.2). The MHD plots are smooth for the three upper panels (relatively low β). For the lower panel we notice some fluctuations mainly due to the reasons we discussed earlier for $\beta \sim 1$, in addition to the fact that the convection

Table 3.2: Relative importance of the series-expansion

Geometrical height from reference [km]	-98	42	182	322	462
B2/B0	0.004	0.012	0.044	0.155	0.116
B3/B1	0.161	0.026	0.071	0.063	0.025

disturbs the field lines. These fluctuations of the magnetic field appear more pronounced for B_x comparing to B_z because of the relatively small amplitude of B_x. The fit between MHD and thin sheet model is relatively good for the three upper panels, and less good for the two lower ones. We notice for the three upper panels that there is a systematic offset between the MHD values and the thin sheet ones. This is due to the fact that the sheet is slightly inclined from a vertical position. Thus the absolute values of B_x through horizontal cuts are slightly higher at one side and slightly lower at the other side, which create this general offset.

B_z and B_x for the flux sheet can be written in a simplified way (see also equations 3.4 and 3.5):

$$B_z = B_{z0} + x^2 B_{z2} + x^4 B_{z4} + ... = B0 + B2 + B4 + ..., \tag{3.47}$$

$$B_r = x B_{r1} + x^3 B_{r3} + ... = B1 + B3 + ..., \tag{3.48}$$

We can compare the relative importance of successive terms in these series expansions. Table 3.2 indicates that $B2$-terms are significantly smaller than $B0$-terms. The importance of $B2$-terms is more pronounced in the upper part of the atmosphere. This is also noticeable in the upper panels of Figure 3.9. $B3$-terms are much smaller than $B1$-terms, and since $B0 > B1 > B2 > B3 > B4 > ...$, it is expected that the influence of the third-order terms on B_x is less marked than the second-order terms on B_z. This is clearly seen in Figures 3.9 and 3.11. This also confirms that neglecting the fourth-order terms in B_z is justified.
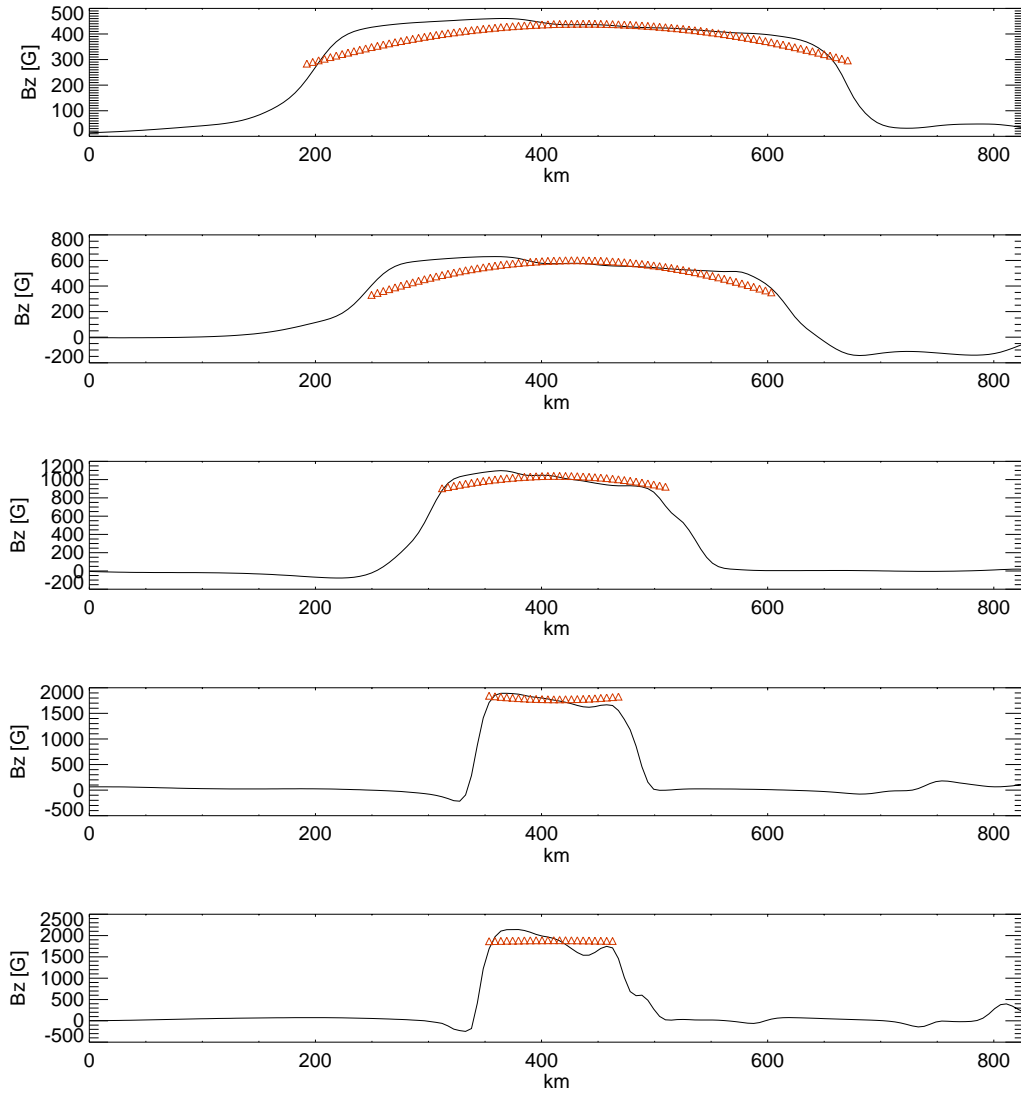
Figure 3.9: Vertical component of the magnetic field, plotted along the 5 horizontal lines in Figure 3.5. The orange triangles represent B_z in the case of a 2nd-order thin flux sheet model.
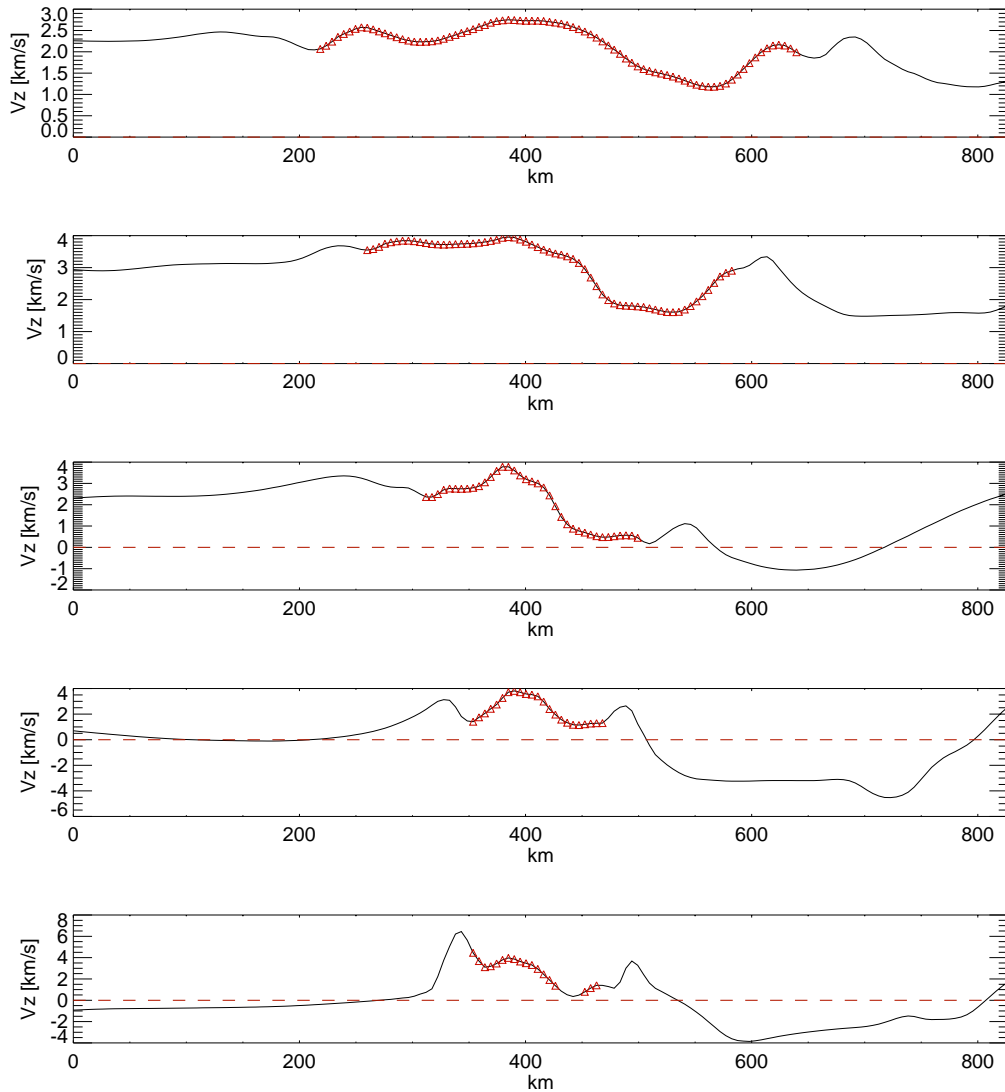
Figure 3.10: Vertical velocity plotted along the 5 horizontal lines in Figure 3.5. The orange triangles indicate the location of the flux sheet (where the field strength is higher than 75 percent of the maximum along the line).
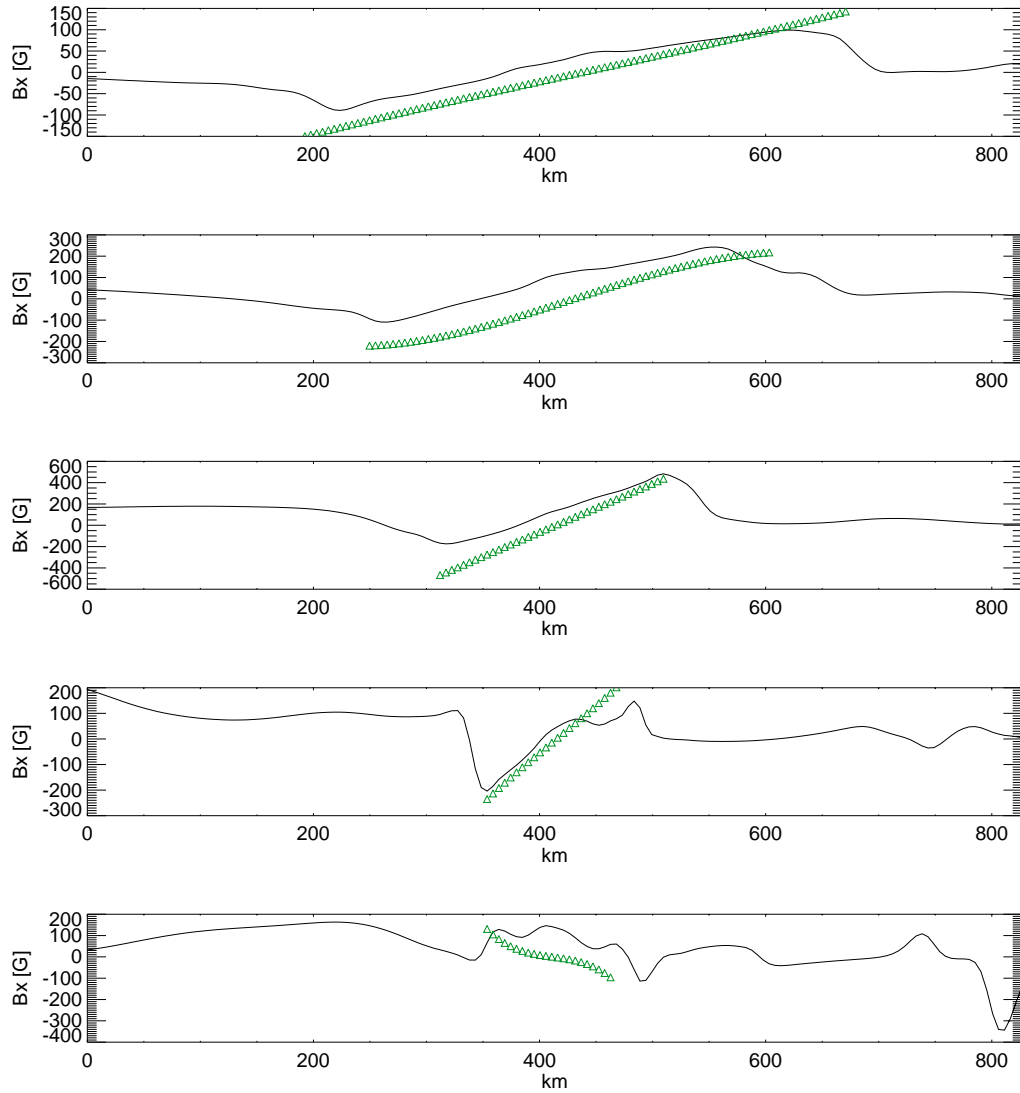
Figure 3.11: Horizontal component of the magnetic field across the flux sheet plotted along the 5 horizontal cuts in Figure 3.5. The green triangles represents B_x in the case of a 2nd-order thin flux sheet model.

3.5   Analysis of the total pressure in the whole simulation domain

We have seen in the case of a thin flux sheet, that the total pressure in the lower part of the sheet is of the same order as the external gas pressure (see the two lower panels in figures 3.6 and 3.7). In these regions the flux sheet is relatively thin. The relative width of the sheet is measured by comparison to the local scale height. At an altitude corresponding to the two lower panels the local pressure scale height is of the order of 200 km. In a static atmosphere, the condition P_{tot} roughly constant through the sheet, would be the consequence of a constant P and B_z through the sheet. Thus such a magnetic configuration could be modelled by a 0th-order flux sheet approximation. In the case of MHD simulations, we have seen that B_z is roughly constant but still has some fluctuations increasing with depth. In order to keep the balance of P_{tot}, variations of P are compensated by variations of $B^2/(8\pi)$. Since in the lower layers β is of order unity, variations of P are compensated by non-negligible variations of $B^2/(8\pi)$.

In the three higher panels of Figure 3.7 we see that the total pressure in the center of the sheet is higher than that at the boundaries. This is due to magnetic tension forces which play an increasingly important role with altitude (decreasing β). So, in the higher layers of the atmosphere, magnetic forces (magnetic tension and pressure) play a more and more dominant role comparing to gas pressure-forces, getting closer to a force-free equilibrium in the highest parts of the atmosphere. In such a case, magnetic pressure gradients are balanced by magnetic tension forces. Since magnetic tension forces are pointing inward, magnetic pressure gradient has to point outward. This results in higher values of B_z at the center of the sheet.

The properties described above have been so far discussed only in the case of a thin flux sheet. In order to have a more complete view of the situation for the rest of the simulation box, which includes thicker magnetic concentrations, we map the gas and total pressures at three heights (the lowest, the middle and the highest altitudes shown in Figure 3.5).

Figure 3.12 represents gas pressure at a geometrical height indicated by the lower horizontal line (at -98 km) in Figure 3.5. Locations where the magnetic flux density is higher than 500 G are outlined by dark contours. We notice that the gas pressure is higher at the centers of granules (see also Figure 3.2 for locations of granules and intergranules). This is a common pattern for convection cells formed by granules. So, hot plasma is rising up to the surface of the sun which forms granules; then this plasma cools down radiatively above the surface due to the dramatic increase of photons mean free path, thus energy can escape from the system radiatively. The relatively cooled plasma returns back to intergranular lanes (mass conservation). Notice that regions with higher magnetic flux density have lower pressure than the neighbouring intergranular lanes. This is due to the fact that stability requires the total pressure inside flux concentrations, precisely at the interface separating magnetic and non-magnetic plasma, to be equal to the gas pressure outside. Thus the gas pressure inside magnetic structures is lower than the external gas pressure.

The total pressure inside flux concentrations (Figure 3.13) at the same height as Figure 3.12 is roughly close to gas pressure outside, and does not vary significantly within
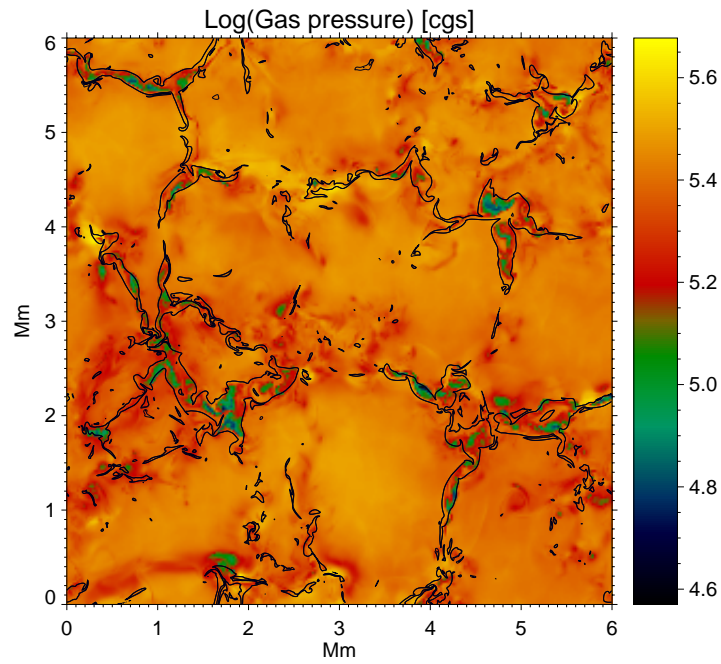
Figure 3.12: Gas pressure at a geometrical height of −98 km indicated by the lower line on Figure 3.5. The black contours enclose the regions where B_z is higher than 500 G.
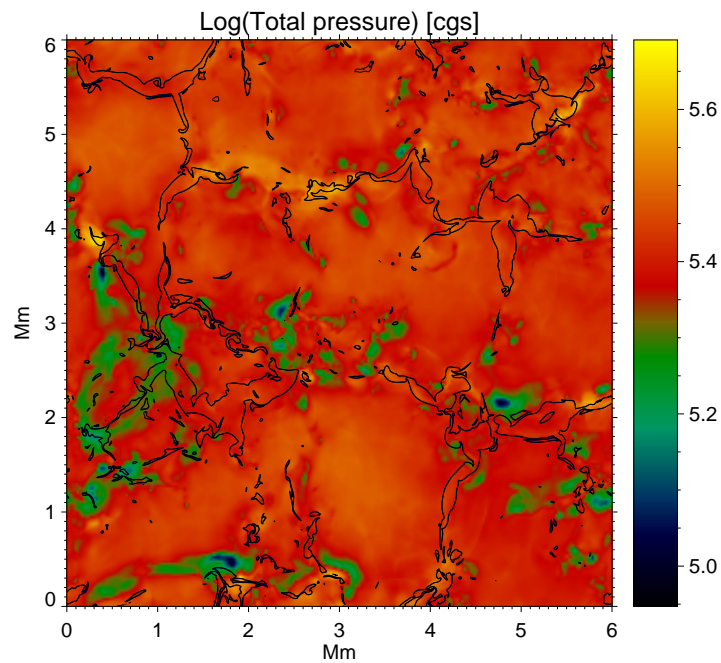

Figure 3.13: Total pressure (gas + magnetic pressures) at a geometrical height of −98 km.

each individual flux concentrations. As we have seen previously, this does not imply that B_z is constant, but rather that curvature forces are negligible in comparison to pressure

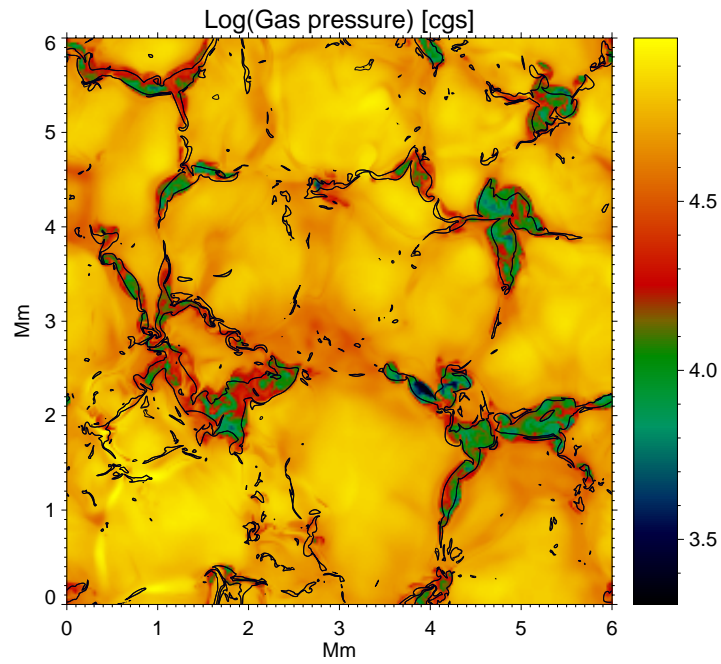Figure 3.14: Gas pressure at a geometrical height of 182 km, indicated by the third (starting from below) horizontal line in Figure 3.5.
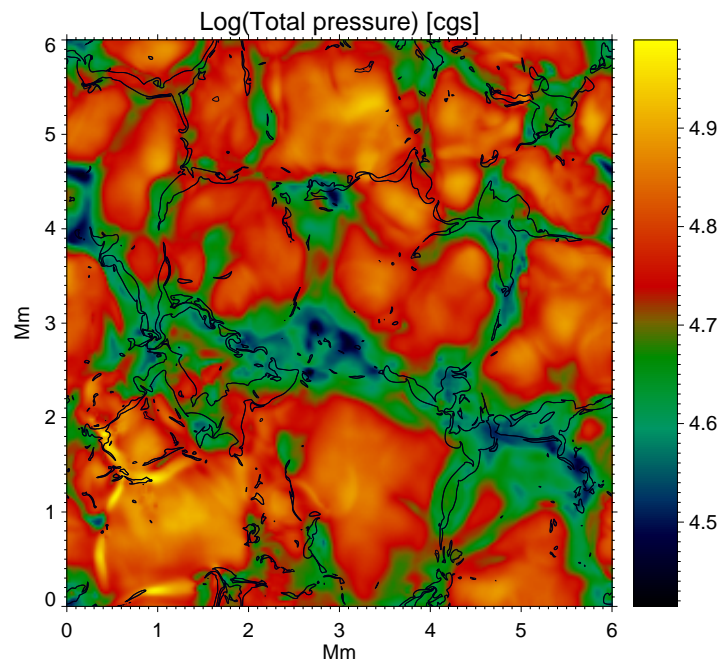

Figure 3.15: Total pressure (gas + magnetic pressures) at a geometrical height of 182 km.

forces. On the one hand, the relative constance of P_{tot} is an argument in favour of modeling flux concentrations using a 0th-order thin flux tube/sheet model. On the other hand,

Table 3.3: Standard deviations and mean value of P_{tot}

Altitude [km]	-98	182	462
Standard deviation of P_{tot} in non-magnetic regions (STD1) [cgs]	27703.0	9707.59	1055.04
Standard deviation of P_{tot} in magnetic regions (STD2) [cgs]	32709.4	7950.80	2151.41
Mean value of P_{tot} in non-magnetic regions (mean1) [cgs]	254220.0	57750.9	4901.33
Mean value of P_{tot} in magnetic regions (mean2) [cgs]	249696.0	47409.8	8626.20
STD1/mean1	0.108972	0.168094	0.215256
STD2/mean2	0.130997	0.167704	0.249405

the constancy of P_{tot} does not imply the constancy of B_z, it is a necessary condition (but not sufficient) for the 0th-order thin flux tube/sheet models.

The presence of the 2nd-order term (or higher-orders) will make the total pressure to have higher values at the center of flux concentrations. So, one way of measuring the importance of the second-order approximation (or higher-order) is to compute the standard deviation and the mean value of the total pressure inside magnetic elements and compare them to the corresponding values outside magnetic regions (see Table 3.3). Thus if (STD2/mean2)> (STD1/mean1) and mean2 > mean1, this can be interpreted as the presence of higher-order terms than the 0th-order.

At an altitude of -98 km (Figure 3.13), mean2 is slightly lower than mean1 because magnetic flux concentrations are located in intergranular lanes where the pressure at this altitude is slightly lower than the average pressure over the simulation domain. STD2/mean2 is larger than STD1/mean1, this does not result from higher-order terms, but rather indicates the presence of fluctuations inside magnetic elements. We notice also in Figure 3.13 the presence of regions with smoother variations than the average, e.g. the flux sheet at the top left corner which we studied in the previous section. Note that, in Figure 3.13, locations with particularly low total pressure are generally unrelated to magnetic flux concentrations. They are associated with strong downflows.

At higher altitudes (182 km), we see in Figure 3.14 that magnetic structures have expanded. The gas pressure has lower values in intergranular lanes, and particularly low values inside magnetic elements. The total pressure inside magnetic concentrations (Figure 3.15) is lower in intergranular lanes even when there is no (or low) magnetic field (e.g. the region around the coordinates (3Mm, 2.8Mm)). The mean value mean1 is higher than mean2 (table 3.3), for similar reasons as in lower altitudes. STD2/mean2 is similar to STD1/mean1, then the normalized fluctuations of P_{tot} inside and outside magnetic elements are similar. In this situation, there is no clear indication about the existence (or not) of higher-order terms than the zeroth-order. This rather shows that there is no predominant contribution from higher-order terms.

Near the top of the box, at a geometrical height of 462 km, indicated by the upper line in Figure 3.5, we notice that the total pressure has rather smooth variations (Figure 3.17) and increases towards the center of flux concentrations. This effect which we have already mentioned in the previous section for the case of a thin flux sheet, is even more pronounced in stronger flux concentrations. The plasma β is small at these heights, thus we get a nearly force-free equilibrium. At this height, mean2 is clearly larger than mean1 and STD2/mean2 is larger than STD1/mean1. This indicates that the total pressure is not a 0th-order function. This is clearly seen in Figure 3.17, which also shows that
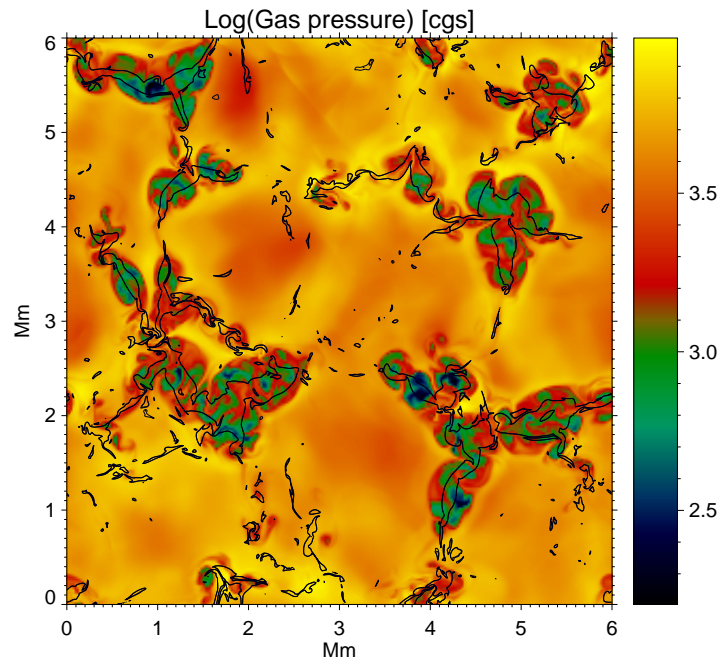
Figure 3.16: Gas pressure at a geometrical height of 462 km.
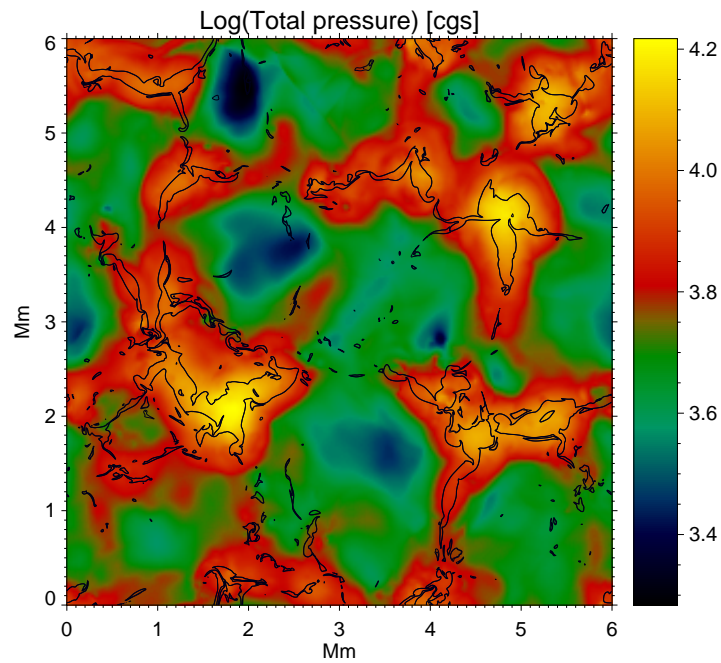
Figure 3.17: Total pressure (gas + magnetic pressures) at a geometrical height of 462 km.

we see this characteristic increase of P_{tot} only in magnetic flux concentrations and not in non-magnetic intergranular regions.

At this altitude, a zeroth-order thin tube/sheet model is not applicable anymore. We

have indeed seen in the case of a thin sheet that a second-order thin flux sheet approximation provides a reasonable fit. Nevertheless, before generalizing this conclusion, it is useful to proceed to a more quantitative study (especially for thick flux tubes). This will be done in the next section.

3.6   Analysis of a strong flux concentration

We saw in the previous section, that reasonable continuity and smoothness of total pressure, in the lower part of the atmosphere, is in favour of the applicability of the 0th-order thin flux tube/sheet approximation. We noticed also that the total pressure is of higher order than 0 in the upper part of the atmosphere. At these heights, the total pressure in the center of thick flux concentrations has the largest deviation compared to values in the weak-field regions. So the total pressure diagnostic brings some indications in favour of the thin tube/sheet model, but a more quantitative investigation is needed. In this section, we complete the investigation started earlier in the section on thin flux sheet. This includes a comparison between B_z and B_r from a thick MHD tube and from the thin tube model presented earlier. The criterions for the choice of a flux tube in the MHD simulations are primarily its width and a relative smoothness of P_{tot} across it. The selected flux tube is shown on Figure 3.18 (crossed by a dark line). We see at first that at this altitude the tube is split, which probably results from the history of its interaction with convection. We also notice that this "tube" has a cross-section which is far left out from a perfect circle.

The total pressure (Figure 3.19) is reasonably smooth, although P_{tot} through the lower panels exhibits more variations than the case of the thin flux sheet. The main reason for this is that the actual flux tube is located in a convectively more active region than the previous flux sheet (see velocity maps Figure 3.2). P_{tot} in the higher panels is smoother (lower β). The top panel exhibits a clear enhancement of P_{tot} towards the tube's center.

The thin flux tube model reproduces reasonably well the overall shape of B_z in the three upper panels (Figure 3.20). In the upper two, we notice the existence of a region with smoother decrease of B_z at the left edge of the flux tube. This results from a small neighbouring magnetic structure that merges with our main flux tube. It appears at the highest panels because its expansion with height makes it reach the location of the dark line (Figure 3.18) at these heights. We don't aim to reproduce this neighbouring structure, but only the main flux tube.

In the lower panels of Figure 3.20, we observe that the relatively thick flux tube is split into two parts. This is probably due to its interaction with convection and other neighbouring flux concentrations which make it evolve in time, sometimes in a complex manner. The two separate parts of the flux tube at the lower panel merge while expanding with height. It is interesting to notice that such flux concentrations in a complex convective pattern, still tend to behave like a single structure higher-up in the atmosphere. The merging process, and the decrease of β with height seems to produce a relatively smooth monolithic structure.

The radial component of magnetic field fits reasonably well with the thin flux tube model for the three upper panels (Figure 3.21). As we have seen before, the merging of a small neighbouring flux concentration with the main flux tube, makes B_r and B_z appear wider in the two upper panels. Nevertheless, the fit is reasonably good, since our aim is to model the main flux tube. We note in the three upper panels in Figure 3.21 that the 3rd-order contribution is much less marked than the 1st-order one.

Notice that the values of B_r vary from negative to positive when moving from the left to the right side through the panels. This is similar to the case of the thin sheet studied above. It comes here from the morphology of the tube, which has a fan-like structure
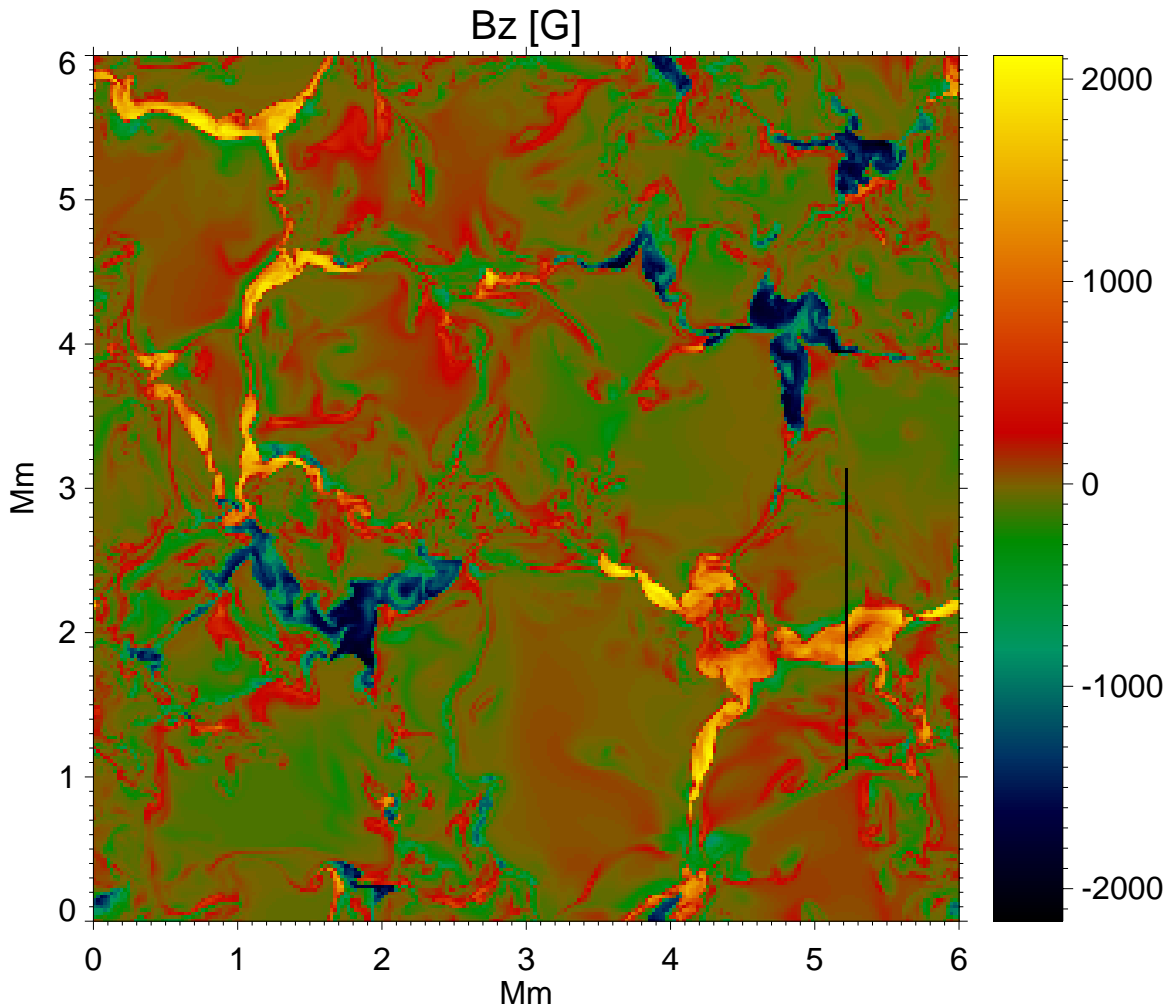
Figure 3.18: Vertical component of the magnetic field vector at a fixed geometrical height near the averaged visible solar surface ($\tau_{5000} = 1$), corresponding to an altitude of about 100 km. The dark line indicates the location where we make a similar treatment as in Figures 3.9, 3.11, and 3.6.

when expanding upwards. Thus, the angle between field lines and the vertical direction increases when moving from the center of the tube to its boundaries. Since **B** is parallel at each point to the field lines, the projection of **B** on the radial direction increases in amplitude when moving outward. The sign of B_r comes from the direction at which the field lines are pointing.

For the two lower panels B_r is irregular due to the double structure of the flux tube. In this case B_r from a thin flux tube model cannot be expected to reproduce the MHD one.
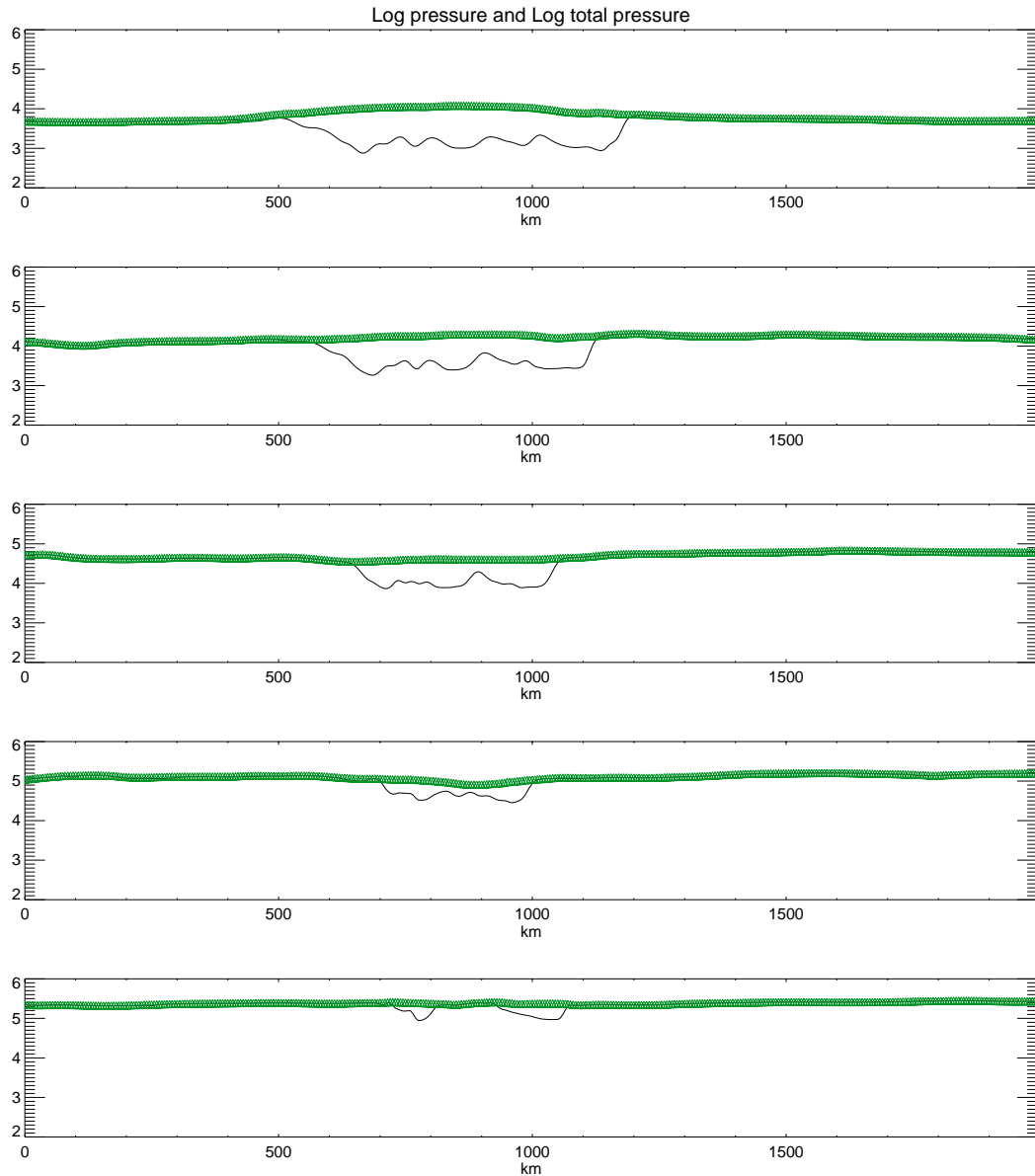
Figure 3.19: Profiles of gas pressure (in black) and total pressure (in green), plotted on a logarithmic scale along the dark line in Figure 3.18, at 5 geometrical heights (the same heights as used in the thin flux sheet case).

Figure 3.20: Vertical component of the magnetic field from the MHD data (in black), and from a thin flux tube model (in orange) plotted along the dark line in Figure 3.18. The 5 plots correspond to the same heights as in Figure 3.9.

Figure 3.21: Radial component of the magnetic field across the dark line in Figure 3.18. The black curves are from the MHD data, and the green ones are from a thin flux tube model.

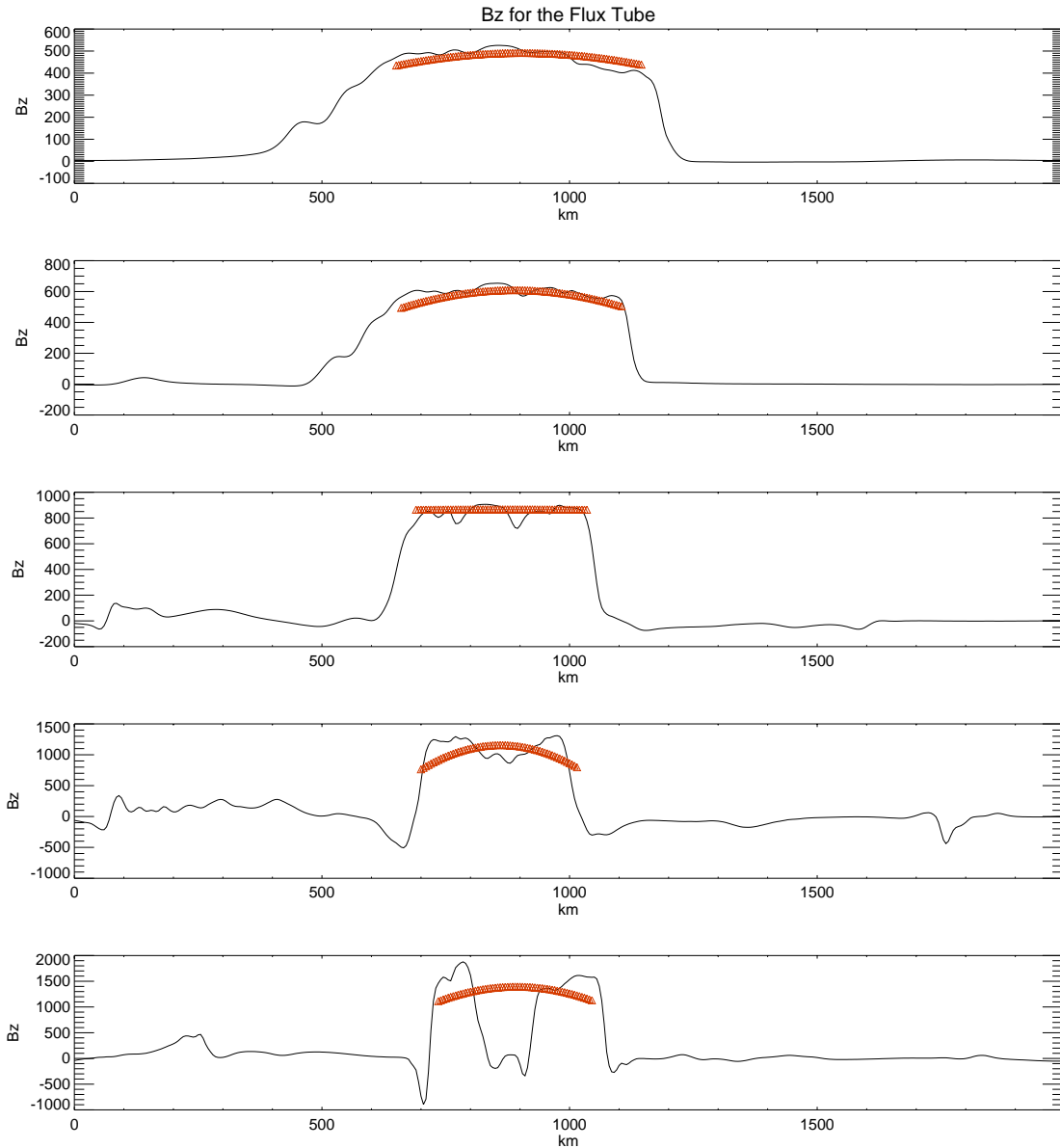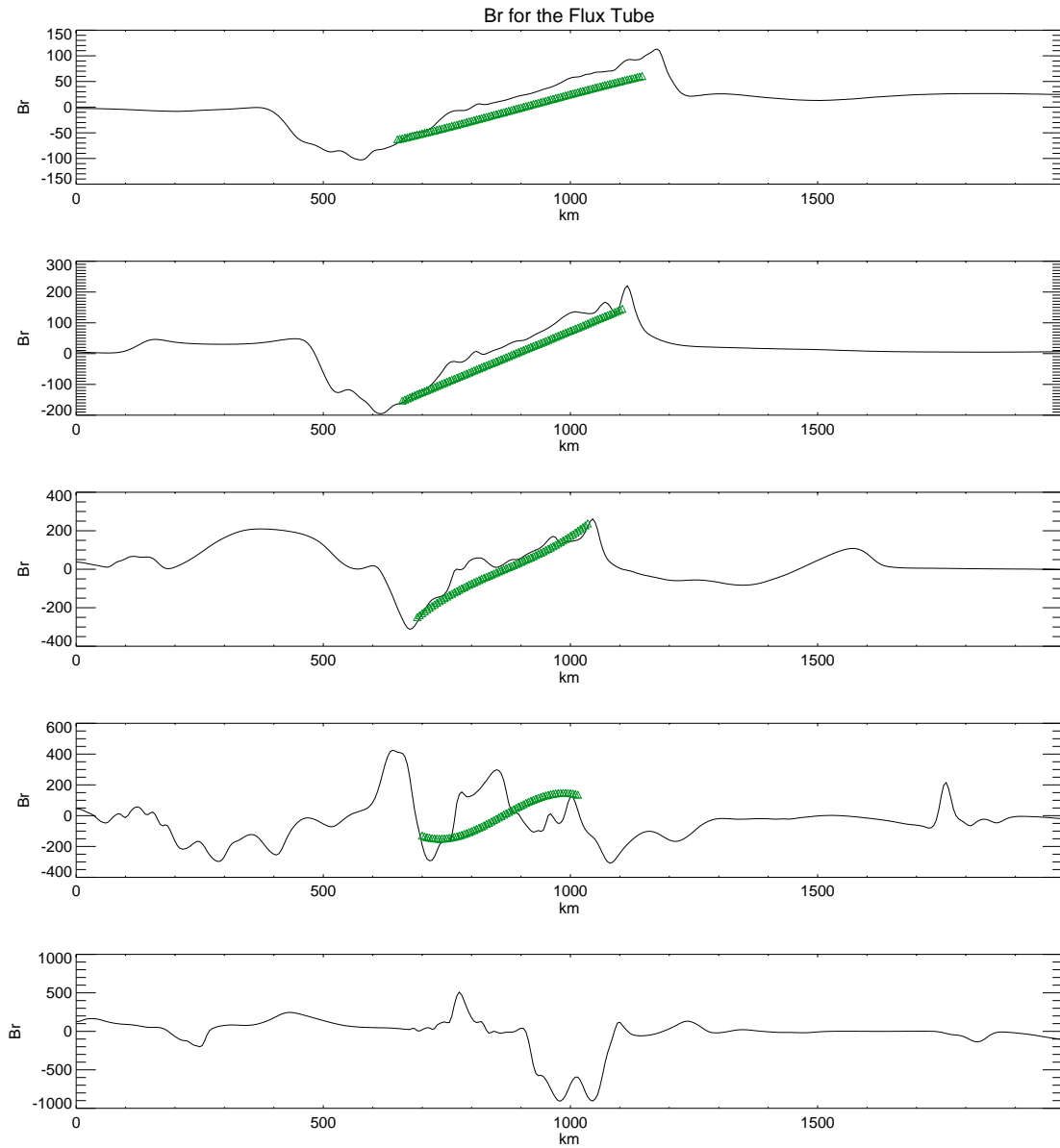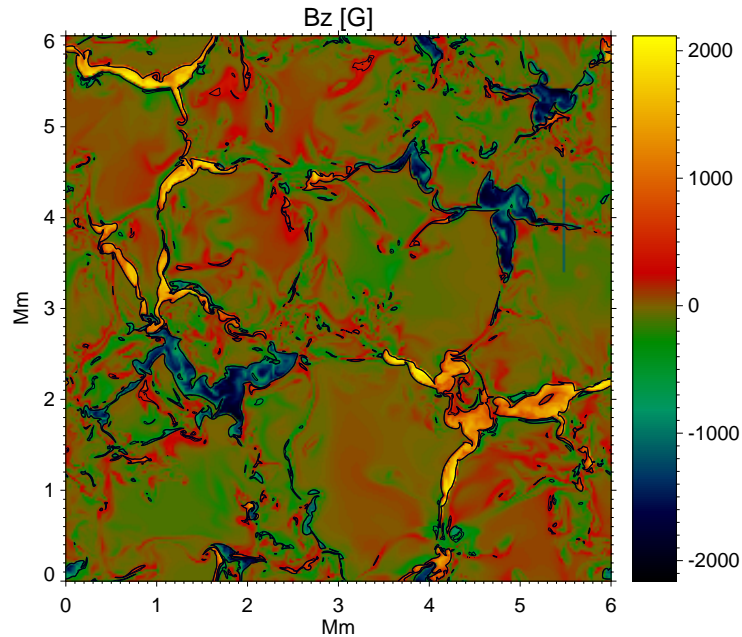Figure 3.22: Vertical component of the magnetic field at a fixed geometrical height near the averaged visible solar surface ($\tau_{5000} = 1$). The black contours outline the locations where B_z is higher than the equipartition field strength (> 450G). The blue line on the right part shows the location where we will plot a vertical 2D cut (Figure 3.24).

3.7   Very thin flux concentrations

In an ideal situation, the thin flux tube/sheet model presented earlier would be most suited to be compared to the thinnest flux concentrations in the MHD simulations. In that case the radius of the tube (or the width of the sheet) would be as small as possible comparing to typical length scales (e.g. pressure scale height). This picture would have been suited in and ideal case where flux tubes/sheets have an extremely thin boundary layer (separating magnetic and non-magnetic regions) and in the case of a steady plasma. The situation at the photosphere is clearly different. The dynamic state of the plasma at the photosphere induces considerable distortions to these very thin flux concentrations, especially for the ones separated from thicker flux concentrations (see Figure 3.22). Also, the radius of such small flux concentrations is no longer much bigger than the boundary layer thickness. As a consequence, the shape and flux density distribution of the thinnest magnetic elements may differ from a thin flux tube/sheet model.

In order for a flux concentration to evolve as a "coherent structure" in a plasma with density ρ and velocity V, the following condition should be satisfied :

$$\frac{B^2}{8\pi} \gg \frac{1}{2}\rho v^2 \tag{3.49}$$

where $B^2/(8\pi)$ is the magnetic energy density of the flux concentration. And $0.5\rho v^2$ is the kinetic energy density of the plasma.
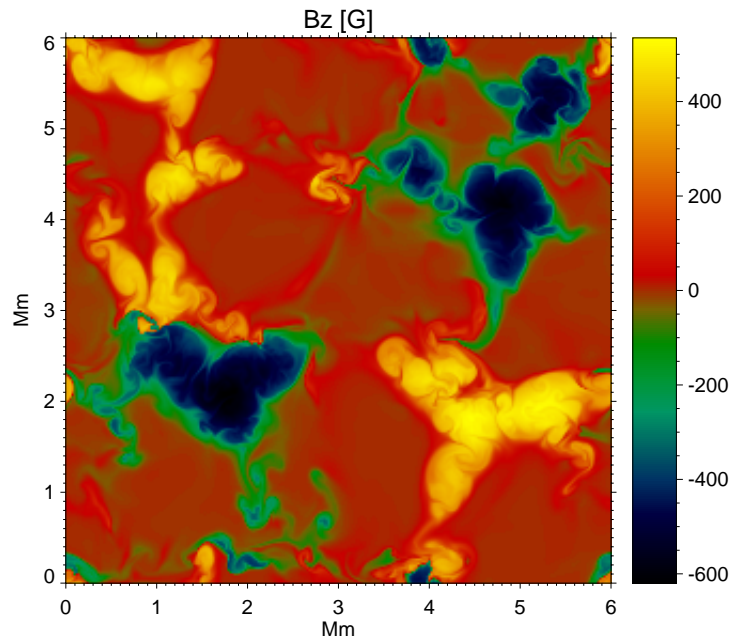
Figure 3.23: Vertical component of the magnetic field at a geometrical height of 462 km.

In a limit case, we expect a flux tube/sheet to be partially a coherent structure as soon as its magnetic energy density is bigger than the kinetic energy density of the plasma. Thus we set a threshold B_{eq} (equipartition field strength) above which a tube/sheet can be considered as partially coherent.

$$B > B_{eq} = v \sqrt{4\pi\rho} \qquad (3.50)$$

At the surface of the sun we have $B_{eq} \simeq 450 - 700$ G. This is a limit below which we cannot expect to obtain a structure coherent enough to be compared with the thin flux tube/sheet model.

In order to select very thin flux concentrations in the MHD data, we can thus set as a first criterion that $B > B_{eq} > 450$ G, (see contours on Figure 3.22). As second criterion, we require that the flux concentration remains coherent enough at higher altitude (see Figure 3.23). We might opt for a third criterion, which is that a flux concentration is not located at a region where close opposite-polarity fields coexist. Because at these locations, the field morphology gets complicated, and flux cancellation and reconnection occur, e.g. at the region located around the coordinates (1 Mm, 2.8 Mm), a reconnection occurs leading to the formation of a current sheet with a clear increase of temperature.

In Figure 3.22 we notice that some of the very thin flux concentrations (Type A) exist at the edge of bigger flux structures. Some others (Type B) are separate from larger flux concentrations. Although they are still distributed preferentially in intergranular lanes. In Figure 3.23 which represents B_z at a height of 462 km, we realize that most of type B very-thin flux concentrations are not noticeable anymore. They are mainly driven by the convection at lower layers, and have thus a poorly coherent structure. Whereas, some of type A structures keep a relatively coherent morphology. In cases where these structures
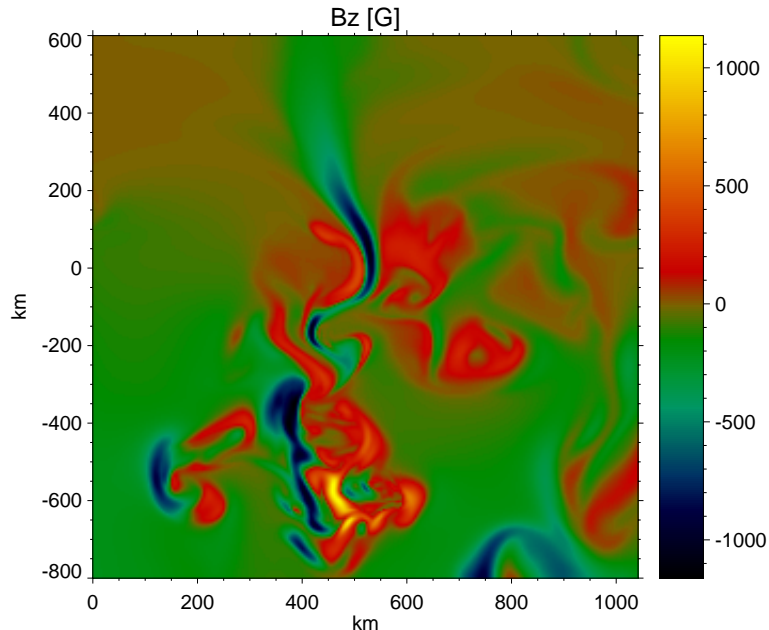
Figure 3.24: Vertical 2D cut in the MHD data showing B_z at the location of the blue line on Figure 3.22.

are too close to thicker flux concentrations they merge high up in the atmosphere, loosing then their identity. At this stage only a small fraction of very thin flux concentrations seems to fulfill all criteria. We will select one of them, at the location shown by the blue vertical line in Figure 3.22.

A lateral 2D view of this thin structure (Figure 3.24), shows that it is asymmetric and inclined. The dynamical state of the plasma drives partially this thin flux concentration, since the energy density is not far from equipartition. This is in disfavour of the representation of very thin flux concentrations in term of thin flux tube/sheet model.

3.8   Summary and conclusions

Throughout this chapter, we have done a comparative analysis between the thin flux tube/sheet model and flux concentrations existing in a 3D radiation-MHD simulation. These latter ones exhibit a wide range of sizes and shapes. We adopted two models (Thin flux tube and thin flux sheet) depending on the geometry of the studied flux concentration. We have seen that, for flux concentrations well above the equipartition distribution (see Sections 5.4 and 3.6) the models reproduces reasonably well the MHD structures. This was the case especially at the higher layers. The fits were less good in the lower part of the atmosphere due to higher β and the dynamical nature of the photosphere at these heights. In this case, it is rather the overall shape of B_z that is reproducible. The 2nd-order terms have a clear contribution to B_z in the thin flux tube/sheet approximation, especially in the upper part of the atmosphere. Whereas the 3rd-order terms bring only a relatively small contribution to B_x or B_r (Sections 5.4 and 3.6). In this case B_x and B_r are mainly

reproduced by the 1st-order terms in the thin flux tube approximation.

In the case of very thin flux concentrations with energy densities lower or of the order of the equipartition value, field lines are distorted and driven partly by the dynamic plasma. This leads to distorted or incoherent flux concentrations which do not have the necessary symmetry and regularity to be reproduced by a thin flux tube/sheet model.

4 Stokes polarimetry near the solar limb

4.1 Introduction

The study of small scale magnetic flux concentrations near the solar limb provides additional insight into the existing models of magnetic flux concentrations (Solanki et al. 1998, Frutiger et al. 2003). These flux concentrations have been associated with solar faculae. Understanding the physical processes behind solar faculae and their magnetic origin through observations and simulations has been the subject of many investigations (Lites et al. 2004, Keller et al. 2004, Carlsson et al. 2004, Steiner 2005, Hirzberger and Wiehr 2005, Okunev and Kneer 2005, De Pontieu et al. 2006). One of the motivations for studying the facular phenomena is the influence of their brightness on the Sun's irradiance variation (Fligge and Solanki 2001). From a spectropolarimetric point of view, it has been shown by Solanki et al. (1998) that a self consistent knowledge of the 3D structure of magnetic elements is necessary in order to model the observed Stokes signal near the solar limb. That is because an inclined ray which obliquely crosses a magnetic flux tube and its neighbouring non-magnetic regions, will be affected by the width of the flux tube, its horizontal (not only vertical) magnetic field distribution, and the properties of the plasma inside and outside the flux tube. E.g. the line-of-sight flows on both sides of the tube might have opposite directions for an inclined ray, so that their contribution to Stokes-V area asymmetry will have an opposite and often complex effect. This sensitivity of the asymmetry to the details of the atmosphere (e.g. Buente et al. 1993) makes it a good diagnostic for a self consistent 3D simulations of flux concentrations and their surrounding plasma.

Here we use fully compressible 3D radiation-MHD simulations (Vögler and Schüssler 2003, Vögler et al. 2005) to study some properties of Stokes profiles at disc center and at the limb. In the second and third sections we will make an investigation about the polarimetric signal emerging at two μ values, namely $\mu = 1$ and $\mu = 0.39$, respectively. A comparison between simulations and spectropolarimetric observations originating from a plage region at $\mu = 0.39$ is performed in the fourth section. The observations were recorded with the SOUP instrument at the 1-m Swedish Solar Telescope (SST) in 2006 by Rouppe van der Voort and van Noort.
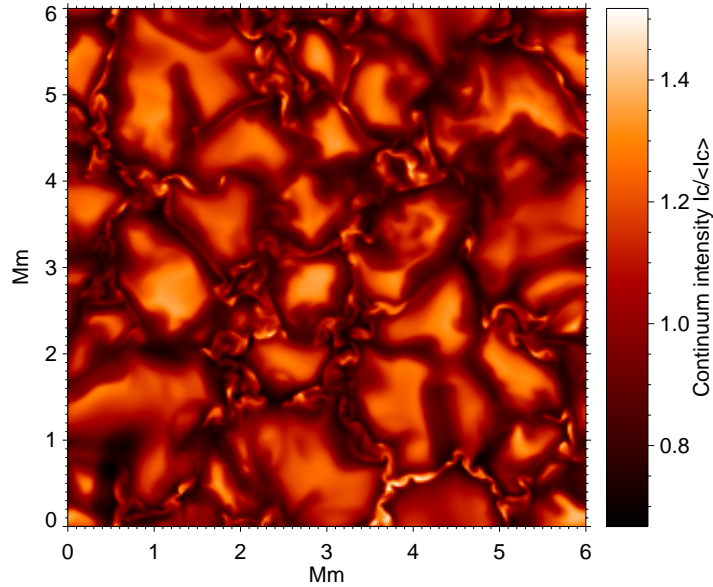
Figure 4.1: Normalized continuum intensity map near 6302 Å emerging from the simulation box at disc center.

4.2   Spectropolarimetric properties of a flux element at $\mu = 1$

4.2.1   Methods and simulations

The 3D radiation-MHD simulations used here include a solution of the fully compressible MHD equations, partial ionization in the equation of state and a non-local non-grey radiative transfer (Vögler and Schüssler 2003, Vögler et al. 2005). The MHD simulation box is 6x6 Mm in the horizontal plane and 1.4 Mm in the vertical direction, with a resolution of 576x576x100 grid points. The mean magnetic field strength is about 200 G. (See Figures 4.2 and 4.1). In these Figures we can see the fully developed granulation pattern which has interacted with the magnetic field. The flux gets concentrated in intergranular lanes as a result of flux expulsion (Weiss 1966, Galloway and Weiss 1981). The Stokes signal emerging from these 3D radiative-MHD simulations is computed using the STOPRO code in the SPINOR package (Solanki 1987, Frutiger et al. 2000). This gives the four Stokes profiles and the neighbouring continuum intensity (see e.g. Figure 4.1, which shows the continuum intensity map near 6302 Å).

4.2.2   Analysis of a flux element at $\mu = 1$

Spectropolarimetric studies of the properties of small scale magnetic flux elements have been carried out several times (e.g. Bellot Rubio et al. 1997, 1999a, Frutiger and Solanki 2001, Rezaei et al. 2007), for reviews see (Solanki 1993, Solanki et al. 2006). Most of these investigations were conducted at disc center $\mu = 1$ and assume different levels of
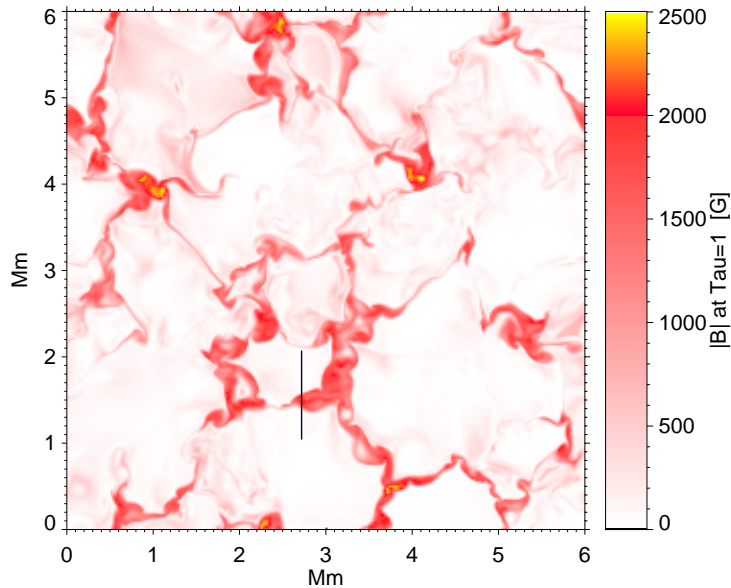
Figure 4.2: Magnetic field strength map at optical depth $\tau_{5000} = 1$. The dark vertical mark (in the lower part) indicates the location where we made the 2D vertical cut shown in Figure 4.3.

sophistication regarding the atmospheric models. We aim here to probe some properties of Stokes profiles (such as their asymmetries) in terms of the mechanisms producing them in 3D MHD simulations. This first part will be restricted to disc center.

Figure 4.3 represents a vertical 2D view along a cut in a flux element at the location indicated by the dark line in Figure 4.2. The magnetic field strength is shown in the left panel. The line-of-sight velocity map (right panel) indicates the existence of down-flowing plasma (shown in red i.e. red shifted) just outside the flux tube, and up-flowing plasma further away. This is a quite general situation where the upflowing plasma at the center of granules, cools down radiatively, and flows down at inter-granular lanes just outside the flux tubes (Solanki 1989). The total Stokes circular (TCP) and linear polarizations (TLP) are defined as:

$$TCP = \int |V| d\lambda, \tag{4.1}$$

$$TLP = \sqrt{\left(\int |Q| d\lambda\right)^2 + \left(\int |U| d\lambda\right)^2}. \tag{4.2}$$

The distributions of TCP and TLP coming out of the atmospheric slice in Figure 4.3 are shown in Figure 4.4 (two upper panels). The vertical dashed lines indicate locations where we carried out a ray analysis (shown in Figure 4.6). The Stokes-V area asymmetry (δA), and amplitude asymmetry (δa), are respectively defined as:

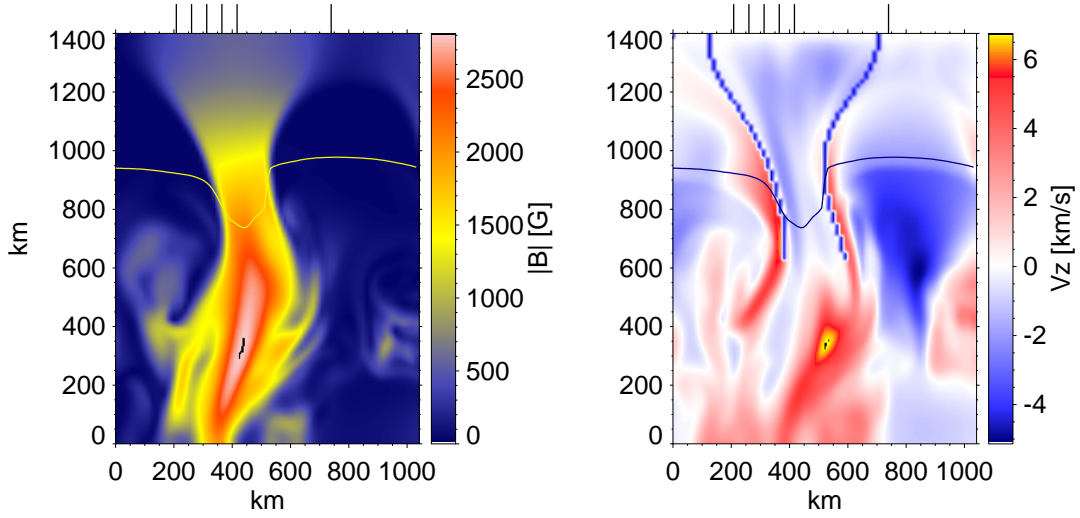$$\delta A = (A_b - A_r)/(A_b + A_r), , \tag{4.3}$$

Figure 4.3: 2D vertical cut of a flux element at the location indicated by a black line on Figure 4.2. The magnetic field strength is shown in the left panel. The line-of-sight velocity is represented in the right panel, where red and blue shifts are represented in red and blue colours respectively. The optical depth $\tau = 1$ is shown by the yellow and blue lines. The boundaries of the flux element are highlighted in blue in the velocity panel. The small vertical lines on the top of the two images indicate the locations of some rays analysed in more detail in Figure 4.6

$$\delta a = (a_b - a_r)/(a_b + a_r),, \tag{4.4}$$

where A_b, A_r denotes the area, a_b,a_b the amplitudes of the blue and red wings of Stokes-V profiles, respectively.

The distribution of the TCP (Figure 4.4) has maximum values for rays crossing the central part of the flux tube where the line-of-sight component of the magnetic field is maximum. The amplitude of the TLP is much smaller than the TCP one, and has a double peak structure. It is maximum at rays crossing the sides of the flux tube where the transverse component of the magnetic field is maximum. The curves representing the TCP and TLP without magnetooptical effects are represented by triangles. The distribution of the TCP is not affected by magnetooptical effects, whereas the TLP is affected at the location where the TCP is maximum. Note that the central part of the TLP is not zero in both cases. This indicated that this non-zero value is not due to magnetooptical effect but to a slight deviation of the magnetic flux element from a vertical orientation.

The area and amplitude asymmetries are shown in Figure 4.4 along the atmospheric slice marked in Figure 4.3. They reach their maximum along rays which cross magnetic regions (canopy-like) in the upper parts of the atmosphere and non-magnetic dowflowing regions in the lower part of the atmosphere (mainly above the optical depth unity line in Figure 4.3). A similar scenario as Figure 4.4 has been observed with HINODE's SP (Rezaei et al. 2007). The simulated δA has a maximum amplitude of 0.46 while the observed ones have an amplitude up to 0.25. This difference is partly due to the effect of
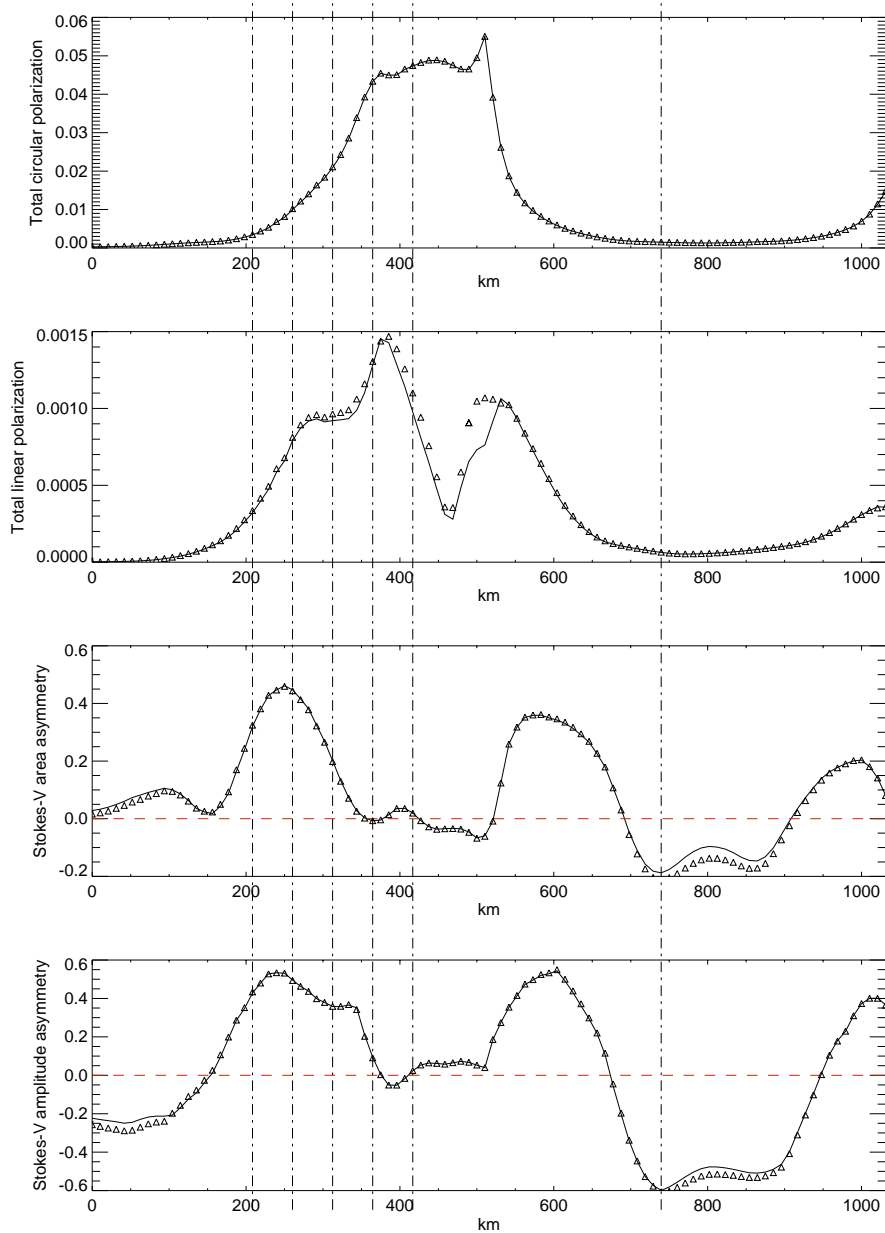
Figure 4.4: From top to bottom (in full lines): Total circular polarization, total linear polarization, Stokes-*V* area asymmetry, and Stokes-*V* amplitude asymmetry, all plotted along the black line on Figure 4.2. The curves indicated with triangles represent the same plotted quantities but calculated without magnetooptical effects. The vertical dash-dotted lines indicate the same locations shown by vertical lines in the previous figure.

the spatial averaging on the asymmetry properties of the Stokes-*V*. The average values of the asymmetries displayed in Figure 4.4 are: $\langle \delta A \rangle = 0.090$ and $\langle \delta a \rangle = 0.016$. The averaged Stokes profiles over the profiles outgoing from the atmospheric slice in Figure 4.3 are shown in Figure 4.5. The asymmetries for the averaged Stokes-*V* in Figure 4.5 are: $\delta A = 0.063$ and $\delta a = 0.130$. These values are slightly higher than the ones reported in Marinez
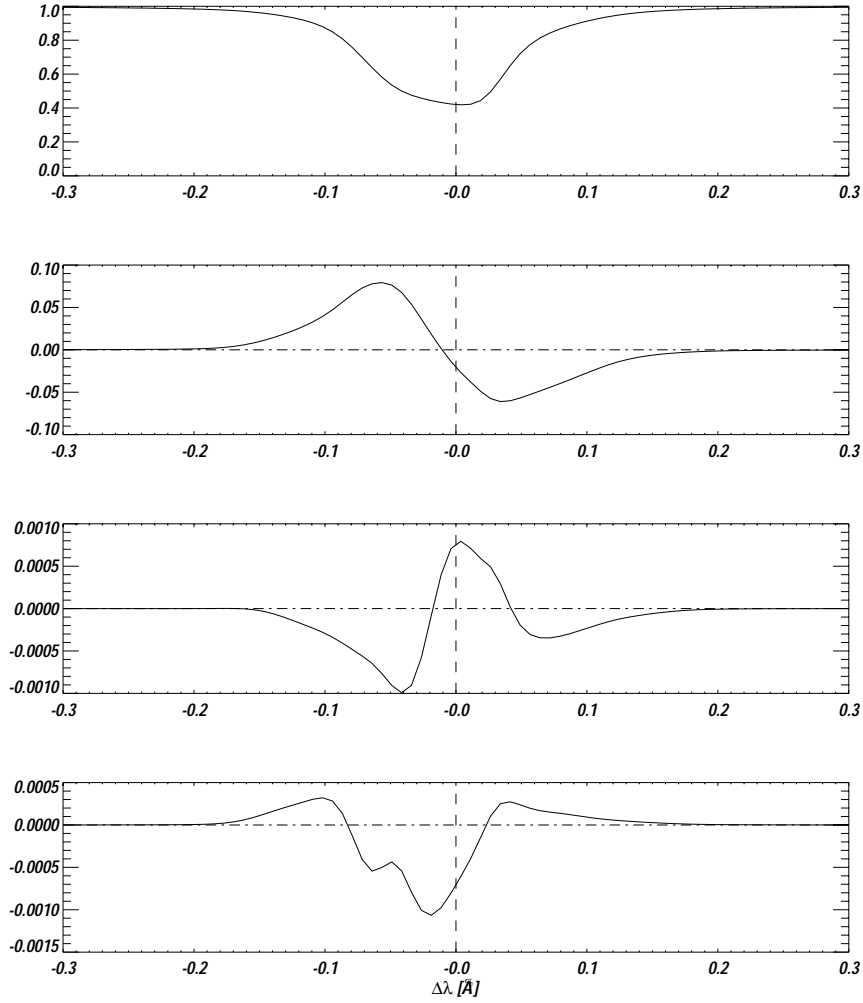
Figure 4.5: From top to bottom: Stokes-I, V, Q and U. The displayed profiles are the averages over the 100 Stokes profiles formed along the atmospheric slice in Figure 4.3

Pillet et al. 1997. In this latter work, it is found that at disc center, $\delta A \simeq 0.04$ and $\delta a \simeq 0.09$. We argue that applying an appropriate spatial and spectral degradation to the simulated data (to simulate the observation conditions) will decrease the simulated asymmetries. This might bring a better agreement between simulations and observations.

A closer look at individual rays is shown in Figure 4.6 along the six positions indicated in Figures 4.3 and 4.4. The six columns correspond to (from left to right) the line-of-sight magnetic field (B_{LOS}), the line-of-sight velocity (V_{LOS}), (-1) times the τ-derivative of B_{LOS} times the τ-derivative of V_{LOS}, Stokes-I, Stokes-V and Stokes-Q. The uppermost panel (leftmost ray), has a redshifted Stokes-I profile and positive Stokes-V asymmetries δA and δa. The existence of positive values of δA is consistent with the condition discussed in Illing et al. (1975) or Solanki and Pahlke (1988), (see also Solanki 1993):

$$-\frac{d|B_{LOS}(\tau)|}{d\tau}\frac{d|V_{LOS}(\tau)|}{d\tau} \geq 0 \Rightarrow \delta A \geq 0, \qquad (4.5)$$

$$-\frac{d|B_{LOS}(\tau)|}{d\tau}\frac{d|V_{LOS}(\tau)|}{d\tau} \leq 0 \Rightarrow \delta A \leq 0 \tag{4.6}$$

This is shown in the third panel, where we notice positive values in the region of formation of the Stokes signal. Thus the ray crosses the left part of the flux tube through the canopy region which is just above a field-free region where the plasma is downflowing. A similar scenario has been examined in two-layer models, and has been shown to produce Stokes-V asymmetry (Solanki and Pahlke 1988, Grossmann-Doerth et al. 1988, 1989, Steiner 2000).

The second and third rays (from top to bottom in Figure 4.6; and from left to right in Figures 4.3 and 4.4) exhibit also positive Stokes-V asymmetries produced by a similar mechanism as along the previous ray. The Stokes-V signal is stronger in the second and third rays, because the rays cross the flux tube at optical depth regions closer to the maximum of the line formation height range, which also corresponds here to regions of higher magnetic flux density. The fourth and fifth rays cross only magnetized plasma inside the flux tube. Both rays are mainly located along upflowing plasma regions, except for the near continuum part of the fourth ray which comes from a downflowing region (see Stokes-I near the continuum for the fourth ray, and the corresponding τ-distribution of the velocity). In these two rays, V_{LOS} and B_{LOS} gradients, shown in the third column, are experiencing positive and negative values in the line formation regions (roughly at $\log\tau \in [-1, -3]$). The existence of two opposite signs of the gradient of V_{LOS} and B_{LOS} is to be taken with special care. Indeed, in the presence of two different signs of the gradient, the final sign of the asymmetry depends on how much "weight" is given to each part of the gradient function. This depends in a non trivial way on the contribution of each atmospheric layer to the line formation.

In the center of the flux tube, we found low values of the asymmetries or even negative values. This is consistent with previous results by Rezaei et al. (2007) and their Hinode observations. A closer look at the conditions along the fourth and fifth rays can explain the reasons why we find such low values of the asymmetries. We need to consider two main points : 1) The main part of the line is formed in regions (roughly at $\log\tau \in [-1, -3]$) where the plasma is essentially moving in the same direction with relatively small deviation from its mean velocity. 2) The Zeeman splitting of the line (see the separation of the two lobes of Stokes-I) has values much larger than the deviation of the Doppler shift around its mean value. Thus the two σ components of the line experience a quite small change in their Doppler shift (comparing to the Zeeman splitting) along each ray. Thus none of the two σ components experiences any significant preferential (comparing to the other one) increase of the absorption coefficients due to Doppler shifts. The dependence of the asymmetry on the relative difference between the Zeeman shift and the Doppler shift was first explained by Grossmann-Doerth et al. (1989). Rays 4 and 5 in Figure 4.6 would fall in the category of "significantly larger Zeeman splitting comparing to Doppler shift" in the framework of Grossmann-Doerth et al. (1989). The fact that the plasma moves as a whole produces a shift of the line center and zero-crossing of the Stokes-V profiles (see Figure 4.6). The existence of downflows or upflows inside the flux tubes does not change the above analysis. It would induce a shift of the zero-crossing of Stokes-V mainly in the rays crossing only inside the tube. As a matter of fact, most of the flux concentrations in our MHD simulation harbour some small amplitude downflows inside them. This is
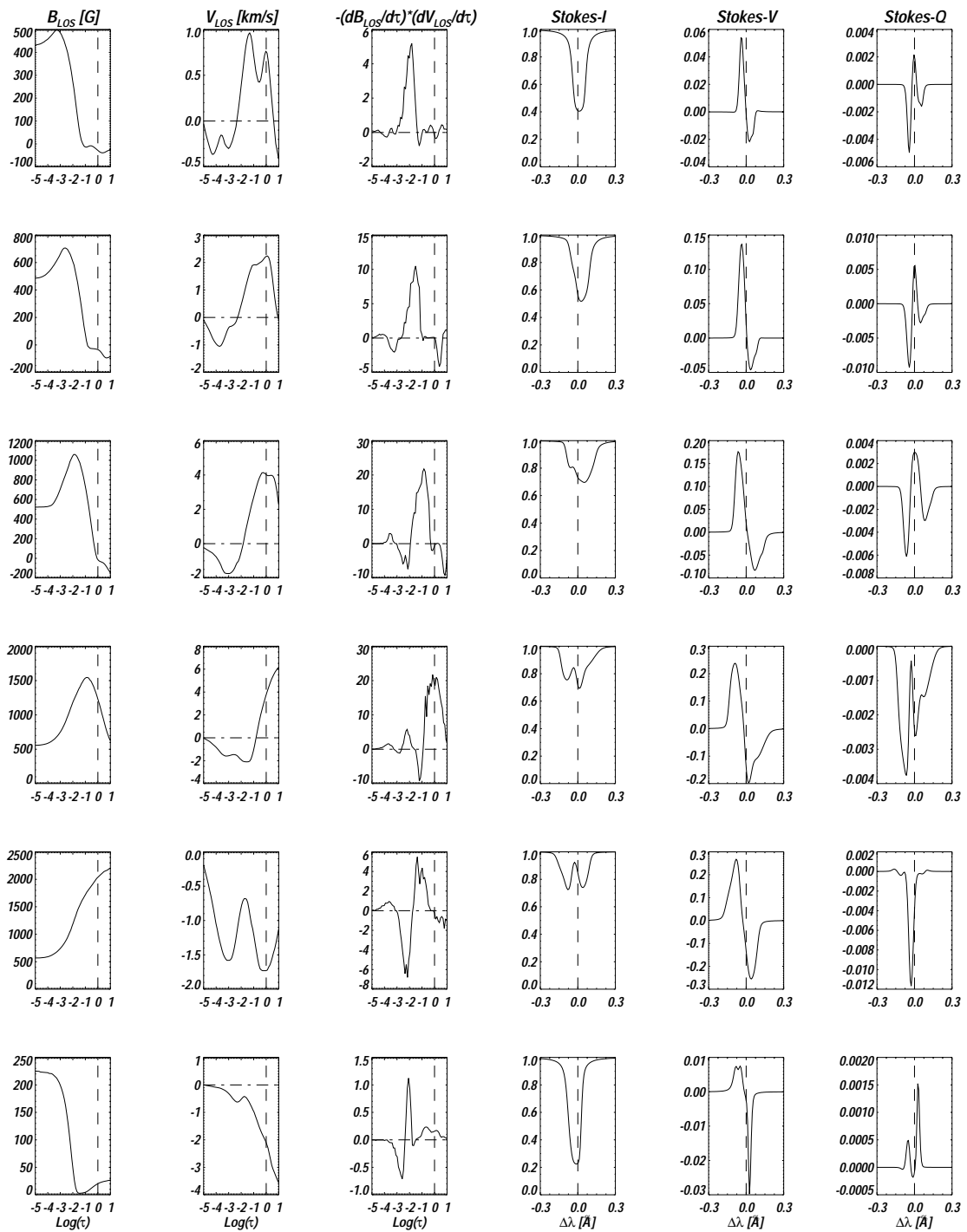
Figure 4.6: From left to right: Magnetic field strength along individual rays, line-of-sight velocity along individual rays, (-1) times the τ-derivative of B_{LOS} times the τ-derivative of V_{LOS}, Stokes-I, Stokes-V and Stokes-Q. Positive velocity corresponds to a redshift, and negative velocity is for a blueshift. The locations of these six rays are indicated in Figure 4.3 and Figure 4.4

consistent with observations (Grossmann-Doerth et al. 1996, Martínez Pillet et al. 1997, Sigwarth et al. 1999, Rezaei et al. 2007). The sixth ray lies far from the magnetic flux concentration. It crosses the canopy region above $\log(\tau)=-2$, and also passes through upflowing plasma from the neighbouring granule. This has produced a negative value of δA and δa. The polarized signal has a weak amplitude in this region comparing to the previous ones.

Figure 4.7: 2D inclined view at $\mu = 0.39$ of the magnetic flux element shown in Figure 4.3. The magnetic field strength is shown in the left panel. The line-of-sight velocity is represented in the right panel, where red and blue shifts are represented in red and blue colours respectively. The optical depth $\tau = 1$ is shown by the yellow and blue lines. The boundaries of the flux element are highlighted in black in the velocity panel. The small vertical lines on the top of the two images indicate the locations of rays analysed in more detail in Figure 4.11
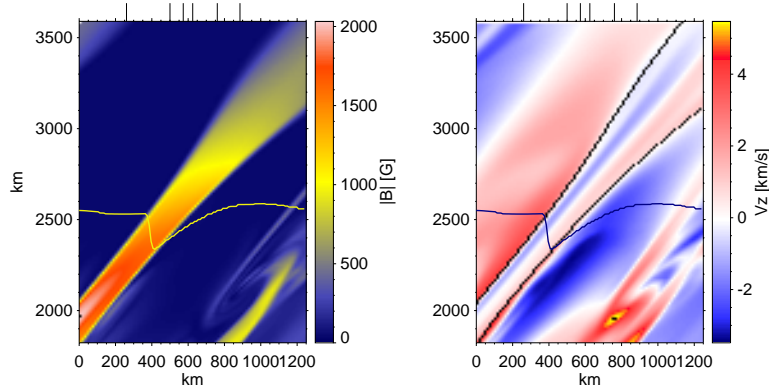
4.3   Spectropolarimetric properties of a flux element at $\mu = 0.39$

We proceed now to a similar analysis as in the previous section, but for simulations inclined with an angle of 67° corresponding to $\mu = 0.39$. This angle was chosen to compare with observations made with the SST at the same μ. The inclined view of the simulation box is constructed by interpolating the different physical quantities along rays with the desired inclination angle (Zakharov 2006). The grid step of 14 km along each inclined ray is the same as in the original MHD cube at $\mu = 1$. As consequence, the new inclined MHD cube is $576 \times 576 \times 100/\mu$ grid points. In the representation shown in Figure 4.7, rays crossing the atmosphere with an angle of 67° are represented vertically, so that the flux tube appears tilted. Figure 4.7 shows an inclined view of the flux element shown in Figure 4.3. Since now each ray has a length of 3590 km ($14 \times 100/0.39$ km), we show only the upper part of the tilted MHD slice in order to focus on regions where the Stokes signal is formed. At an inclination angle of 67° (Figure 4.7), many rays will get contributions to the computed spectral line from both sides of the flux tube. The field-free plasma outside the flux tube follows the granulation dynamics. I.e. it moves towards the flux tube from both sides, so that it appears as red-shifted motion of the field-free plasma (along the inclined rays) at the disc-center-side of the flux tube (red coloured velocity in Figure 4.7).
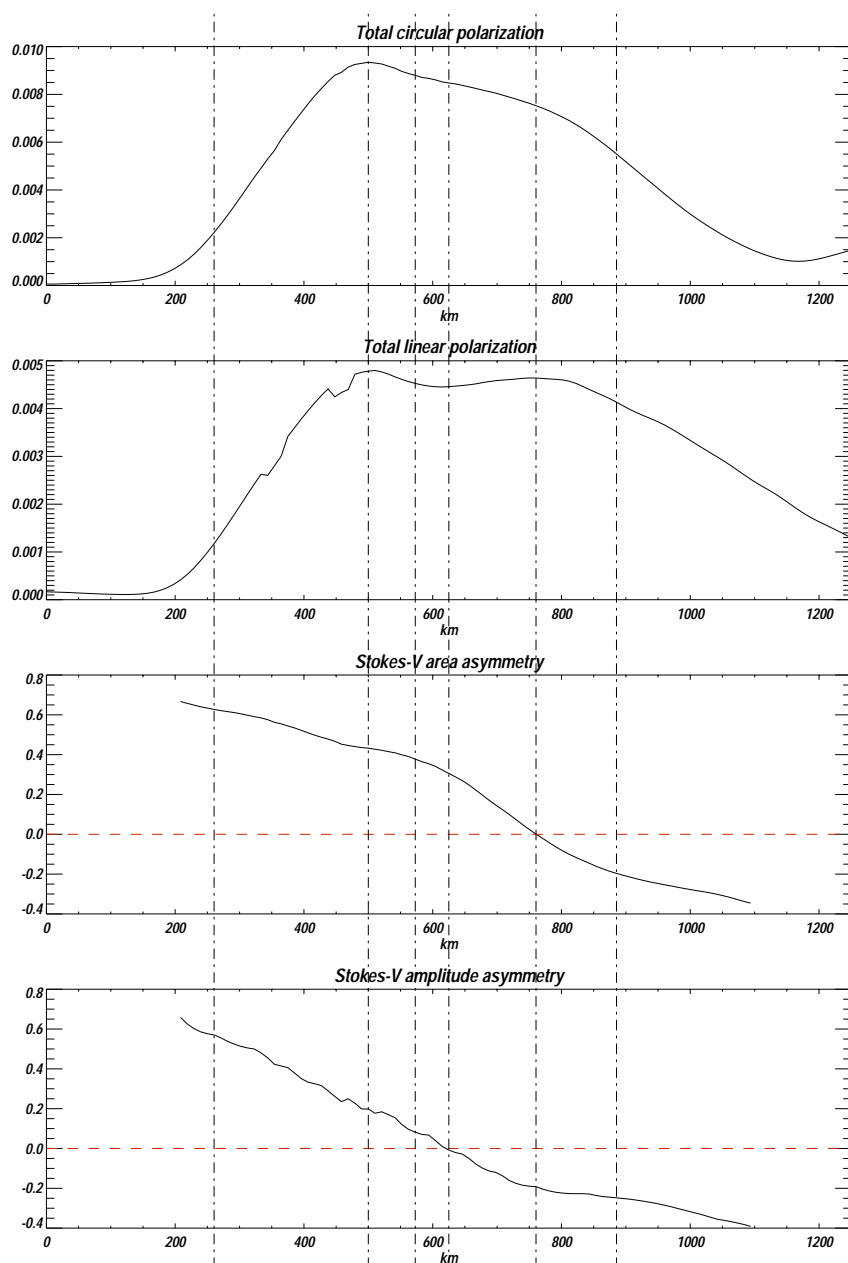
Figure 4.8: From top to bottom : Total circular polarization, total linear polarization, Stokes-V area asymmetry, and Stokes-V amplitude asymmetry, all plotted along the atmospheric slice in Figure 4.7. The vertical dash-dotted lines indicate the same locations shown by vertical lines in the previous figure.

Similarly, the plasma at the limb-side of the flux tube has a dominant blue-shift.

In Figure 4.8, we plot the total circular polarization, the total linear polarization, δA, and δa along the atmospheric slice in Figure 4.7. The six vertical dash-dotted lines indicate locations at which we analyse single rays in greater detail (Figure 4.11). The polarized Stokes parameters obtain a contribution only where $B \neq 0$. The total circular polarization and total linear polarization in Figure 4.8 have maximum values when the location of

Figure 4.9: From top to bottom: Stokes-*I*, *V*, *Q* and *U*. The displayed profiles are the averages over the Stokes profiles formed along the atmospheric slice in Figure 4.7

the flux tube along rays corresponds to the locations of maxima of the response functions of the line-of-sight and transverse components of the magnetic field, respectively. Unlike the situation at disc center, here the total circular and total linear polarizations curves have somewhat similar shapes. This is due to the fact that a variation of |B| implies a proportional variation of both, the the line-of-sight and transverse components of the magnetic field.

We notice that the asymmetries δA and δa vary from positive to negative values when rays cross the flux tube at increasing heights. This is different from the disc-center case where the asymmetries are mainly positive across the flux tube (Figure 4.4). The mean values of the asymmetries displayed in Figure 4.8 are: $\langle \delta A \rangle = 0.186$ and $\langle \delta a \rangle = 0.049$. The averaged Stokes profiles over the atmospheric slice are shown in Figure 4.9. The asymmetries for the averaged Stokes-*V* are: $\delta A = 0.213$ and $\delta a = 0.258$. These positive and relatively large values are due to statistical averaging effect. Figure 4.10 represents the averaged Stokes signal over the full row (576 Stokes profiles) to which belongs the
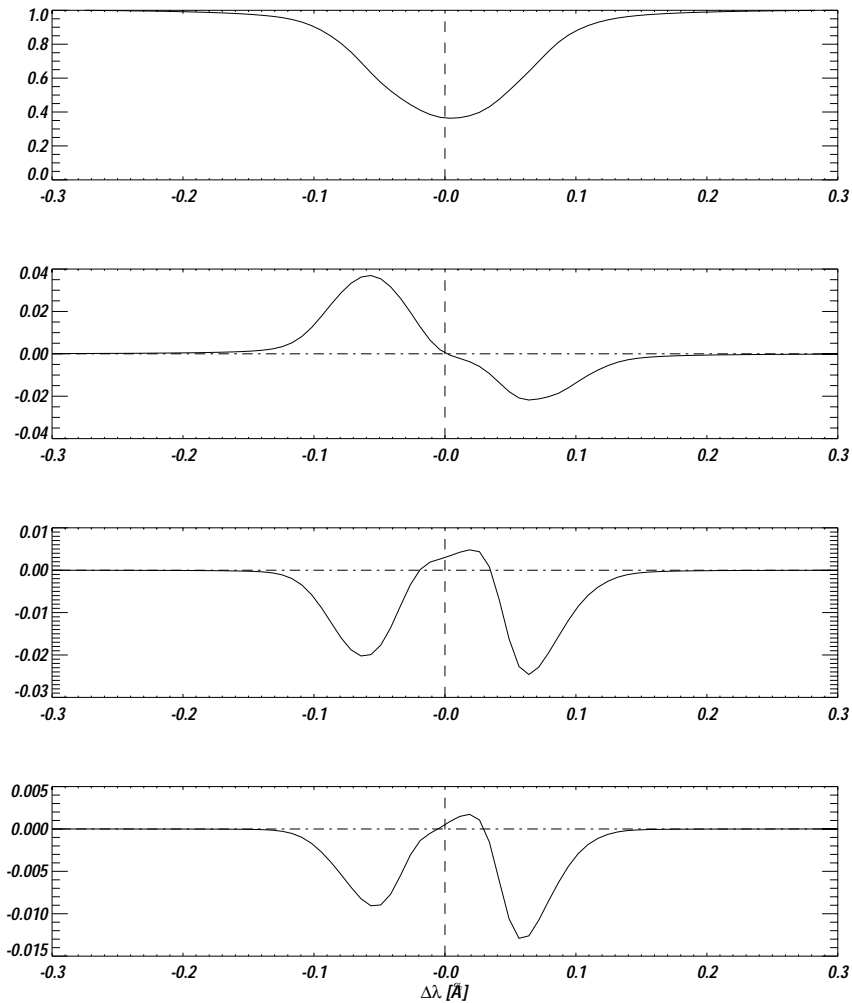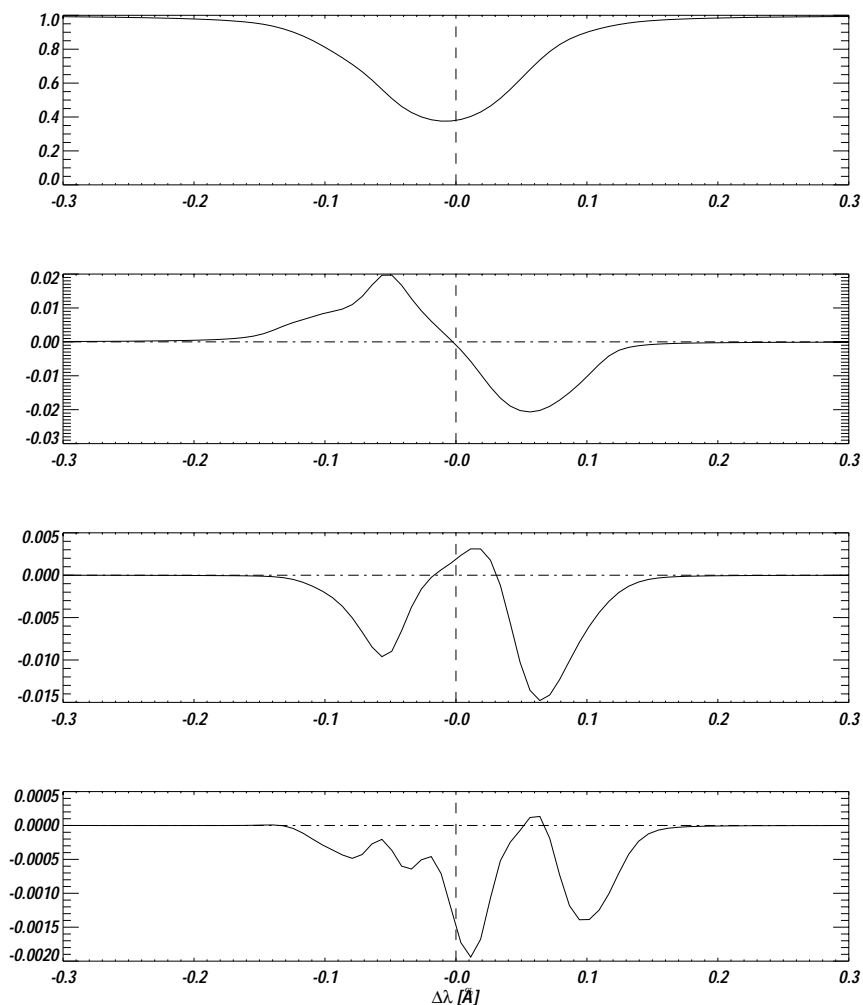
Figure 4.10: From top to bottom: Stokes-I, V, Q and U. The displayed profiles are the averages over the 576 Stokes profiles formed along the row in the MHD data to which belongs the magnetic element shown in Figure 4.7

magnetic element shown in Figure 4.7. The asymmetries of the Stokes-V profile displayed in Figure 4.10 are: δA = -0.063 and δa = -0.024. These values are still subject to statistical averaging effect but are closer to the observed values than the previous ones. The observed center-to-limb variations of δA and δa (e.g. Stenflo et al. 1987, Martínez Pillet et al. 1997) exhibit a change in the sign of the asymmetries in active region close to the solar limb. In Martínez Pillet et al. (1997), the authors report that at $\mu = 0.39$, $\delta A \simeq$ -0.03 and $\delta a \simeq 0.007$. The asymmetries of the Stokes-V profile in Figure 4.10 agree also with the observations of Martínez Pillet et al. (1997) on the fact that δa is larger than δA. The application of a proper spectral and spatial degradation to the simulated data is likely to produce smaller absolute values of the asymmetries, producing a better agreement between the observed and simulated δA and δa.

The first three rays (from left to right in Figures 4.7 and 4.8) and from top to bottom in Figure 4.11, have positive area and amplitude asymmetries. The gradients of V_{LOS} and

Figure 4.11: From left to right: Magnetic field strength along individual rays, line-of-sight velocity along individual rays, (-1) times the τ-derivative of B_{LOS} times the τ-derivative of V_{LOS}, Stokes-I, Stokes-V an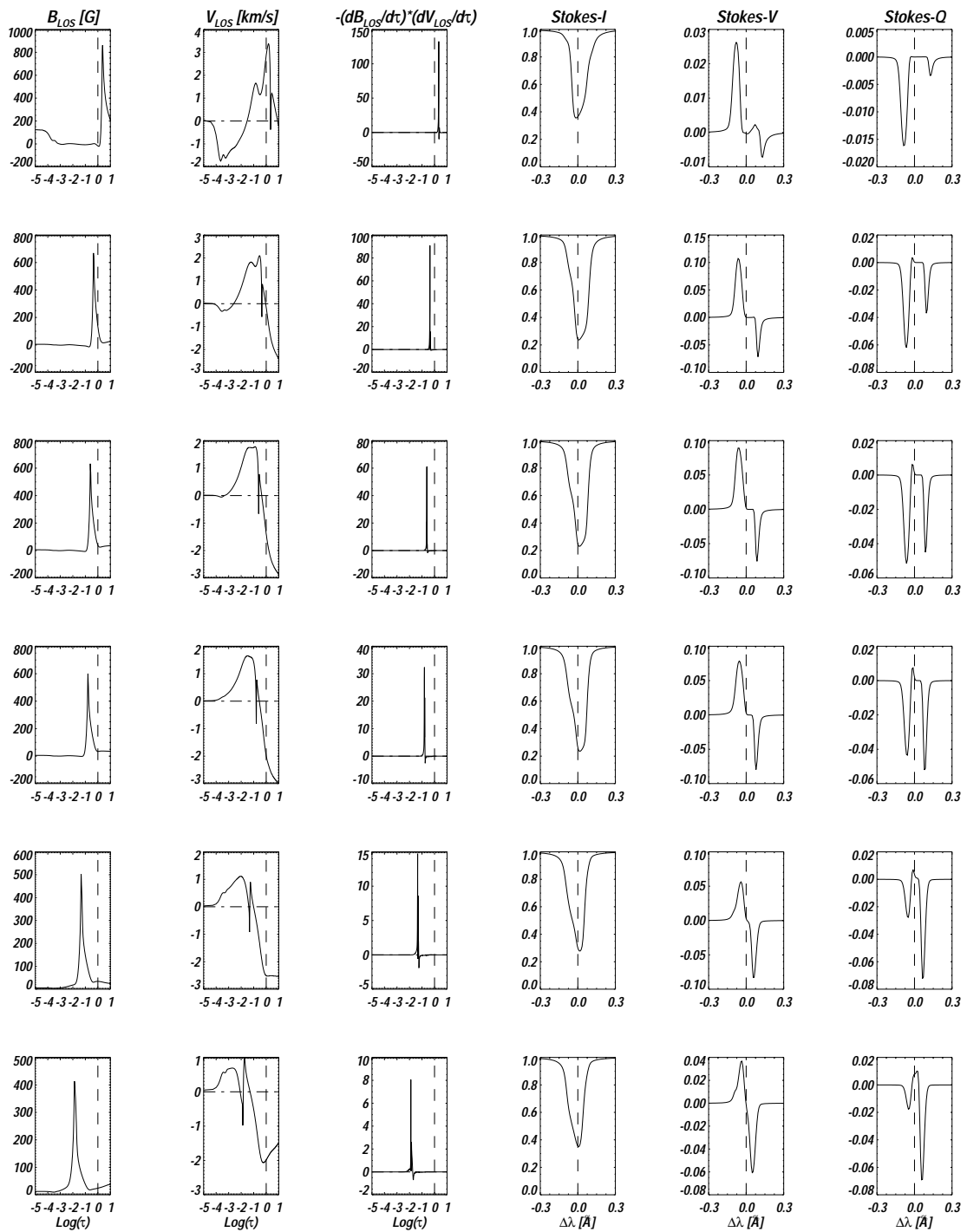d Stokes-Q. Positive velocity correspond to red shift, and negative velocity is for blue shift. The locations of these six rays are indicated in Figure 4.7 and Figure 4.8

B_{LOS} have opposite signs. This is in agrement with Solanki and Pahlke (1988). At ray 4 the Stokes-V amplitude asymmetry is 0, whereas the area asymmetry is still positive. Between ray 4 and 5, δA is positive or 0, and δa is negative or 0. The multiplied gradients of V_{LOS} and B_{LOS} have a small contribution from the opposite sign. It is important to note that in the case where there are two opposite signs of the gradients of V_{LOS} and B_{LOS}, it is not the sign of the dominant amplitude that determines the sign of δA. The latter depends on the fraction of the line being formed at each side of the flux tube (with opposite sign of the gradients of V_{LOS} and B_{LOS}). E.g. for the 5th ray, the region of formation of the Stokes signal (roughly $\log \tau \in [-1, -3]$) includes both signs of the gradients (see middle panel in Figure 4.11). Thus at ray 5 the Stokes-I signal is formed partly in the field-free plasma at the limb side of the flux tube where the plasma is moving towards the observer. This translates to a blue-shift of Stokes-I near the continuum. Higher in the atmosphere, the plasma is moving away from the observer, which produces a red-shift of Stokes-I near the line center. These two opposite-sign contributions will create opposite-sign gradients of V_{LOS} and B_{LOS} at the two magnetic/non-magnetic interfaces at each side of the flux tube (middle panel in Figure 4.11). This will generate opposite sign asymmetries, and in the case of ray 5, they cancel producing $\delta A = 0$.

The 6th ray has negative δA and δa. The Stokes signal is predominantly formed in the flux tube and its neighbouring limb side plasma. In this side of the tube, the plasma is moving towards the observer producing then a blue shift of Stokes-I for most of the line (apart of its central part). This predominance of the line-formation in the limb side of the flux tube gives a higher weight to the sign of the gradients of V_{LOS} and B_{LOS} in this side of the tube. Thus the final sign of Stokes-V asymmetry is coming from the sign of the gradients of V_{LOS} and B_{LOS} in this side of the flux tube. This is in agreement with Solanki and Pahlke (1988).

It is noticeable that the Stokes-V outcoming from rays 2, 3 and 4 have a flat core, and the Stokes-V outcoming from rays 1 harbour a sign reversal at the righthand side of the line core. In order to study the origin of these line core phenomena, we implement the following numerical experiment. We compute 4 sets of Stokes parameters using the following setups: 1) We consider the same atmospheric and line synthesis conditions as in Figure 4.11. 2) We consider the same atmospheric conditions as in Figure 4.11, but we do not consider magnetooptical effects in the line synthesis. 3) We consider similar atmospheric conditions as in Figure 4.11, but we assign a homogeneous magnetic field along the rays (the field strength is equal to the maximum field strength along the rays in Figure 4.11). Magnetooptical effects are considered too. 4) Similar setup to "3)" but without magnetooptical effects. The resulting Stokes-V profiles along the 6 rays for the 4 sets are shown in Figure 4.12. The comparison of set 1 and set 2 indicates that magnetooptical effects are not responsible of the flat cores observed in the Figure 4.11. The Stokes-V core flattening is removed when we put magnetic field through the rays (Set 3). This means (in the case of set 1) and Figure 4.11) that the central part of the spectral line is subject to absorption outside the magnetic regions inducing a flattening of the central part of the polarized Stokes parameters and particularly of Stokes-V (Solanki and Pahlke 1988). The magnetooptical effects (in set 3) produce a sign reversal in the central part of Stokes-V. This in not present in set 4. A temperature enhancement inside the flux tube is responsible of the sign reversal of the central part of Stokes-V in the first ray (Figure 4.11 and set 1 in Figure 4.12). This is similar to the mechanism describe in Solanki and Pahlke
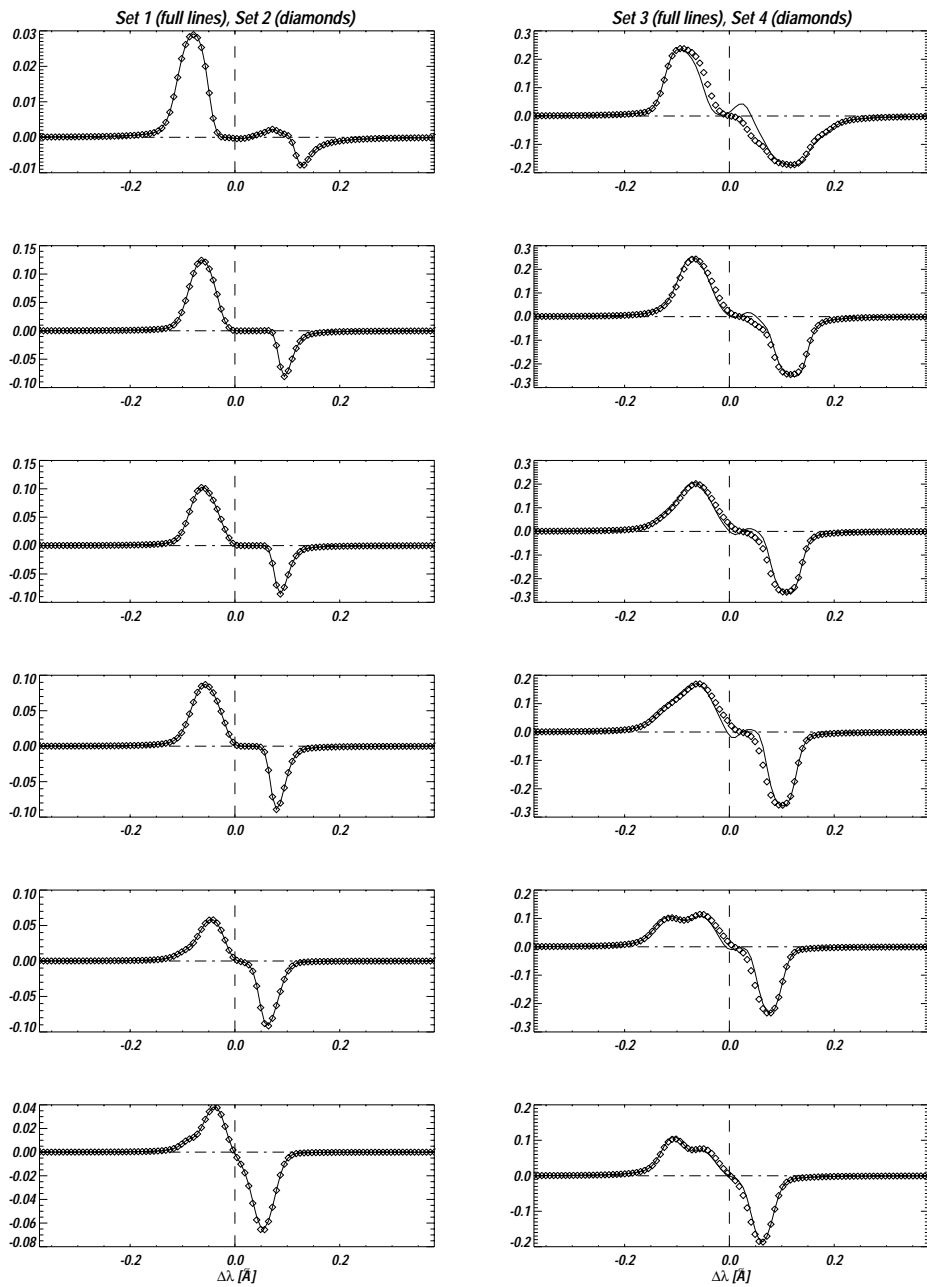
Figure 4.12: Stokes-*V* profiles computed along 6 rays. Set 1 : the atmospheric and line synthesis parameters are similar to the ones in Figure 4.11. Set 2: the atmospheric parameters are similar to the ones in Figure 4.11, but the line synthesis is done with neglecting magnetooptical effects. Set 3 : The rays are filled with a constant magnetic field (equal to the maximum |B| along the rays), but the rest of physical parameters are the same as the previous rays. Magnetooptical effects are considered in the line synthesis. Set 4: Same as set 3 with no magentooptical effects.

(1988) where it is shown that a hotter flux tube than the surrounding produces a sign reversal at the core of Stokes-V. The enhancement of temperature in ray 1 (set 1) occurs at the highest part of the magnetic region where there is a larger redshift than in the rest along the ray, which produces an emission only at the red wing of Stokes-V.

4.4   Comparison with spectropolarimetric observations at $\mu = 0.39$

We will proceed to a comparison between the emerging Stokes signal from the simulation run (presented earlier) and a set of high spatial resolution spectropolarimetric images obtained with the SOUP instrument at the Swedish 1-m Solar Telescope. The observations have been carried out by L. Rouppe van der Voort and M. van Noort in the beginning of 2006. The observational data consist of 9 images: the four Stokes polarization images at both + and −50 mÅ from the line center of the Fe I 6302.5 Å line, and a wide band image. The images are restored using the Multi-Object Multi-Frame Blind Deconvolution (MOMFBD) image restoration method (van Noort et al. 2005). The SOUP images are based on 480 exposures at each line position so that the effective exposure time amounts to 7.2 s. The combined use of the SST adaptive optics system and MOMFBD post-processing resulted in a spatial resolution in the Stokes observations that approaches the diffraction limit of the telescope (close to 0.2 arcsec).

In order to compare these observations with MHD simulations, we have to apply the appropriate degradation to the simulations in order to bring them to comparable conditions with observations. To do so, we carry out the following steps: 1) We choose a quiet-sun simulation run and convolve the synthetic Stokes profiles in the spectral dimension with a Lyot-type filter of FWHM = 70 mÅ (similar to SOUP). 2) In order to account for the lower spatial resolution in the observations, we apply a low-pass filter to the synthetic images which has the shape of a top-hat function and effectively removes power at the highest spatial frequencies - beyond the spatial resolution of the observations. In addition, we convolve the synthetic images with a Lorentzian profile which accounts for the far wings of the PSF that are not corrected for in the MOMFBD restoration. 3) We select a quiet region from the observed Stokes-I images either at + 50 mÅ or −50 mÅ and compare it with the synthetic ones. The matching of the two data sets is done by comparing their power spectra (Figure 4.13 upper panel) and their standard deviations. This is done through an iterative process where both the FWHM of the PSF and Lorenz profile are allowed to change until the two data-sets agree with each other (in the sense of the above two parameters).

The two middle panels of Figure 4.13 indicate the observed (right one) and degraded-simulated (left one) Stokes-I maps at −50 mÅ from line center (Fe I 6302.5 Å). The simulated map corresponds to a quiet region where the mean field strength is about 20 G at τ=1. The power spectra corresponding to the Stokes-I images at −50 mÅ are shown in the upper panel (the full line corresponds to the observed image and the dashed line is for the simulated one). One notices the good agreement between the power spectra of the two data. The standard deviations of the observed and simulated images in the middle panels are 7.63 percent and 7.64 percent, respectively. The observed (right panel) and degraded-simulated (left panel) Stokes-I images at +50 mÅ from the center of the line
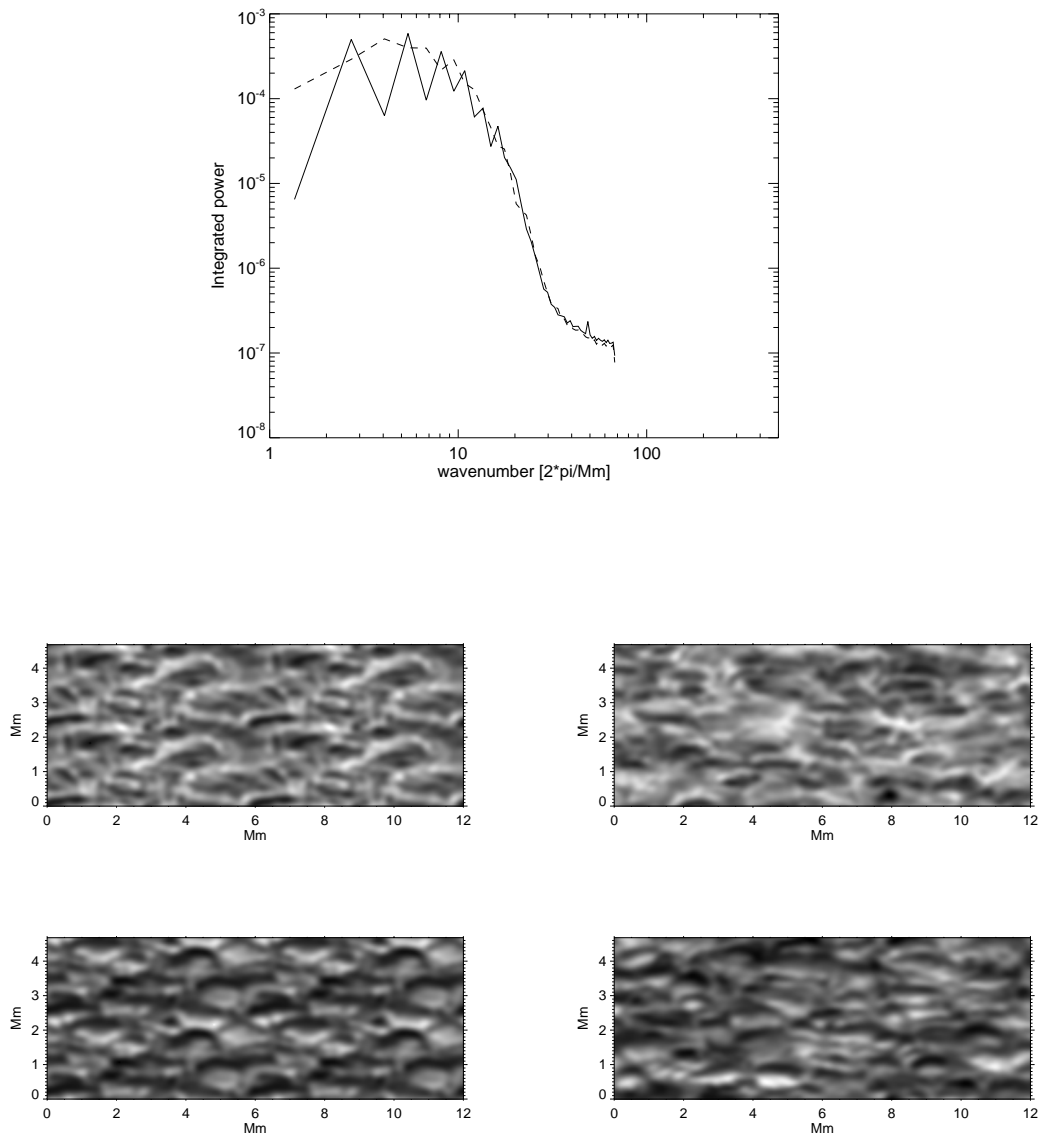
Figure 4.13: Upper panel: integrated power spectra for the two middle images (full line: observations, dashed line: simulations). Middle left panel: simulated Stokes-*I* maps at −50 mÅ from line center Fe I 6302.5 Å. Middle right panel: observed Stokes-*I* maps at −50 mÅ from line center Fe I 6302.5 Å. Lower left panel: simulated Stokes-*I* maps at +50 mÅ from line center Fe I 6302.5 Å. Lower right panel: observed Stokes-*I* maps at +50 mÅ from line center Fe I 6302.5 Å.

are displayed in the lowest panels. Their power spectra are close to the ones in the upper panel, therefore we don't display them here. The standard deviations of the observed and simulated images at +50 mÅ are 11.6 and 11.4 percent, respectively. The corresponding function (in the real space) to a top-hat function (in the Fourier space) is a sine cardinal function. The fit between the observed and simulated images has been achieved for a sine cardinal function with FWHM ≃ 2.5 arcsec.

The so obtained degrading parameters (providing the best agreement between the ob-

served and simulated quiet sun images) are applied to degrade simulations of more active regions, like the ones in Figure 4.14.

The upper image in Figure 4.14 displays an observed Stokes-V image at -50 mÅ from the center of the line Fe I 6302.5 Å. The three vertical white lines indicate the positions where the signal is plotted in Figure 4.15 (left panels). The lower image in Figure 4.14 is a degraded simulated Stokes-V map at -50 mÅ. The MHD simulation run used to obtain this image is the same as in the previous section. The mean unsigned magnetic field strength is about 200 G at $\tau=1$. The vertical white slits indicate the locations where the signal is plotted in Figure 4.15 (right panels). The simulations (lower panel of Figure 4.14) harbour a more homogeneous distribution of the flux than observations. This is due to their periodic boundary conditions, such that the flux that leaves the box from one lateral side, enters again from the opposite side. The observed region presented in Figure 4.14 contains more sparse magnetic features surrounded by a quiet area. This makes the morphology of these magnetic features less confined by surrounding activity. Thus the distribution of flux and its expansion with altitude might not be fully reproduced by simulations. In that sense, a global statistical comparison between the observed and simulated Stokes signals may not be adequate. A comparison between the Stokes-V signals in the two images in Figure 4.14 can be done by plotting the signal along slits (e.g. the white slits). The resulting signal is shown in Figure 4.15.

The upper left panel in Figure 4.15 indicates the Stokes signal across "averagely strong" flux concentrations in Figure 4.14. The signal along this first curve is close to the average "typical" strength associated with flux concentrations in Figure 4.14. In this case the maximum signal is $\in$ [0.06 - 0.08]. The second half of the middle left panel is associated with a relatively weak flux concentration where the signal has a maximum of 0.025. The lower left panel shows the signal across a strong flux concentration. In this case the signal reaches a maximum value close to 0.095. The simulated signal displayed in the upper right and middle right panels indicate that typical simulated flux concentrations have a maximum signal near 0.05. This signal is smaller than the observed one. The lower right panel indicates that the maximum signal in a relatively strong simulated flux concentration reaches about 0.065. If we use simulations with higher field strength (e.g. 400 G), the obtained signal is higher than the observed one (Yelles Chaouche et al. 2008). This indicates that the observed Stokes signal is reasonably reproduced by an MHD simulation run with an average field strength between 200 and 400 G.
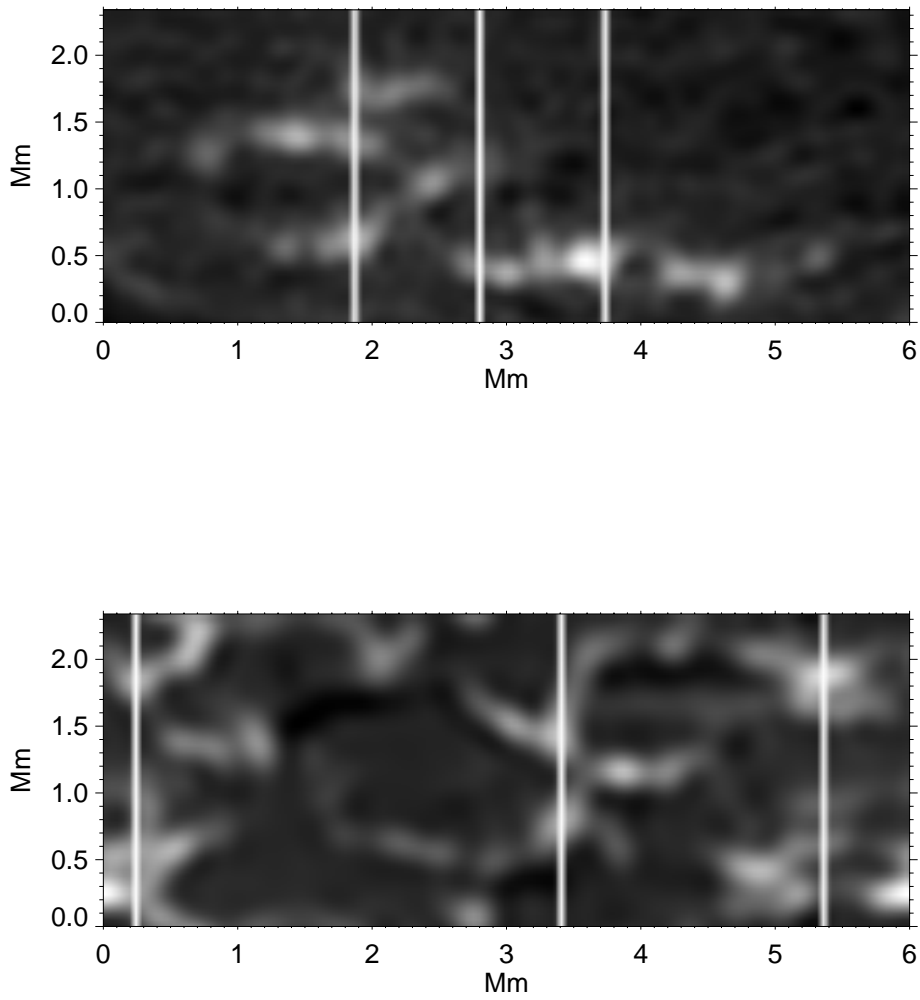
Figure 4.14: Upper panel: observed Stokes-*V* at −50 mÅ from line center FeI 6302.5 Å. Lower panel: Stokes-*V* from simulations degraded to the resolution of observations. White slits indicate the positions where we plot the Stokes-*V* signal in Figure 4.15.
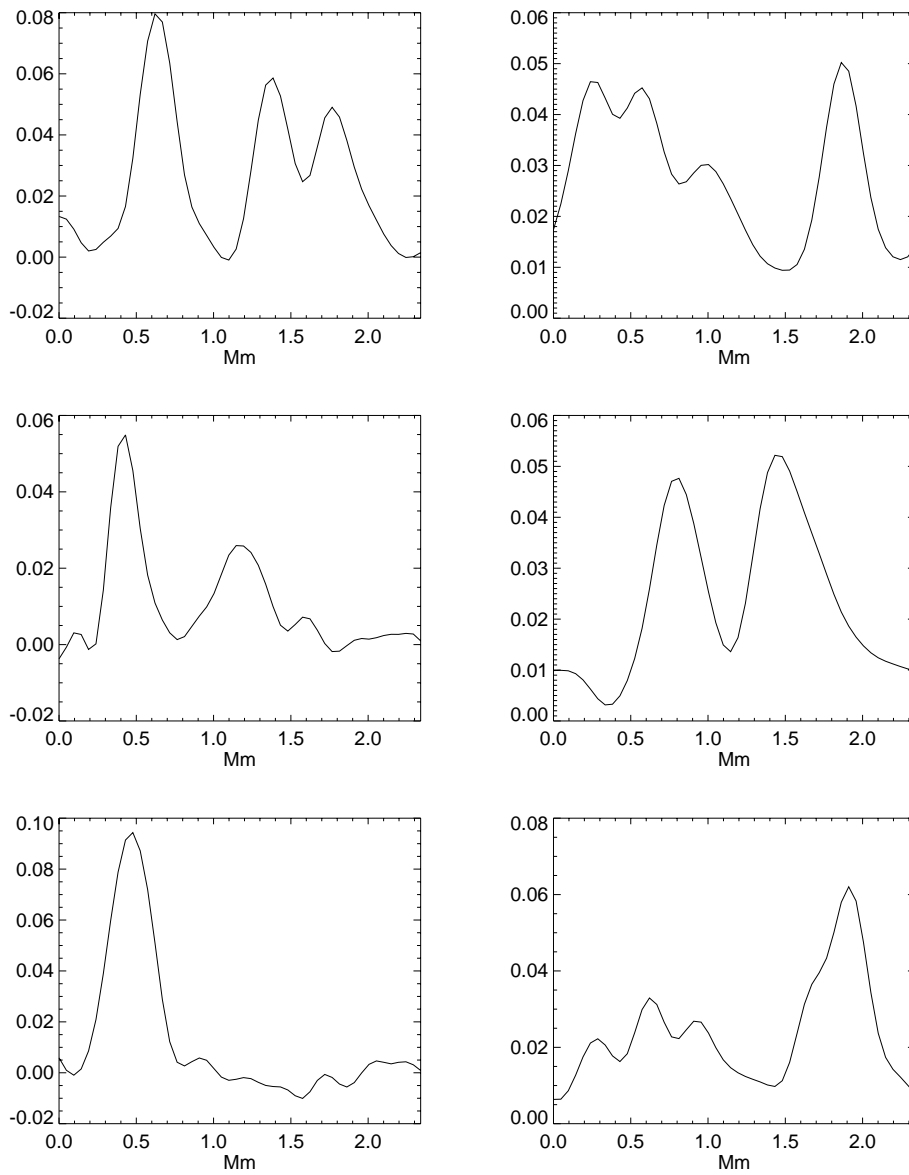
Figure 4.15: Stokes-*V* at -50 mÅ from line center FeI 6302.5 Å at the positions indicated by the white silts in Figure 4.14. Left panels (from top to bottom) correspond to the observed signal (from left to right in the upper panel of Figure 4.14). Right panels (from top to bottom) correspond to the simulated signal (from left to right in the lower panel of Figure 4.14)

4.5   Summary and conclusion

We studied some spectropolarimetric properties of magnetic elements at $\mu = 1$ (disc center) and $\mu = 0.39$ (near the limb). At disc center, the asymmetries produced are mainly positive. Their distribution across the magnetic element is close to the one observed by HINODE's SOT (Rezaei et al. 2007). Near the limb at $\mu = 0.39$, the asymmetries vary from positive to negative values when measured from the center-side of the flux element towards the limb. The mechanisms leading to such asymmetries have been discussed in sections 5.2 and 5.3. At both μ-values, we have seen that the sign of δA follows the law proposed by Illing et al. (1975) and Solanki and Pahlke (1988). The values of the asymmetries (δA and δa) for an averaged Stokes-V profile (averaged over a large enough sample of Stokes-V profiles) indicate that δa is typically larger than δA. This is in agreement with observations (e.g. Martínez Pillet et al. 1997). We believe that an appropriate spectral and spatial degradation of the synthetic spectra (to mimic observation conditions) will allow a better agreement between the simulated and observed values of δA and δa.

We have made a comparative study between high-resolution observations and simulations of spectropolarimetric signals at $\mu = 0.39$. The comparison has been made possible by introducing suitable instrumental and seeing degradation to the simulated Stokes signal. The observed spectropolarimetric signal is reproduced by simulations with a mean field strength situated between 200 G and 400 G. A more complete comparison could be done if we would use observations with higher spectral sampling. In this case, the τ-distribution of physical quantities (such as temperature, magnetic field vector, line-of-sight velocity) would be better studied since it has a direct impact on the properties of the Stokes parameters.

5 Flux emergence at the solar photosphere

5.1 Introduction

Studies of magnetic flux emergence in the photosphere with the help of Stokes parameters started with the work of (Brants 1985a,b, Zwaan et al. 1985). Later it was shown that active regions are formed by successive emergence of flux patches containing only a small fraction of the total flux of the active region (Strous et al. 1996, Strous and Zwaan 1999). These active regions exist in a hierarchy varying from "Large active regions" to "Ephemeral active regions". The largest ones have a total flux up to 4 x 10^{22} Mx (Zwaan 1987). After initial work restricted to spectropolarimetric observations of Stokes-I, Stokes-V and continuum images (Brants 1985a,b, Strous 1994), the full Stokes vector has been used (Lites et al. 1998, Kubo et al. 2003). In the chromosphere there have been also several studies using the full Stokes vector (Solanki et al. 2003, Lagg et al. 2004, 2007). Recently, observational studies of flux emergence with high spectral and spatial resolution has been recorded with Hinode's Spectropolarimeter (Okamoto et al. 2008, Ishikawa et al. 2008 and Cheung et al. 2008). The emerging flux regions are consist of horizontally oriented flux elements, which are the tops of emerging loops. The reported field strength of these horizontal flux elements varies between observational studies : 500 ± 300 G (Brants 1985a,b); 200 < $|B|$ < 600 G (Lites et al. 1998, Sigwarth 2000); 400 < $|B|$ < 700 G (Kubo et al. 2003); 650 G (Okamoto et al. 2008). The rising flux elements have an upward velocity of ≤ 1 km/s. The various estimates of this velocity are : 0.5 km/s (Brants 1985a,b, Strous et al. 1996); ∼ 1 km/s (Lites et al. 1998); < 1 km/s (Kubo et al. 2003); 0.3 km/s (Okamoto et al. 2008).

It has been observed that the granulation pattern in emerging flux regions exhibits an abnormal elongated darkening along parts of granules located at the emerging flux region. This has been observed in the continuum and in the core of the Zeeman-insensitive line Fe I 557.6 nm (Strous 1994, Strous et al. 1996, Strous and Zwaan 1999). These transient darkening alignments last about 10 minutes.

It has been shown by Lites (2005) and Okamoto et al. (2008) that flux elements emerging in the photosphere exhibit a twisted field structure. These emerging twisted flux ropes may contribute to the magnetic helicity of chromospheric prominences.

In recent years there has been a growing body of work aiming to model magnetic flux emergence from the convection zone to the solar atmosphere (e.g. Fan et al. 2003, Fan 2004, Shibata et al. 1989). Most of the modelling effort has been oriented to study emergence in the chromosphere and the corona. These simulations have typically ignored the

effect of convection as well as radiative energy transport in the underlying layer. A more focussed work on emergence of flux from the sub-surface layers to the photosphere has been carried out by Cheung et al. (2007). This has been done using a 3D radiation MHD simulation using the MURaM code (Vögler and Schüssler 2003, Vögler et al. 2005). It takes into account non-local and non-gray radiative energy transport, and includes effects of partial ionization.

In the present work, we study the spectropolarimetric properties of such MHD simulated flux emergence. This provides a bridge between the properties of the observed emerging flux regions and the 3D radiative MHD simulations. We concentrate here on analysing the emergence of a long twisted flux tube (Cheung et al. 2007) and give a detailed comparison (between observations and 3D simulations) of different aspects of the flux emergence.

A description of the MHD simulation setup is given in section 5.2. This is followed by a study of the continuum and circularly polarized Stokes signal characterizing the flux emerging region. The properties of a buoyantly rising flux tube are analysed in section 5.3. We study also the associated spectropolarimetric signature of this emerging flux tube. Some of the most complete spectropolarimetric observation work has been done by Lites et al. (1998) and Kubo et al. (2003). We present a comparison with these observations in section 5.4. We also include in this section some comparisons and discussions with the recent observations of Okamoto et al. (2008) obtained using Hinode's SP. A general discussion and concluding remarks are presented in section 5.5.

5.2 3D simulations and some of their observational properties

The simulation of an emerging flux tube (Cheung et al. 2007) was carried out using a compressible 3D radiation MHD code MURaM (Vögler et al. 2005), which solves the MHD equations taking into account energy exchange via radiative transfer as well as the effect of partial ionization in the equation of state.

The horizontal size of the simulation domain is 24×12 Mm, spanned by 480 and 240 grid points, respectively. The height of the domain is 2.3 Mm, which is spanned by 144 grid points. The resulting grid spacing in the horizontal and vertical directions is 50 and 16 km respectively. The vertical side boundaries are periodic. Both the bottom and top boundaries are open and allow mass transfer. The top boundary is at about 500 km above the base of the photosphere, $\tau_{500} = 1$, where τ_{500} is the continuum optical depth at 500 nm. The magnetic field above the upper boundary is matched to a potential field. At the lower boundary of the simulation domain, the magnetic filed is constrained to be vertically oriented (Cheung et al. 2007)

At $t = 0$, a horizontal, axisymmetric flux tube was introduced, with its axis at 1.35 Mm below the visible surface. The initial longitudinal and transverse components of the magnetic field are given by:

$$B_l(r) \quad = \quad B_0 \exp\left(-r^2/R_0^2\right), \tag{5.1}$$

$$B_\theta(r) \quad = \quad \frac{\lambda r}{R_0} B_l, \tag{5.2}$$

for $r \in [0, 2R_0]$, where r is the radial distance from the tube axis. $R_0 = 200$ km is the characteristic radius of the tube and $B_0 = 8500$ G is the magnetic field strength at the tube axis. The parameter $\lambda = 0.5$ specifies the amount of twist in the tube. The plasma-β (ratio between gas and magnetic pressures, both taken inside the tube) is approximately equal to 1 at the center of the tube. The initial longitudinal flux of the tube is $\Phi_0 = 10^{19}$ Mx. The flux tube has uniform specific entropy equal to the average value of the surrounding upflows.

The setup described above allows the flux tube to rise to the solar surface and remain partly coherent (as a bulk) until reaching the solar surface where the granulation dynamics redistributes the field (Cheung et al. 2007). In order for a flux tube to rise in the subsurface convective layers, its buoyancy force must overcome the downward-directed drag of the convective downflows. The interaction of flux tubes with convection has also been studied by Fan et al. (2003), who performed anelastic simulations of flux tube rise in convective surroundings. The twisted structure of the flux tube maintains its coherence against convective flows, since the tension forces due to the transverse field counteract the pressure forces which try to pull the flux tube apart. Cheung et al. (2007) and Murray and Hood (2008) have investigated the effects of different twist profiles on the properties of a rising flux tube in the subsurface layers of the sun. The latter authors found that, regardless of the specific twist profile, tubes with stronger tension forces have a faster growth rate of the magnetic buoyancy instability, while tubes with weaker tension forces expand to a greater degree in the horizontal direction.

In order to study the observational properties of this flux emergence simulations, we calculate the Stokes signal for Fe I 6302Å and the continuum intensity in the vicinity of the line. This is done in LTE using the STOPRO code in the SPINOR package (Solanki 1987, Frutiger et al. 2000). The continuum images from six snapshots covering the flux emergence sequence are presented in Figure 5.1. The images are degraded to Hinode's SP resolution employing an optical model of the telescope and taking into account a defocus value typical of the Hinode's SP following Danilovic et al. (2008). A Stokes-V time-sequence at -60 mÅ from the line center is shown in Figure 5.2. The images have been obtained after degrading the Stokes signal to spatial and spectral conditions similar to Hinode's SP for Fe I 6302 Å. The spectral degradation is done by convolving the Stokes profiles with a spectral filter approximated by a Gaussian with FWHM = 25 mÅ. A time sequence of maps showing the magnetic field strength at $\tau_{5000} = 1$ is presented in Figure 5.3.

The upper left panel of Figure 5.1 at $t = 7.7$ min, shows the intensity at an early stage of the emergence. At this time, parts of the flux tube are just beginning to transverse the visible surface of the sun (see upper left panel in Figure 5.3). The flux tube reaches heights slightly above $\tau = 1$. This produces a relatively weak polarized signal (see Figure 5.2 for Stokes-V at -60 mÅ from the center of Fe I 6302 Å). We note an enhancement in the continuum intensity at locations where the magnetic field strength is the highest. This is because the plasma temperature inside the rising flux tube is higher than the average granular temperature. This enhancement of the continuum intensity is persistent for several minutes at the early phases of flux rope emergence (see snapshot at $t = 9.7$ min and $t = 11.3$ min). The rise of the flux tube occurs mainly inside granules and influences the local morphology of the granules. At $t = 9.7$ min and $t = 11.3$ min the flux rope emergence has produced typically larger and more elongated granules than the average.
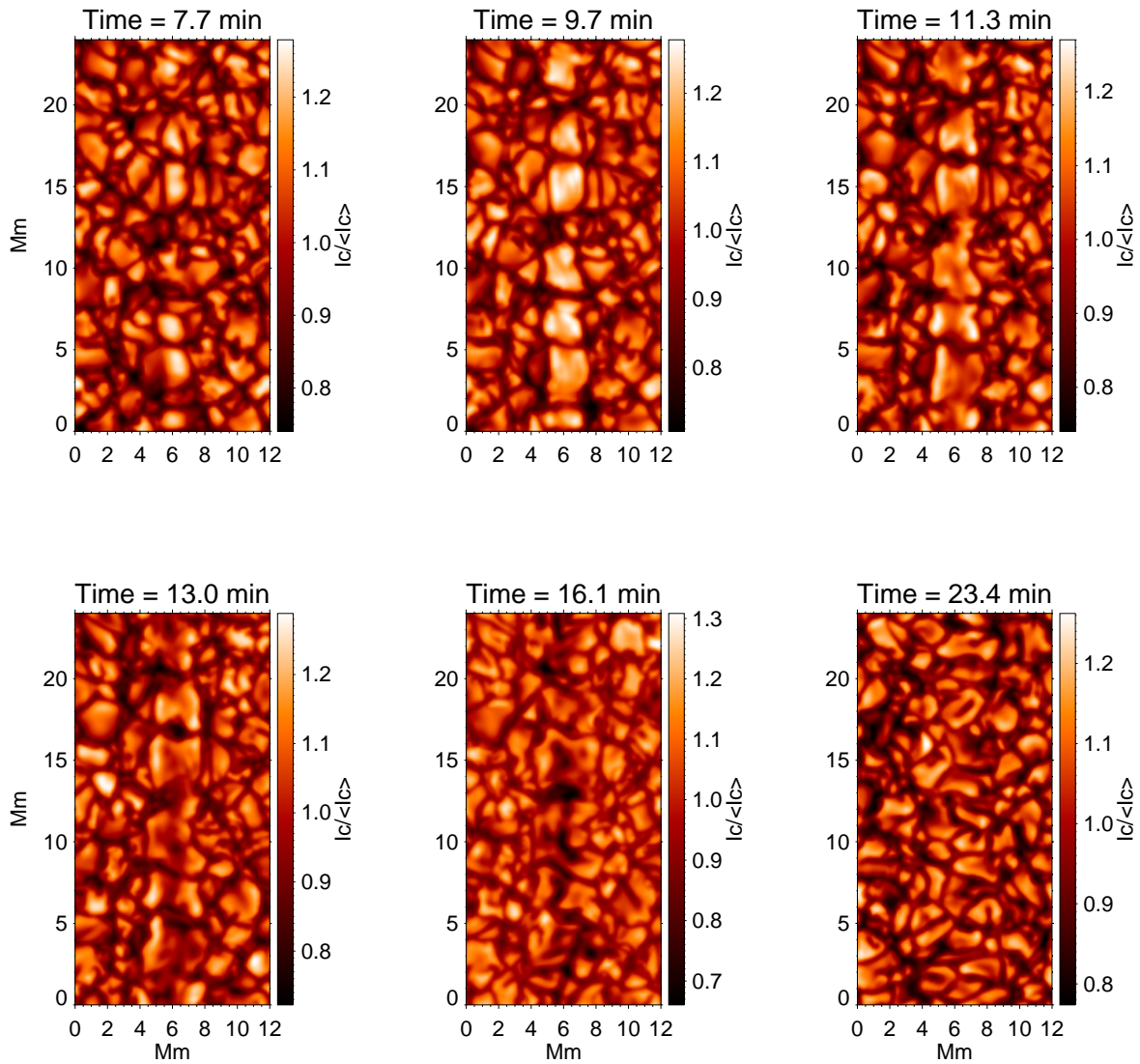
Figure 5.1: Time sequence of normalized continuum intensity maps near 5000Å covering the flux tube's emergence at the solar surface. The time is counted starting from the introduction of the flux tube at -1.35 Mm below the visible solar surface. The images are degraded to Hinode's SP resolution
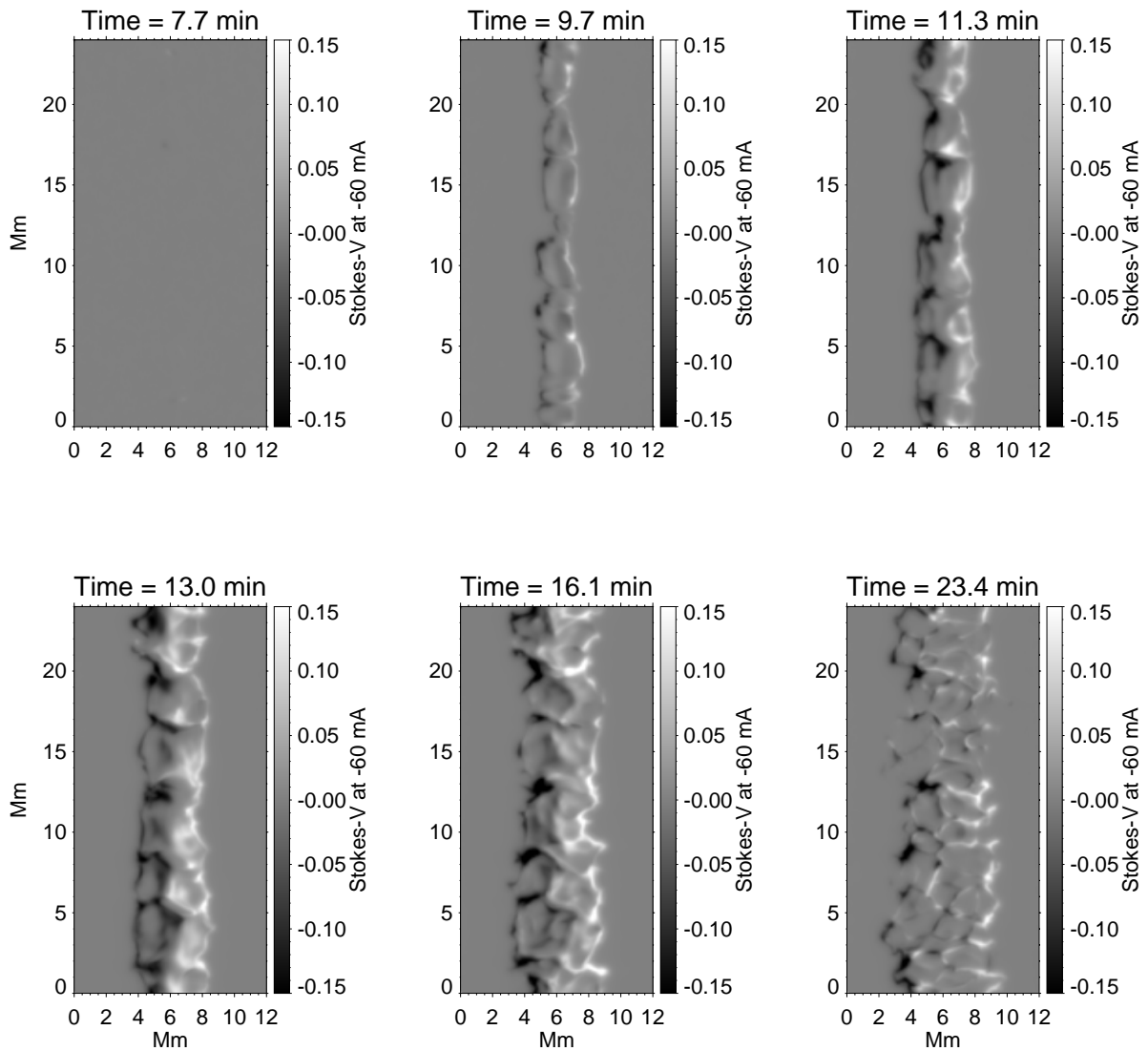
Figure 5.2: Time sequence of maps showing the Stokes-*V* signal at -60 *m*Å from the line center of Fe I 6302.5 Å. The signal is clipped to ±0.15 I_c, with I_c being the local continuum intensity. The images are degraded to spatial and spectral conditions similar to Hinode's SP near 6302.5 Å. Individual snapshots refer to the same times as those of Figure 5.1.

At the lateral sides of the flux tube, downflow lanes are formed. In continuum intensity and Stokes-V maps (Figures 5.1 and 5.2), the emerging flux rope appears as an aligned structure. The enhancement of continuum intensity within the magnetized granules is largest at $t = 9.7$ min. The Stokes-V maps at $t = 9.7$ min and $t = 11.3$ min indicate that the field has different polarities in the right and left parts of the field of view. This is due to the strongly twisted field in the tube. The polarized signal covers an increasingly larger area with time. At later times ($t = 13.0$ and 16.1 min), the continuum intensity maps show the occurrence of a substantial darkening in some locations at the central part of the flux tube. This is particularly clear at $t = 16.1$ min. These dark regions are associated with an upflow in contrast to intergranular lanes which are associated with downflows. These transient darkenings have been reported in observational investigations (Brants and Steenbeek 1985, Strous and Zwaan 1999), and more recently supported by observations using Hinode's SP (Cheung et al. 2008). The darkening occurs both in the continuum intensity and in the core of Zeeman-insensitive lines. This is due to the lower temperature at the locations of these dark regions. This drop in temperature is due to the radiative cooling of the flux tube. Thus initially the rising flux tube is hotter than the neighbouring granules above $\tau = 1$. This flux tube cools down radiatively and looses gradually its buoyancy in the stable photospheric stratification. The twisted structure of the flux tube prevents the convectively driven external plasma from crossing the field lined and heating the central part of the flux tube. This makes the central part of the flux tube cooler than the rest, so that it appears darker. This situation is different from small scale vertically oriented flux tube in which the central part appears brighter. In a vertically oriented small scale flux tube, the flux density above the solar surface is typically larger than that of the horizontally oriented emerging flux tube. This results (for vertical flux tubes) in a significant pressure and density decrease in the magnetic regions. This will result in a Wilson depression reaching few hundred kilometers below the average solar surface. That mean photons emitted in deeper (hotter) layers are observed. Thus the central parts appear brighter. In the present emerging flux tube at $t = 13.0$ and 16.1 min, the magnetic field above the solar surface is relatively weak comparing to vertical flux tubes. This does not produce a sufficiently large pressure decrease to shift the optical depth scale to remarkably lower altitude. Furthermore, the plasma in the emerging flux tube is partly confined in magnetic regions. Thus the radiatively cooled plasma is prevented from flowing down freely, which would have caused depressions and thus the shift of the optical depth unity surface to lower altitude.

At a later stage ($t = 23.4$ min) one does not see any longer the central darkening of the flux tube. The granules covering the flux tube area appear elongated and are preferentially oriented perpendicularly to the tube's main axes. That is because the horizontal outflows driven by the expanding tube causes the granular plasma to preferentially follow this outflow motion.

At $t = 16.0$ and 23.4 min, the locations of the strongest circularly polarized signal (Figure 5.2) are largely correlated with the strongest magnetic flux density (Figure 5.3). This indicates that the magnetic field is rearranged in a more vertical configuration (especially at $t = 23.4$ min). In this latest snapshot, the magnetic flux is essentially located in intergranular lanes located in the former emergence area. The vertically oriented flux concentrations have a typical kilo-Gauss field strength. This is a result of convective intensification of the magnetic flux (Parker 1978, Spruit 1979, Schüssler 1990, Nordlund
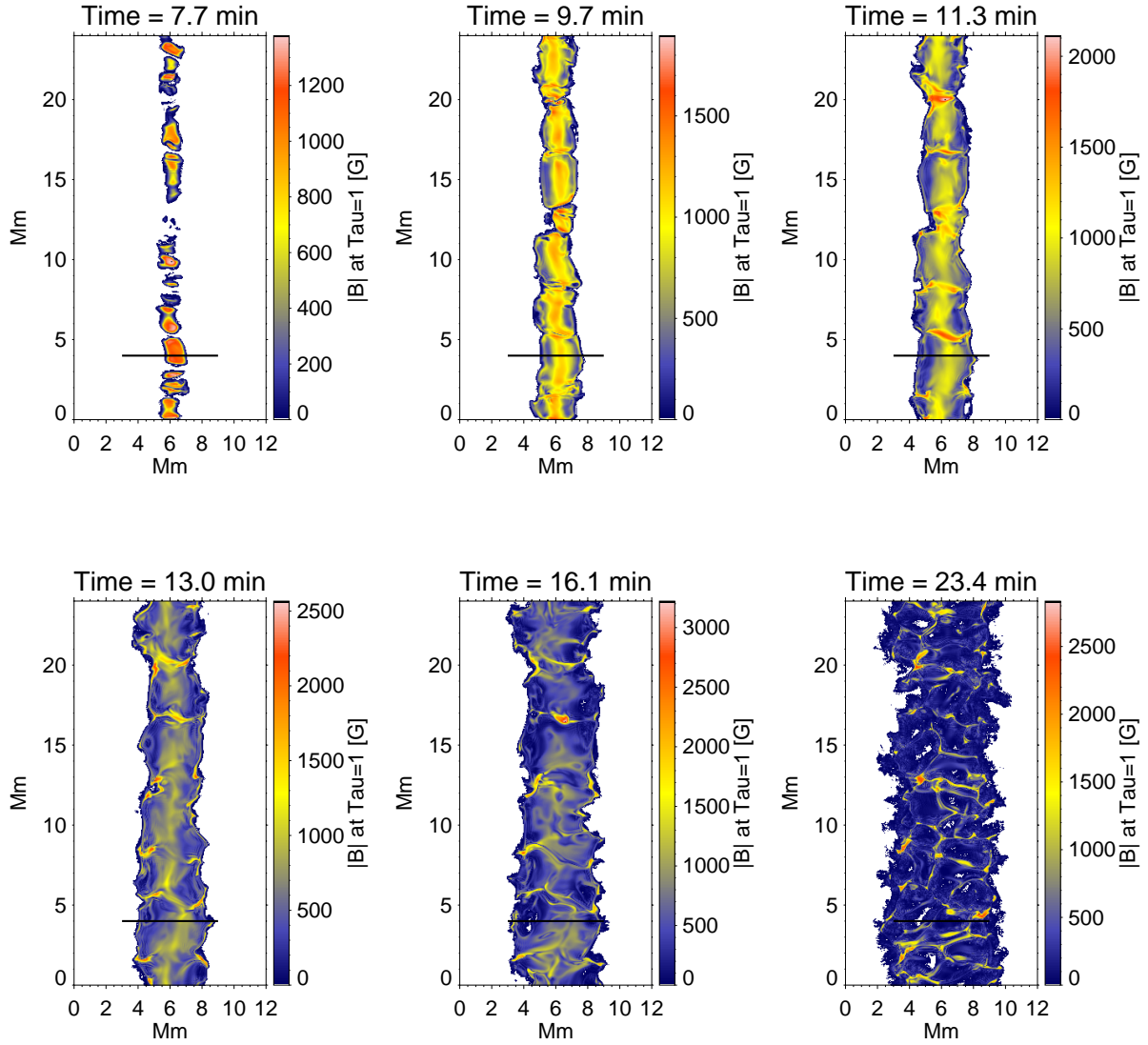
Figure 5.3: Magnetic field strength at $\tau_{5000} = 1$. The maps show the same time sequence as Figures 5.1 and 5.2 . The dark lines indicate the locations where the vertical cuts through the MHD data are presented in Figures 5.4 to 5.9 .

and Stein 1990, Grossmann-Doerth et al. 1998, Vögler et al. 2005, Cheung et al. 2007).

5.3   The buoyant rise of the emerging flux tube

The flux rope begins its rise at -1.35 Mm below the visible solar surface ($\tau = 1$). At the beginning of the rise the time reference is set to $t = 0$ min. The buoyancy force accelerates the flux tube upward.

Figure 5.4 shows a vertical cut through the MHD data at the location shown by the dark line crossing the flux tube in the upper left panel in Figure 5.3 at $t = 7.7$ min. The displayed panels correspond to, from top to bottom, the temperature fluctuations with respect to horizontal average (to better reveal horizontal structures), vertical velocity, magnetic field strength and inclination relative to the vertical. The red and blue colour-codes in the velocity panel stand for redshift and blueshift, respectively. The full lines across the panels show the locations of the optical depth unity ($\tau = 1$). The dashed lines indicate the maximum of the contribution function of Stokes-V. The dash-dotted lines show the location of the maximum of the contribution function of Stokes-I. Since the contribution functions are wavelength dependent, we integrate them over wavelengths, and then define their maximum. The rising flux tube brings hot plasma to the photosphere, so that the magnetized plasma (near $\tau = 1$) is hotter than the surroundings at similar geometrical height. This makes the optical depth unity line geometrically higher inside the flux tube than outside. At this early emergence phase ($t = 7.7$ min), the magnetic flux tube has only a small part above the solar surface, the resulting polarized signal is relatively weak (Figure 5.2) and formed over the magnetized plasma which is mainly located low in the atmosphere (dashed lines in Figure 5.4) near optical depth unity at this early phase of emergence. The twisted configuration of the field lines makes the magnetic field vector largely horizontal in the upper part of the flux tube (inclination in Figure 5.4) and mainly vertical at each side of the tube's cross section as shown in Figure 5.4. This situation produces weak circularly polarized light (Figure 5.2) at $t = 7.7$ min since most of the magnetic field above the solar surface is horizontally oriented. Stokes-I has a relatively regular formation height, with a slight increase above the flux tube. This is due to the overall change in the optical depth above the emerging flux tube, which has caused the optical depth scale to shift towards higher altitudes.

The parts of the flux tube that reach the solar surface start to cool down radiatively, due to the considerable increase of the photon mean free path above the solar surface (Figure 5.5 at $t = 9.7$ min) (Cheung et al. 2007). The radiatively cooled plasma becomes denser and looses its buoyancy. We note though that the flux tube as a whole continues rising even in these non-buoyant layers. This is due to the fact that the rising sub-surface parts of the flux tube keep pushing the plasma above the surface upward. Part of the material above the surface also has a lateral motion as a reaction to the pressure excess caused by the continuously rising plasma into the emergence site. Also, the cooled dense plasma overlying the emergence zone partly descends back to the convection zone at each side of the flux tube. This is followed by a concentration of vertically oriented magnetic field at each side of the flux tube (Figure 5.5). This field is oppositely oriented at each side of the flux tube depending on the dominant field orientation provided by the twisted emerging flux tube (see the orientation of the magnetic field at each side of the flux tube
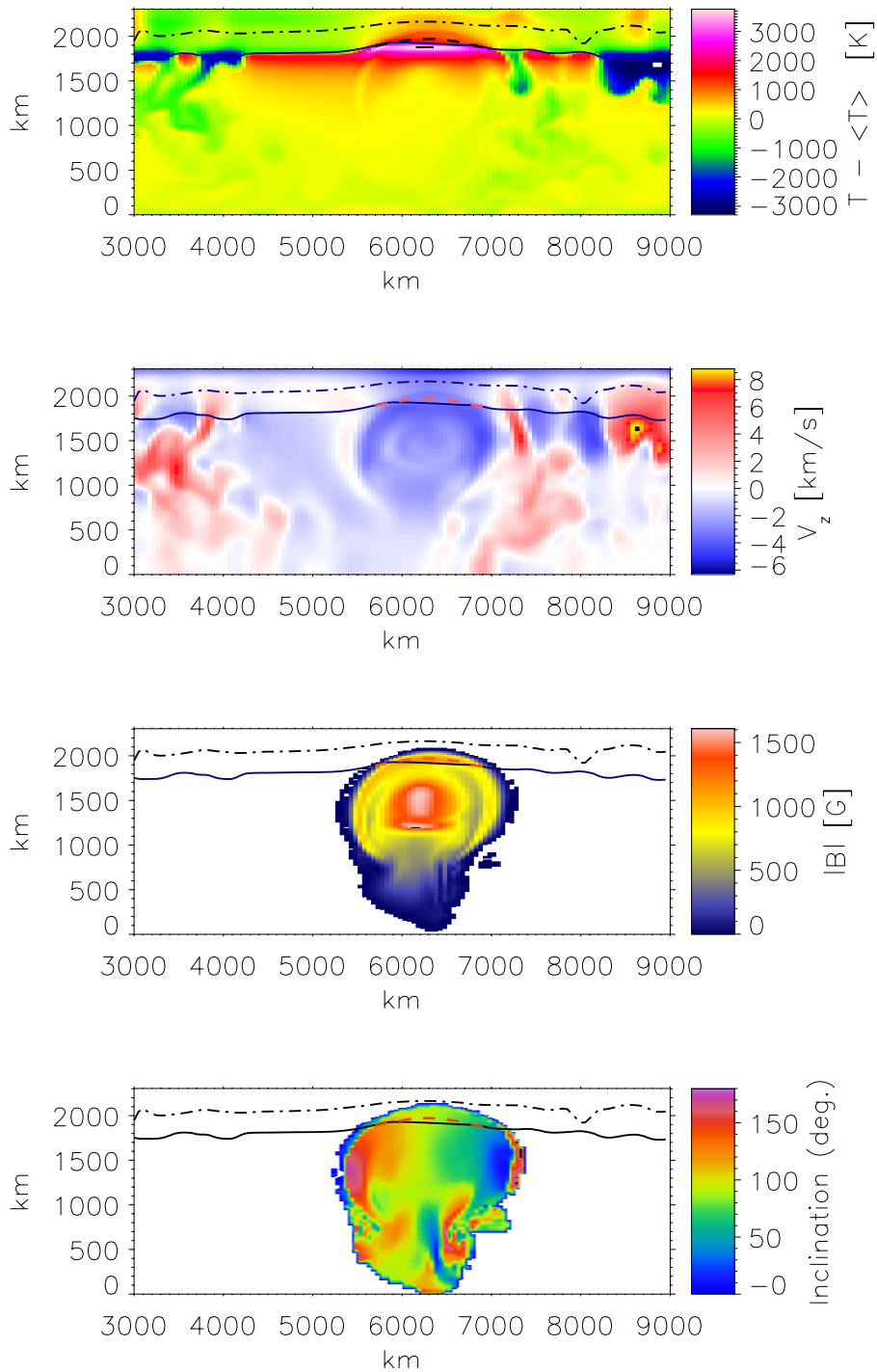
Figure 5.4: Vertical cut through the MHD data at the location shown by the black line in the upper left panel in Figure 5.3 at $t = 7.7$ min. The panels represent, from top to bottom, the temperature fluctuations with respect to horizontal average, line-of-sight velocity (blue represents upflow), magnetic field strength and inclination. The full lines indicate the location of $\tau_{5000} = 1$. The dash-dotted lines show the height at which the contribution function of Stokes-I reaches its maximum, and the dashed lines indicate the same for Stokes-V

Figure 5.5: Same as Figure 5.4 but for the location shown by the black line in Figure 5.3 at t = 9.7 min
.

Figure 5.6: Similar to Figure 5.4 at $t = 11.3$ min

in Figure 5.3). These vertically oriented flux concentrations produce an enhancement of the circularly polarized signal at each side of the flux tube, as shown in Figure 5.2.

At later times $t = 11.3$ and 13.0 min (Figures 5.6 and 5.7), the flux tube is more extended in the lateral dimension than in the verti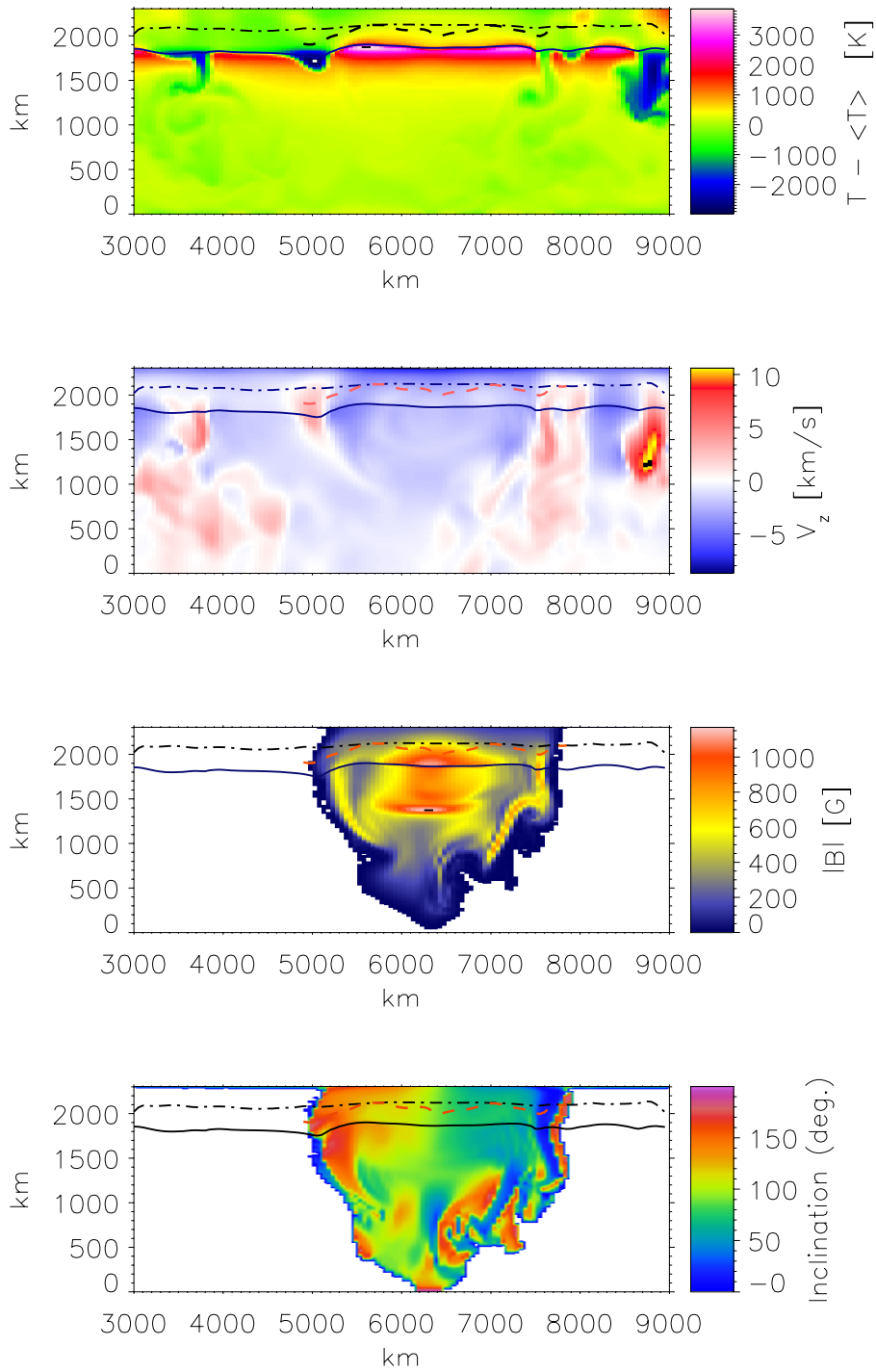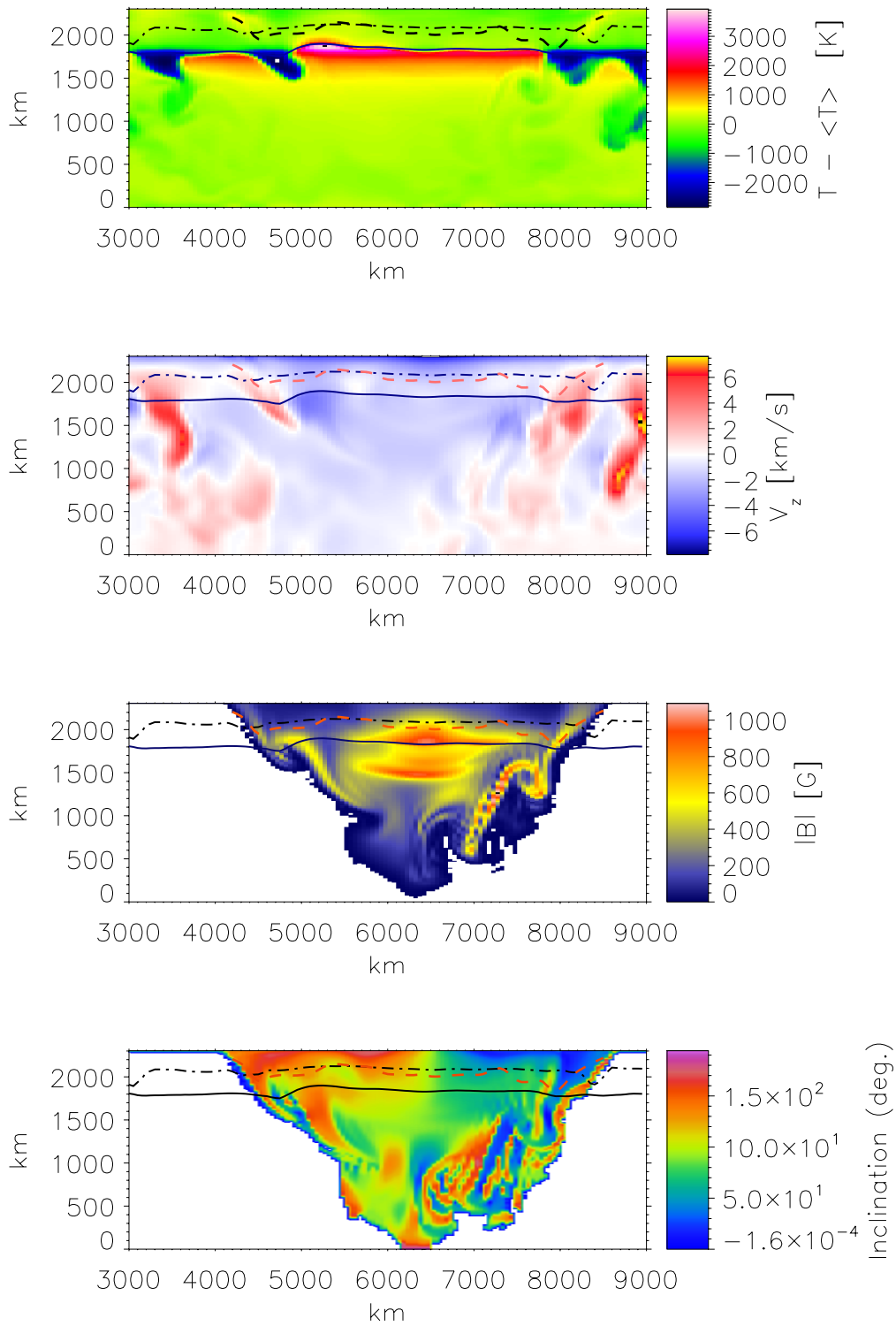cal. The vertically oriented fields concentrated at each side of the flux tube have moved away form each other. The central part of the flux tube has reached the photosphere. The evolution of the emerging flux tube is influenced by the convection dynamics. This is especially the case at the outer parts of the emerging flux tube where the field configuration is more complex than the central part. This latter part is still carrying a relatively regularly twisted core with a field strength approaching 1 kilo Gauss. Note that the polarized signal is formed over a region sampling mainly sub-kilo Gauss field. It has been shown by Fan et al. (2003) and Cheung et al. (2007), that flux tubes with field strength of the order of the equipartition field strength are not passively carried by the convection. In this case the kinetic energy density of the convective flow is of the same order as the magnetic energy density of the flux tube. The twisted morphology of the flux tube ensures more coherence against the convective flows, because the tension forces due to the transverse field counteract the external pressure forces which tend to distort the flux tube (Cheung et al. 2007, Murray and Hood 2008). This makes the morphology of a twisted flux tube with equipartition field strength less sensitive to the surrounding granulation dynamics than similar flux tube with less twist. The granulation pattern is affected by the twisted flux tube. This results in the granulation pattern shown over the emergence sequence in Figures 5.1, 5.2.

At $t = 16.1$ min (Figure 5.8), one can still see the downflows at each side of the flux tube where the flux is predominantly vertical. The flux tube is wider, and one notices the appearance of downflowing plasma above the solar surface in the body of the flux tube (e.g. near the abscissa $x = 2400$km). The horizontally oriented core of the flux tube has greatly shrunk. Most of the flux is located in the vertical downflow lanes. This produces a strong circularly polarized signal correlated with downflow lanes in the emergence area. The core area (around $x = 3900$km), is relatively cooler than the surroundings. This explains the appearance of a darkening at the central part of the flux tube in the continuum images (Figure 5.1).

In Figure 5.9, $t = 23.4$ min, the magnetic flux is mainly distributed as vertically oriented flux concentrations (see also Figures 5.2 and 5.3 for a more general overview). Thus, the magnetic flux initially brought by the emerging flux tube has been rearranged as vertically oriented flux concentrations. These flux elements are located in inter-granular lanes as a result of flux expulsion (Weiss 1966, Galloway and Weiss 1981). The vertically oriented flux elements have a field strength of about 1-2 kG resulting from convective intensification of the magnetic flux. The maximum of the contribution function of Stokes-I is shifted to lower altitudes near the magnetic flux concentrations. Because the partially evacuated flux tube makes the upper layers of the atmosphere more transparent (optically thinner), this shifts the optical depth scale towards lower altitudes.

5.4   Comparison with spectropolarimetric observations

5.4.1   Observation conditions and the Milne-Eddington inversion

Spectropolarimetric observational studies of flux emergence in active regions outside sunspots have been performed by Lites et al. (1998) and Kubo et al. (2003). In order
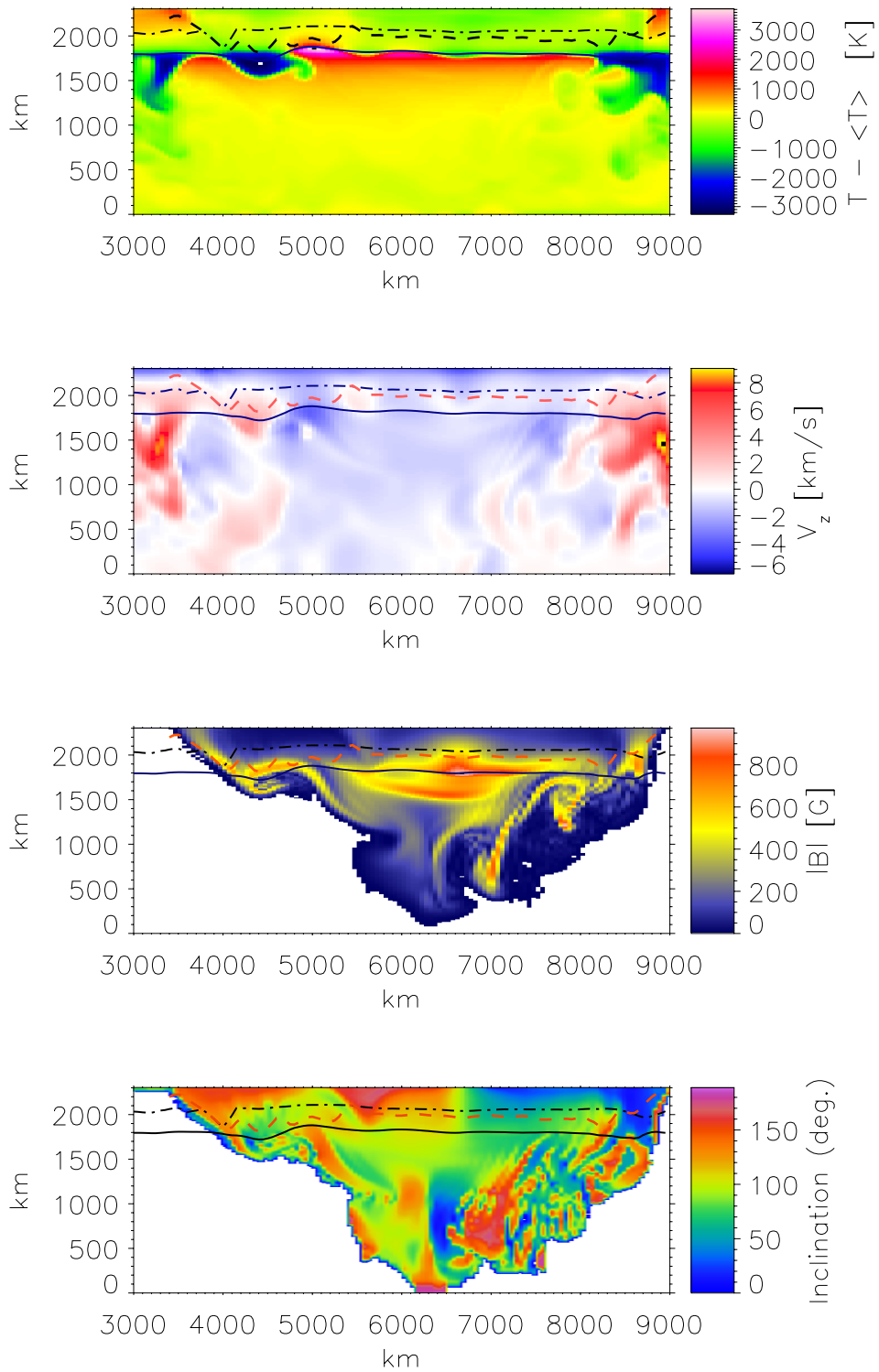
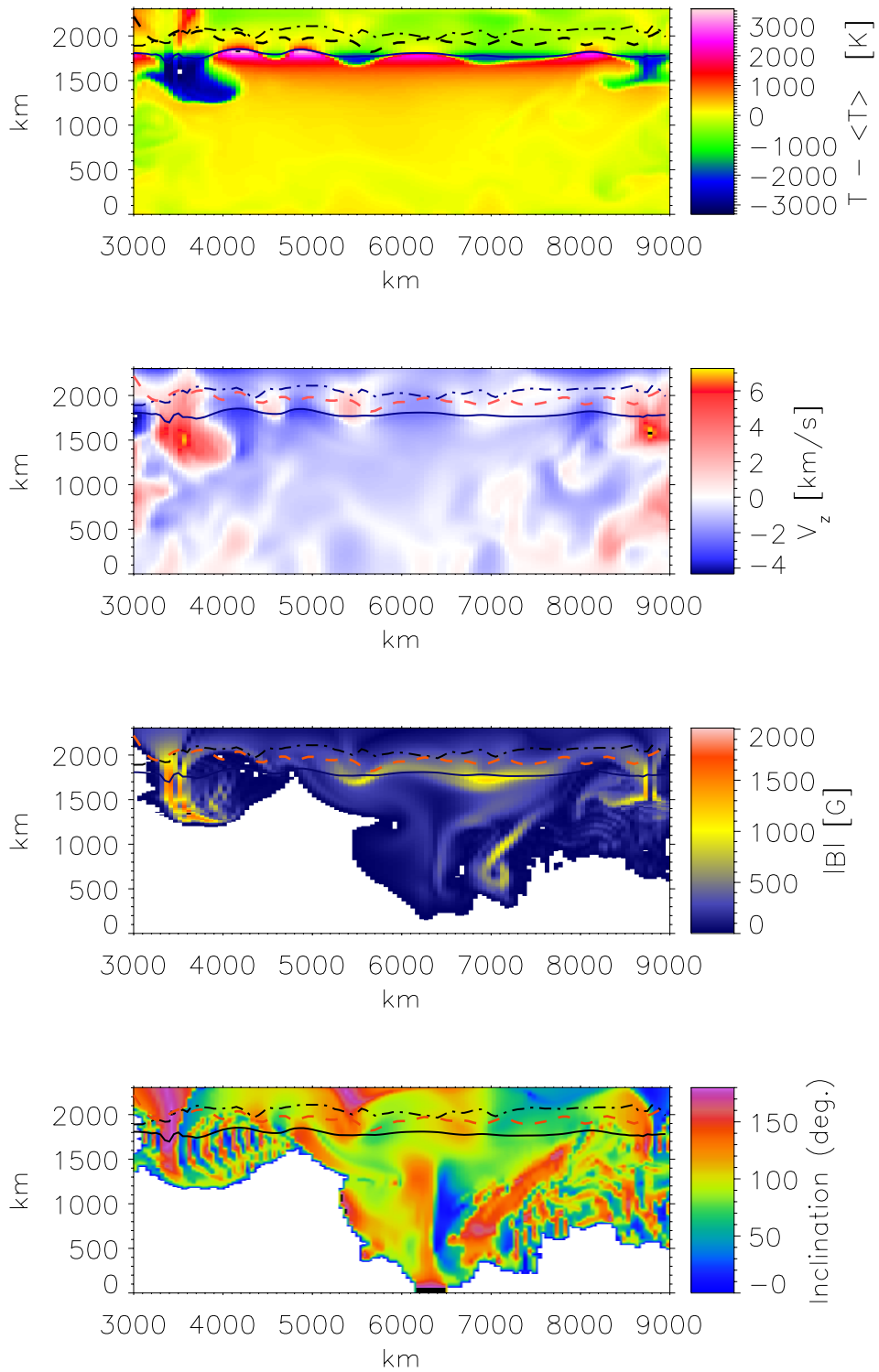Figure 5.7: Similar to Figure 5.4 at t = 13.0 min

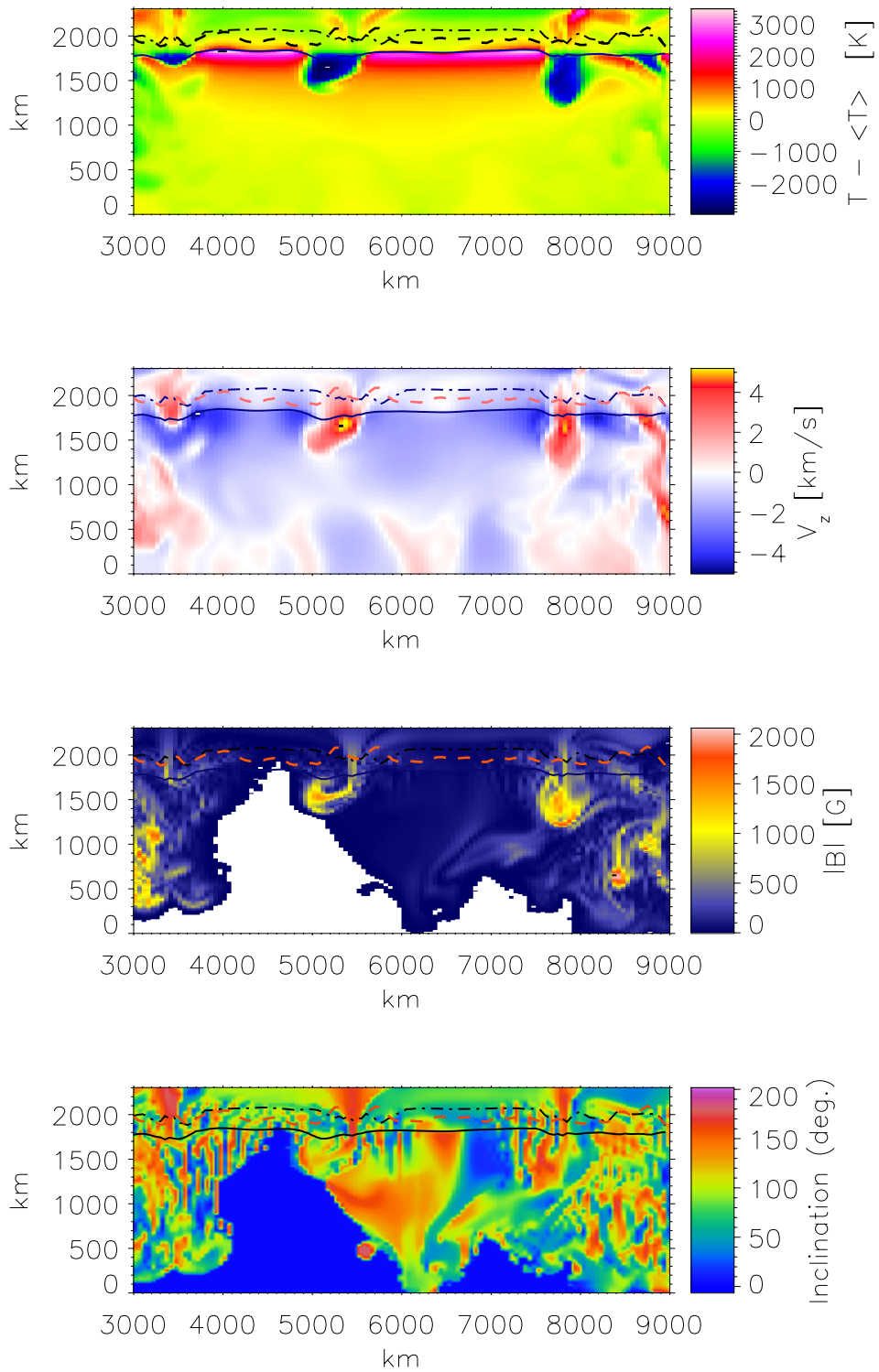Figure 5.8: Similar to Figure 5.4 at t = 16.1 min

Figure 5.9: Similar to Figure 5.4 at $t = 23.4$ min

to compare our results with these observational results, we degrade our synthetic data to approximate the observational conditions and then follow a similar inversion procedure as described in Kubo et al. (2003).

The observations on which these two publications are based have been done with the Advanced Stokes Polarimeter (ASP) at the NSO. The slit spectropolarimeter has observed a flux emergence area in the two iron spectral lines Fe I 6301.5 Å and Fe I 6302.5 Å recorded at a spectral resolution of 25 mÅ. The obtained spatial resolution varies form 1" to 3", depending on the seeing conditions. The pixel size is 0.37". In order to reproduce the observation conditions, we have reduced the spectral resolution and sampling of the synthetic Stokes spectra to match the observed ones. The spectral transmission function was assumed to be a Gaussian with FWHM = 25 mÅ. The spatial smearing of the synthetic data is done by convolving with a Gaussian with FWHM= 750km to account for the limited spatial resolution of the telescope. We also include a convolution with a Lorentzian profile with FWHM = 5500km to account for degradations due to the scattered light. To account for the photon noise we add a normally distributed noise with a standard deviations of 10^{-3}. This will be divided by the square-root of Stokes-I to account for the amount of light at each spectral position.

The observed spectra were inverted using a Milne-Eddington code (Skumanich and Lites 1987, Lites and Skumanich 1990). This is based on fitting the observed Stokes profiles with synthetic ones obtained from an analytic solution of the Unno-Rachkovsky equations (Unno 1956, Rachkowsky 1967) in a Milne-Eddington atmosphere (see e.g. Landi degl'Innocenti 1992). We invert the spectra using the Milne-Eddington code **He-LIx** (Lagg et al. 2004). This code allows to find the minimum of the merit function using either a Levenberg-Marquardt algorithm or a genetical one. We have tested the Levenberg-Marquardt algorithm using synthetic Stokes spectra and compared the results with the response function averaged physical parameters from the MHD data (e.g. $|B|$, line-of-sight velocity, etc.). It turned out that the physical parameters retrieved with the Levenberg-Marquardt algorithm were in poor agreement with the original MHD data. We have made similar tests with the genetical algorithm. These have revealed good agreement between the response-function averaged physical parameters from the MHD data and the ones retrieved by the genetical algorithm. We choose then in the following to uses the **HeLIx** code with the genetical algorithm mode. The two spectral lines Fe I 6301.5 Å and Fe I 6302.5 Å were inverted simultaneously in the work by Kubo et al. (2003) and in the present work. The existence of two atmospheric components within each pixel was allowed for. One of these harboured a magnetic field, while the other was field-free and represented scattered light as well as the field-free gas in the resolution element. The fraction of the surface area occupied by magnetic field within each pixel is called "filling factor". The inversion procedure looks for the optimal combination of parameters corresponding to the minimum of the merit function. The following free parameters are considered by Lites et al. (1998) and Kubo et al. (2003): the magnetic field strength, its inclination and azimuth, the ratio of line center to continuum opacity of each line, the Doppler width of each line, the damping constant of the two lines, the positions of the wavelength centers of the two lines, the slope and surface value of the source function, the Doppler shift of the scattered light, and the filling factor. In our inversions we consider similar free parameters apart of the positions of the wavelength centers of the two lines, since they are already known in synthetic spectra.

5.4.2   Inversion results and comparison with observations

Figure 5.10 shows a time sequence of the magnetic field maps retrieved from inversion. From top to bottom, $t = 11.3$, 13.0, 16.1 and 23.4 min. The colour coded maps show the amplitude of the vertical component of the magnetic field. The orientation of the horizontal components of the field is indicated by lines (to take into account the 180° ambiguity). At first, we notice that the emerging flux appears more smoothly distributed compared to Figures 5.2 and 5.3. This is due to the low resolution (about 1 arcsec) of these synthetic data. The twisted structure of the emerging flux tube is revealed by the orientations of the field lines. This orientation changes between the two snapshots at $t = 11.3$ min and $t = 16.1$ min. A similar situation has been observed by Okamoto et al. (2008) using Hinode's spectropolarimeter (SP) with the same iron lines as used here. At $t = 11.3$ min the spectral lines are sampling the upper part of the emerging flux tube where the field lines are following a positive-to-negative polarity orientation. Later at $t = 16.1$ min, the flux tube has further emerged and the spectral lines are sampling its lower part where the field lines, in this twisted structure, are oriented from negative to positive polarity. We point out some differences between the discussions and suggestions in Okamoto et al. (2008) and the findings of the present work : In Okamoto et al. (2008), the authors support the idea that the flux rope has emerged from the photosphere to the corona, and mention that the altitude reached by the flux rope might be of the order of the tube's diameter. We have seen in the previous section (and in Cheung et al. 2007) that the flux tube upon emergence is not cylindric but has a rather flattened shape resulting from the flux tube's expansion in the lateral direction. It has been also shown that even though most of the magnetized plasma becomes anti-buoyant after reaching the photosphere, the sub-photospheric parts of the flux tube continue to emerge in the photosphere showing then a blue shift along most of the flux emergence in the region of formation of the iron lines Fe I 6301.5 Å and Fe I 6302.5 Å. The scatter plots in Figure 5.11 (determined from inversions) show the inclination angle versus the magnetic field strength (left panels), and the inclination angle versus the line-of-sight velocity (left panels) along the emergence sequence presented in Figure 5.10 (from top to bottom). This indicates that the horizontally oriented emerging flux has an upflow (blueshift) along most of the emergence sequence. This blueshift should not be interpreted as an upward motion of the flux tube as a nearly homogeneous cylinder (like the work by Okamoto et al. might suggest) but is rather a signature of an upflowing material in the photosphere. Wether the emerging twisted flux tube observed by Okamoto et al. 2008 is a major source of helicity for the overlying filament is not clear according to the findings of the present simulations and inversions (see also Cheung et al. 2007).

In order to compare the results of the present inversions with those of Lites et al. (1998) and Kubo et al. (2003), we also compute histograms representing the distributions of the magnetic field strength, inclination, and line-of-sight velocity along the emergence sequence (Figure 5.12). From top to bottom, the panels cover the four emergence times presented in Figure 5.10. Following the observational analysis of Lites et al. (1998) and Kubo et al. (2003), the histograms in Figure 5.12 and the scatter plots in Figure 5.11 are calculated for pixels where the total degree of polarization integrated over the line profile of Fe I 6302.5 Å is greater than 0.4 percent. This is to ensure considering data points essentially above the noise level.
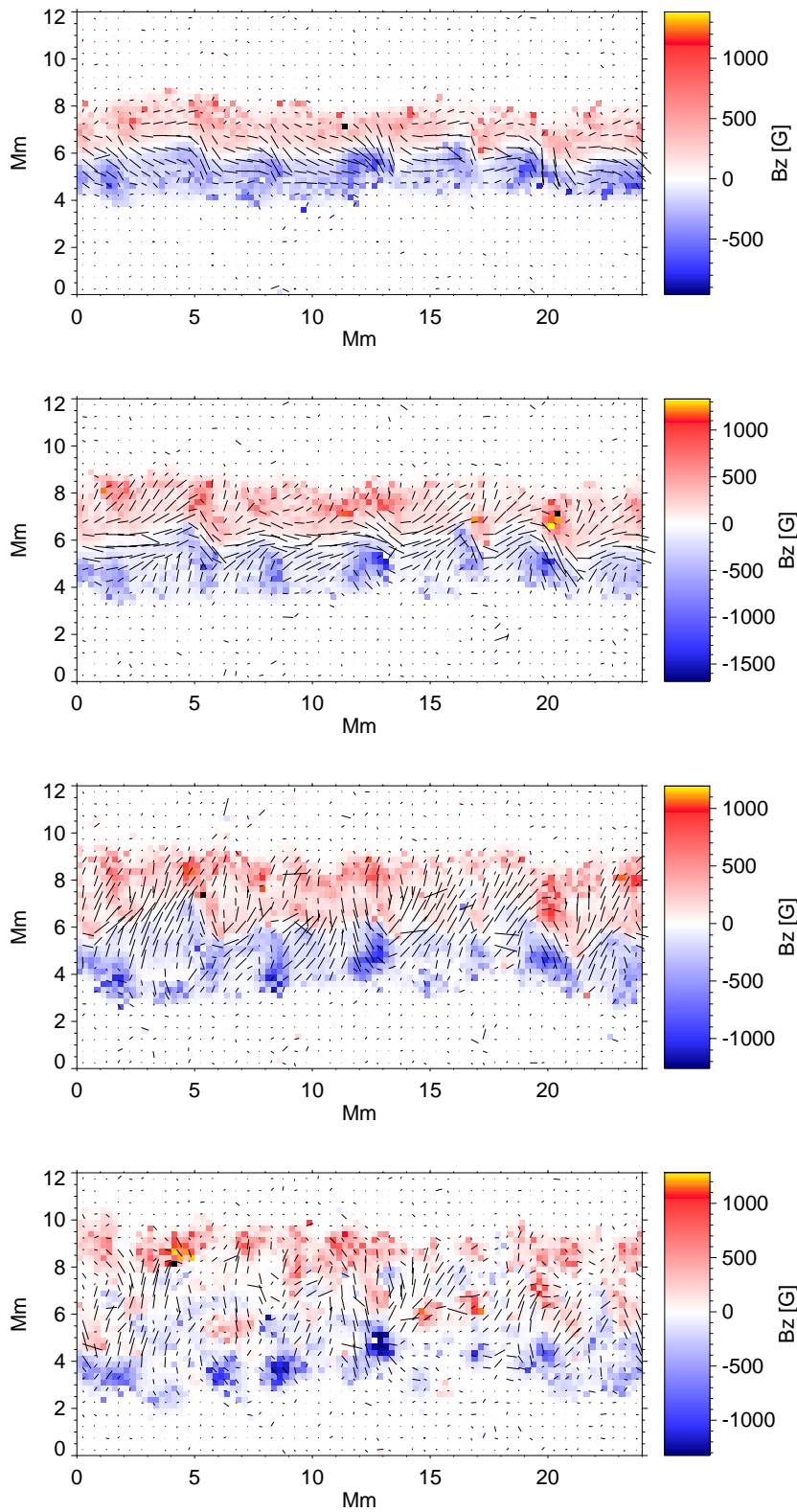
Figure 5.10: Maps of the retrieved magnetic field vector from inversions. The colour code indicates the amplitude of the vertical (line-of-sight) component of the magnetic field. The orientation of the horizontal field components is shown by lines. The maps correspond to (from top to bottom) : $t = 11.3, 13.0, 16.1$ and 23.4 min
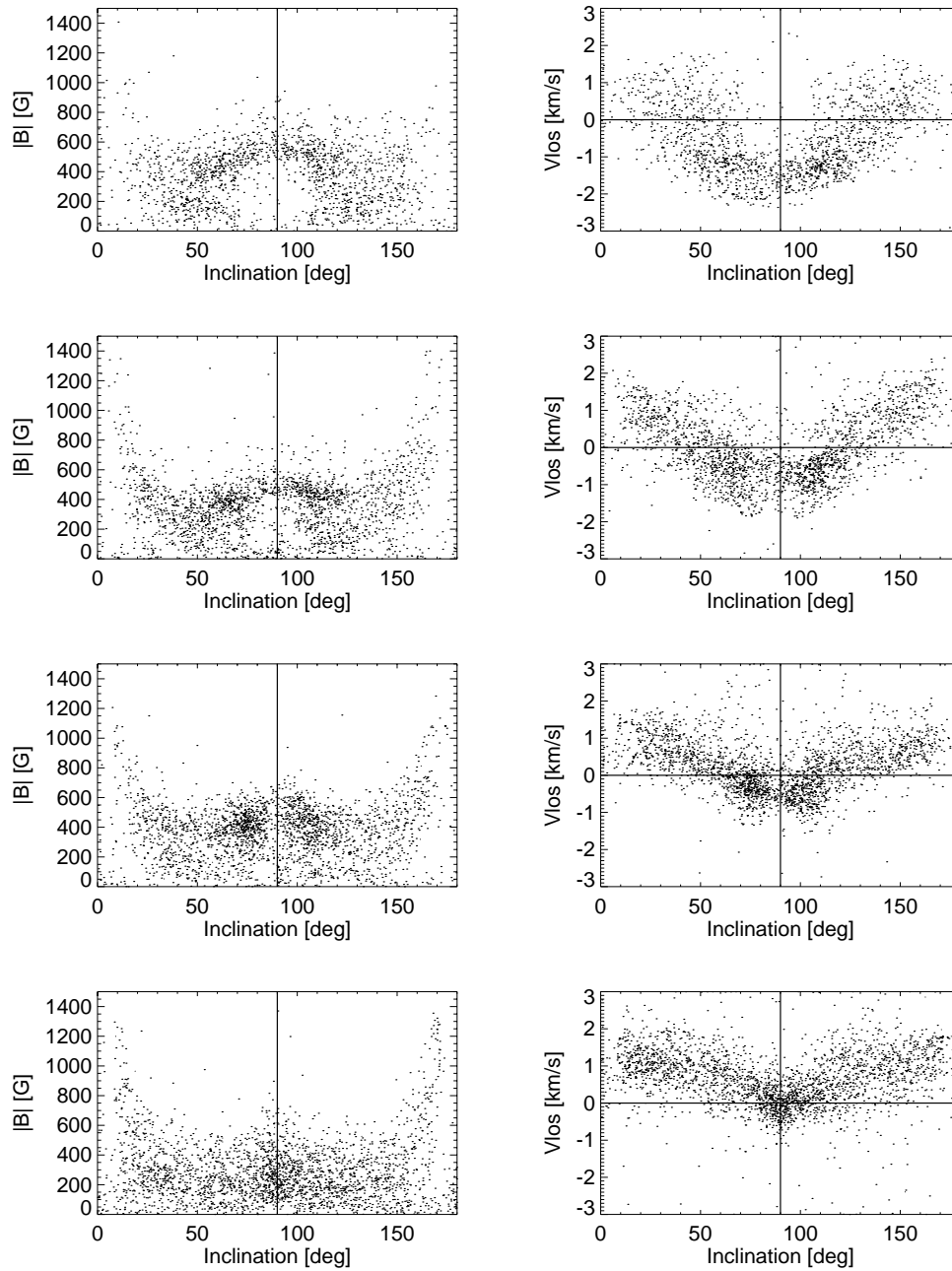
Figure 5.11: Scatter plots of some parameters retrieved from the inversion. Left panels : inclination angle versus the magnetic field strength. Right panels : the inclination angle versus the line-of-sight velocity. From top to bottom, the panels corresond to the same time sequence as in Figure 5.10

The top row of panels in Figure 5.12 corresponding to $t = 11.3$ min indicate that the emerging flux is distributed mainly over field strength between 400 G and 600 G. This field is essentially close to a horizontal distribution (middle panel). More precisely the distribution of the field inclination harbours maxima around 105 degrees, 60 degrees and 90 degrees. The two former values are statistically more significant. This dominantly double maxima distribution of field inclination is due to the twisted configuration of field lines in the emerging flux tube. The uppermost right panel in Figure 5.12 indicates the line-of-sight velocity. It exhibits a maximum around −1.2 km/s (the negative sign stands for upward motion). The scatter plots in the top row of panels of Figure 5.11 indicate that the nearly horizontally emerging flux is associated with upflow motion with values up to −2.3 km/s and a field strength of about 600 G. At $t = 13.0$ min, the distribution of field strength (Figure 5.12) has a maximum situated between 400 and 500 G. The double peak distribution of the inclination is still present. The V_{los} distribution has a maximum in the interval [-0.2, -0.8] km/s. The corresponding scatter plots in Figure 5.11 show that the nearly horizontally oriented field has an upward motion with lower amplitude than in the previous snapshot. Part of the field with nearly vertical distribution (below 20 degree and above 160 degree) has reached kilo-Gauss field strength and exhibits a dowflow motion (second row from the top in Figure 5.11). The scatter plots in Lites et al. (1998) and Kubo et al. (2003) exhibit horizontal field strength between 200 G and 700 G. This is in good agreement with the inversion results at $t = 11.3$ min, $t = 13.0$ min and $t = 16.1$ min. The observed upward motion of the horizontally oriented field is typically < 1 km/s. This is also in agreement with the results of the scatter plots at $t = 13.0$ min and $t = 16.1$ min. The scatter plots at these two emergence times appear to reproduce at best the horizontal field properties as apparent from the scatter plots in Lites et al. (1998) and Kubo et al. (2003). We notice though some differences between the scatter plots obtained from observations and simulations. Namely the vertical field strength reported by observations is larger than the one obtained in simulations. This might be due to the fact that the observed emergence region contains a pre-existing vertical field (since the emergence happened in plage regions). This pre-existing vertical flux is expected to have typical kilo-Gauss values (Vögler et al. 2005). In contrast, the simulated flux emerges in a field free region. Another difference between the observed and simulated scatter plots representing the field inclination versus its strength is that the observed ones have V-like shapes whereas the simulated ones have W-like shapes. This lack of data points at intermediate inclination angles is clearer in the work of Kubo et al. (2003) (see the lowest panels of Figure 8 in their work). While the scatter plots of Lites et al. (1998) (Figure 3 in their work) exhibit some data points with low |B| at intermediate inclination angles (mainly from the neighbouring plage region as indicated in Lites et al. (1998)). The histograms presented in Kubo et al. (2003) (Figures 6 and 7, corresponding to regions B1 and B2 in their work) compare at best with the histograms at $t = 13.0$ min in Figure 5.12. We notice also some differences between the observed and simulated histograms. Namely, the simulated field inclination exhibit a characteristic double peak due to the twisted configuration of the field lines in the emerging flux tube. We notice also some double peak in the region B2 (Figure 7 in Kubo et al. 2003), and a slight double peak for the region B1 with filling factor higher than 80 percent (Figure 6 in Kubo et al. 2003). Nevertheless the separation of the two peaks in the simulated histograms is larger than the observed ones. This indicates that the simulated emerging flux tube has a larger twist than the observed

ones.

At $t = 16.1$ min we notice that the two peaks in the distribution of inclination in Figure 5.12 have become closer to each other. This indicates that the twist of the emerging flux tube has been partly dissipated due the interaction of the flux tube with the convective granulation motion. At $t = 23.4$ min, we observe a single peak in the distribution of the field inclination. This corresponds to field strengths of about 200 G (Figure 5.12). The corresponding scatter plots in Figure 5.11 show that the horizontally oriented field has a slight or zero upward velocity, while the nearly vertically oriented flux is associated with downflows.

5.5   Discussion and concluding remarks

The inversion results presented in the previous section are consistent with many of the observed properties of flux emergence regions (Lites et al. 1998, Sigwarth 2000, Kubo et al. 2003). The inversion results show that at $t = 11.3$ min, $t = 13.0$ min and $t = 16.1$ min, the rising flux tube has a spectropolarimetric signature showing that the horizontally oriented magnetic flux has a typical field strength of 400 to 600 G while the central part of the flux tube reaches kilo-Gauss field strength at the base of the photosphere. Nevertheless the spectral lines are formed over a region where the field strength is dominantly of sub-kilo-Gauss values. We also have seen that the field is mainly horizontal while it emerges into the photosphere. Simulations and observations indicate that the emerging flux reaches the solar surface with a nearly horizontal field of about equipartition field strength or slightly higher. This underlines the importance of the interaction of the rising flux tubes with the granular dynamics. It has been shown in sections 5.2 and 5.3 (also in Cheung et al. 2007) that the rising flux tube has produced elongated granules (as an effect of the flux tube on the granules), and later the granular dynamics has rearranged the emerging flux in small vertically-oriented flux concentrations (as an effect of the granular dynamics on the rising flux tube). The emerging flux is redistributed by flux expulsion to become vertically oriented flux concentrations in intergranular lanes (Weiss 1966, Galloway and Weiss 1981). Their typical field strength reaches kilo-Gauss values as a result of convective intensification (Schüssler 1990, Nordlund and Stein 1990, Grossmann-Doerth et al. 1998, Vögler et al. 2005, Cheung et al. 2007).

There are some differences between the observed and simulated flux emergences. The comparison between the observed and simulated distributions of field inclination indicates that the amount of twist in the simulated flux tube is larger than for the observed ones. We note that, unlike the observations, the simulated flux tube emerges in a field free region with no pre-existing field.

The twisted structure of the flux tube is revealed by the inversions of synthetic spectra along the emergence sequence. Such signature of twisted emerging flux tube has been observed by Okamoto et al. (2008) using Hinode's spectropolarimeter with the same iron lines as used here. We have seen that a blueshift is associated with the emergence event for most of the emergence sequence. This blue shift should not be interpreted as an upward motion of the flux tube as a nearly homogeneous cylinder (like what could be interpreted from the work by Okamoto et al. 2008). It has been shown that the emerging magnetized plasma expands laterally, and is essentially redistributed as vertically oriented flux con-
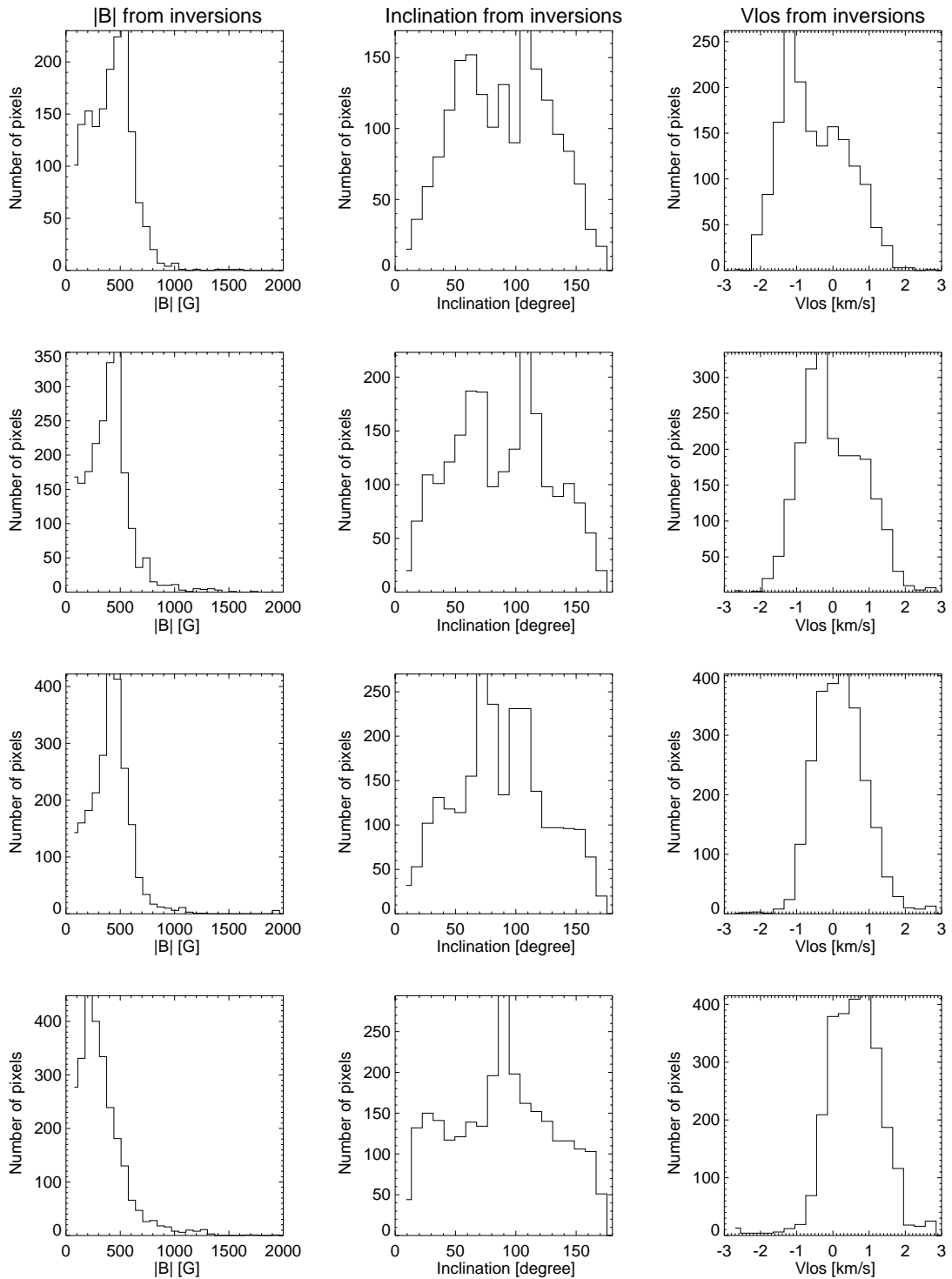
Figure 5.12: Histograms of magnetic field inclination, magnetic field strength |B|, and line-of-sight velocity. From top to bottom, the panels correspond to the same time sequence as Figure 5.10

centrations. The scenario presented by Okamoto et al. (2008) proposing the emergence of twisted flux tubes as a major source of helicity for the overlying filament is not clear according to the findings of the present simulation and inversions (see also Cheung et al. 2007). We propose further observational investigations using simultaneously lines formed at different heights enabling to record the velocity and magnetic field at the photosphere and chromosphere.

Observations report that the flux often emerges in the form of loop-like structures. From a simulation point of view this field configuration can be reproduced by prescribing higher entropy at the middle part of the flux rope at the beginning of the numerical experiment. This will make the central part rise faster than the rest, thus producing an Ω-like shape. One can further assign a lower entropy than average to the two "ends" of the flux tube, making them anti-buoyant and producing thus a more pronounced shape of the Ω-like rising loop. A first analysis of such a simulation run has been carried out by Cheung et al. (2007, 2008) without spectropolarimetric study. We believe that a further spectropolarimetric analysis is needed to study the observational signatures of such flux loops.

6 Outlook

We have seen that at an inclined view, the polarized signal outgoing from small scale magnetic elements is formed over a relatively localized region. This can provide an ideal situation for performing spectroploarimetric diagnostic of these flux elements. The Center-to-Limb Variations (CLV) of Stokes-V profiles and their asymmetries carry valuable information on the properties of small scale magnetic flux elements and their dynamical surrounding plasma (Stenflo et al. 1987, Solanki 1987, Buente et al. 1993, Martínez Pillet et al. 1997), for a review see (Solanki 1993). A natural next step of our work is to investigate the CLV variations of Stokes-V amplitude and area asymmetries. This is already a work in progress. The diagnostic potential of the linearly polarized signal (Stokes-Q and U) has not been fully used in the past. Though this reveals important physical properties of flux concentrations like temperature, magnetic field, and internal flow velocity (Solanki 1987, Stenflo et al. 1987, Martínez Pillet et al. 1997, Solanki et al. 1998, Leka and Steiner 2001). So far, there have been only few attempts to study diagnostics based on the linearly polarized signal in the framework of MHD simulations (e.g. Leka and Steiner 2001). The CLV diagnostics using Stokes-Q (or $\sqrt{Q^2 + U^2}$) asymmetries between the σ and π components carry information about the 3D structure of flux concentrations. This diagnostic is sensitive to the temperature and magnetic field of flux elements (Solanki 1987, Stenflo et al. 1987). More generally we have seen that the polarized Stokes signal is influenced in a complex way by the atmospheric conditions inside and outside flux concentrations since the magnetic flux and plasma mutually influence each other in a magneto-convective system. Thus a promising way for studying magnetic flux elements is to compare the simulated and observed CLV variations of the linearly polarized Stokes profiles. Also, the ratio between the σ components of : on one hand Stokes-V, and on the other hand Stokes-Q (or $\sqrt{Q^2 + U^2}$), provides diagnostics about the internal magnetic, velocity and temperature structure of flux concentrations since they are proportional to the line-of-sight and transverse components of the magnetic field respectively, and thus form at slightly different optical depths near the limb.

The magnetic flux emergence in the photosphere covers a wide range of fluxes (Zwaan 1987, Lites et al. 1998, De Pontieu 2002, Okamoto et al. 2008). This suggests the use of different simulation setups in order to study a given event. Observations also report the emergence of loop-like structures. We are then challenged with new (and also confirmed) hight resolution spectropolarimetric observations in active regions and quiet sun (De Pontieu 2002). Regarding the emergence event studied in chapter 5, we propose to use a simulation run with less twist. This will probably affect the coherence of the rising flux rope but will probably bring a better agreement between simulations and observations. A second important simulation scenario, is to study loop-like rising flux ropes. We already have started the analysis of such structures following the simulations of Cheung et al.

(2007). The use of deeper boxes and higher fluxes is a necessary step too (Cheung et al. 2008). The influence of the upper boundary conditions of these simulation can be studied by implementing different heights of simulation boxes and different upper boundary conditions for the plasma flows and the magnetic field.

The rapidly growing computational resources and the increasing observational resolution, opens perspectives to the study of several solar physics domains. Many stimulating questions can be addressed in the few next years by extending the available realistic 3D MHD simulations to the chromosphere (e.g. Hansteen and Gudiksen 2005). The non-LTE nature of this layer makes it so-far still largely unexplored by MHD simulations. The many questions concerning the second solar spectrum, and the nature of non-LTE processes bring the necessary motivations for such a work.

Bibliography

Bellot Rubio, L. R., Ruiz Cobo, B., Collados, M., 1997, Flux-Tube Model Atmospheres and Stokes V Zero-crossing Wavelengths, Astrophys. J. Lett., 478, L45

Bellot Rubio, L. R., Ruiz Cobo, B., Collados, M., 1999a, Probing downflows in solar magnetic elements: the Fe II test, Astron. Astrophys., 341, L31–L34

Bellot Rubio, L. R., Ruiz Cobo, B., Collados, M., 1999b, An LTE code for the inversion of Stokes spectra from solar magnetic elements, in Polarization, (Eds.) K. N. Nagendra, J. O. Stenflo, vol. 243 of Astrophysics and Space Science Library, pp. 271–280

Bercik, D. J., 2002, A numerical investigation of the interaction between convection and magnetic field in a solar surface layer, Ph.D. thesis, Michigan state university

Borrero, J. M., 2004, The fine structure of the sunspot penumbra, PhD thesis, Universität Göttingen

Brants, J. J., 1985a, High-resolution spectroscopy of active regions. II Line-profile interpretation, applied to an emerging flux region, Solar Phys., 95, 15–36

Brants, J. J., 1985b, High-resolution spectroscopy of active regions. III - Relations between the intensity, velocity, and magnetic structure in an emerging flux region, Sol. Phys., 98, 197–217

Brants, J. J., Steenbeek, J. C. M., 1985, Morphological evolution of an emerging flux region, Sol. Phys., 96, 229–252

Buente, M., Solanki, S. K., Steiner, O., 1993, Centre-to-limb variation of the Stokes V asymmetry in solar magnetic flux tubes, Astron. Astrophys., 268, 736–748

Cameron, R., Schüssler, M., Vögler, A., Zakharov, V., 2007, Radiative magnetohydrodynamic simulations of solar pores, Astron. Astrophys., 474, 261–272

Carlsson, M., Stein, R. F., Nordlund, Å., Scharmer, G. B., 2004, Observational Manifestations of Solar Magnetoconvection: Center-to-Limb Variation, Astrophys. J. Lett., 610, L137–L140

Chaouche, L. Y., Abdelatif, T. E., 2005, MAG Waves in Sunspots Umbrae: Slow Waves Leaking to the Corona, Sol. Phys., 229, 255–271

Cheung, M., Schüssler, M., Tarbell, T., Title, A., 2008, Solar surface emerging flux regions: a comparative study of radiative MHD modeling and Hinode SOT observations, Astrophys. J. (Submitted)

Cheung, M. C. M., Schüssler, M., Moreno-Insertis, F., 2007, Magnetic flux emergence in granular convection: radiative MHD simulations and observational signatures, Astron. Astrophys., 467, 703–719

Cohen-Tannoudji, C., Dui, B., Laloe, F., 1973, Mecanique quantique, Collection Enseignement des Sciences, Paris: Herman

Danilovic, S., Gandorfer, A., Lagg, A., Schüssler, M., Solanki, S. K., Vögler, A., Katsukawa, Y., Tsuneta, S., 2008, The intensity contrast of solar granulation: comparing Hinode SP results with MHD simulations, Astron. Astrophys., 484, L17–L20

De Pontieu, B., 2002, High-Resolution Observations of Small-Scale Emerging Flux in the Photosphere, Astrophys. J., 569, 474–486

De Pontieu, B., Carlsson, M., Stein, R., Rouppe van der Voort, L., Löfdahl, M., van Noort, M., Nordlund, Å., Scharmer, G., 2006, Rapid Temporal Variability of Faculae: High-Resolution Observations and Modeling, Astrophys. J., 646, 1405–1420

Defouw, R. J., 1976, Wave propagation along a magnetic tube, Astrophys. J., 209, 266–269

del Toro Iniesta, J. C., 2003, Introduction to spectropolarimetry, Cambridge, UK: Cambridge University Press

Fan, Y., 2004, Magnetic Fields in the Solar Convection Zone, Living Reviews in Solar Physics, 1, 1–74. http://solarphysics.livingreviews.org

Fan, Y., Abbett, W. P., Fisher, G. H., 2003, The Dynamic Evolution of Twisted Magnetic Flux Tubes in a Three-dimensional Convecting Flow. I. Uniformly Buoyant Horizontal Tubes, Astrophys. J., 582, 1206–1219

Faurobert, M., Arnaud, J., Vigneau, J., Frisch, H., 2001, Investigation of weak solar magnetic fields. New observational results for the SrI 460.7 nm linear polarization and radiative transfer modeling, Astron. Astrophys., 378, 627–634

Faurobert-Scholl, M., Feautrier, N., Machefert, F., Petrovay, K., Spielfiedel, A., 1995, Turbulent magnetic fields in the solar photosphere: diagnostics and interpretation., Astron. Astrophys., 298, 289

Ferriz-Mas, A., Schüssler, M., 1989, Radial expansion of the magnetohydrodynamic equations for axiallysymmetric configurations, Geophysical and Astrophysical Fluid Dynamics, 48, 217–234

Ferriz-Mas, A., Schüssler, M., Anton, V., 1989, Dynamics of magnetic flux concentrations - The second-order thin flux tube approximation, Astron. Astrophys., 210, 425–432

Fligge, M., Solanki, S. K., 2001, The sun's variable spectrum and its terrestrial effects, Astronomical and Astrophysical Transactions, 20, 467–474

Fontenla, J. M., Avrett, E. H., Loeser, R., 1990, Energy balance in the solar transition region. I - Hydrostatic thermal models with ambipolar diffusion, Astrophys. J., 355, 700–718

Frazier, E. N., Stenflo, J. O., 1972, On the Small-Scale Structure of Solar Magnetic Fields, Sol. Phys., 27, 330–346

Frutiger, C., Solanki, S. K., 2001, Empirical models of solar magnetic flux-tubes and their non-magnetic surroundings, Astron. Astrophys., 369, 646–659

Frutiger, C., Solanki, S. K., Fligge, M., Bruls, J. H. M. J., 2000, Properties of the solar granulation obtained from the inversion of low spatial resolution spectra, Astron. & Astrophys., 358, 1109–1121

Frutiger, C., Solanki, S. K., Gandorfer, A., 2003, Magnetic Elements Near the Solar Limb: Inversions Based on a Flux-tube Model, vol. 307 of Astronomical Society of the Pacific Conference Series, p. 344

Galloway, D. J., Weiss, N. O., 1981, Convection and magnetic fields in stars, Astrophys. J., 243, 945–953

Gray, D. F., 2005, The Observation and Analysis of Stellar Photospheres, 3rd Edition, Cambridge University Press.

Grossmann-Doerth, U., Schüssler, M., Solanki, S. K., 1988, Unshifted, asymmetric Stokes V-profiles - Possible solution of a riddle, Astron. Astrophys., 206, L37–L39

Grossmann-Doerth, U., Schüssler, M., Solanki, S. K., 1989, Stokes V asymmetry and shift of spectral lines, Astron. Astrophys., 221, 338–341

Grossmann-Doerth, U., Keller, C. U., Schüssler, M., 1996, Observations of the quiet Sun's magnetic field., Astron. Astrophys., 315, 610–617

Grossmann-Doerth, U., Schüssler, M., Steiner, O., 1998, Convective intensification of solar surface magnetic fields: results of numerical experiments, Astron. Astrophys., 337, 928–939

Hale, G. E., 1908, On the Probable Existence of a Magnetic Field in Sun-Spots, Astrophys. J., 28, 315

Hansteen, V. H., Gudiksen, B., 2005, 3D Numerical Models of Quiet Sun Coronal Heating, in Solar Wind 11/SOHO 16, Connecting Sun and Heliosphere, vol. 592 of ESA Special Publication, p. 483

Harvey, J. W., 1977, Observations of Small-Scale Photospheric Magnetic Fields, Highlights of Astronomy, 4, 223

Hirzberger, J., Wiehr, E., 2005, Solar limb faculae, Astron. Astrophys., 438, 1059–1065

Howard, R., Stenflo, J. O., 1972, On the Filamentary Nature of Solar Magnetic Fields, Sol. Phys., 22, 402–417

Illing, R. M. E., Landman, D. A., Mickey, D. L., 1975, Broad-band circular polarization of sunspots - Spectral dependence and theory, Astron. Astrophys., 41, 183–185

Keller, C. U., Schüssler, M., Vögler, A., Zakharov, V., 2004, On the Origin of Solar Faculae, Astrophys. J. Lett., 607, L59–L62

Khomenko, E., Centeno, R., Collados, M., Trujillo Bueno, J., 2008, Channeling 5 Minute Photospheric Oscillations into the Solar Outer Atmosphere through Small-Scale Vertical Magnetic Flux Tubes, Astrophys. J. Lett., 676, L85–L88

Khomenko, E. V., Shelyag, S., Solanki, S. K., Vögler, A., 2005, Stokes diagnostics of simulations of magnetoconvection of mixed-polarity quiet-Sun regions, Astron. Astrophys., 442, 1059–1078

Kubo, M., Shimizu, T., Lites, B. W., 2003, The Evolution of Vector Magnetic Fields in an Emerging Flux Region, Astrophys. J., 595, 465–482

Lagg, A., Woch, J., Krupp, N., Solanki, S. K., 2004, Retrieval of the full magnetic vector with the He I multiplet at 1083 nm. Maps of an emerging flux region, Astron. & Astrophys., 414, 1109–1120

Landi degl'Innocenti, E., 1992, Magnetic field measurements, p. 71, Solar Observations: Techniques and Interpretation

Leka, K. D., Steiner, O., 2001, Understanding Small Solar Magnetic Structures: Comparing Numerical Simulations to Observations, Astrophys. J., 552, 354–371

Lites, B. W., 2005, Magnetic Flux Ropes in the Solar Photosphere: The Vector Magnetic Field under Active Region Filaments, Astrophys. J., 622, 1275–1291

Lites, B. W., Skumanich, A., 1990, Stokes profile analysis and vector magnetic fields. V - The magnetic field structure of large sunspots observed with Stokes II, Astrophys. J., 348, 747–760

Lites, B. W., Skumanich, A., Martinez Pillet, V., 1998, Vector magnetic fields of emerging solar flux. I. Properties at the site of emergence, Astron. & Astrophys., 333, 1053–1068

Lites, B. W., Scharmer, G. B., Berger, T. E., Title, A. M., 2004, Three-Dimensional Structure of the Active Region Photosphere as Revealed by High Angular Resolution, Sol. Phys., 221, 65–84

Lites, B. W., Kubo, M., Socas-Navarro, H., Berger, T., Frank, Z., Shine, R., Tarbell, T., Title, A., Ichimoto, K., Katsukawa, Y., Tsuneta, S., Suematsu, Y., Shimizu, T., Nagata, S., 2008, The Horizontal Magnetic Flux of the Quiet-Sun Internetwork as Observed with the Hinode Spectro-Polarimeter, Astrophys. J., 672, 1237–1253

Martínez Pillet, V., Lites, B. W., Skumanich, A., 1997, Active Region Magnetic Fields. I. Plage Fields, Astrophys. J., 474, 810

Mihalas, D., 1970, Stellar atmospheres, Series of Books in Astronomy and Astrophysics, San Francisco: Freeman.

Murray, M. J., Hood, A. W., 2008, Emerging flux tubes from the solar interior into the atmosphere: effects of non-constant twist, Astron. Astrophys., 479, 567–577

Nordlund, A., 1982, Numerical simulations of the solar granulation. I - Basic equations and methods, Astron. Astrophys., 107, 1–10

Nordlund, A., 1983, Numerical 3-D simulations of the collapse of photospheric flux tubes, in Solar and Stellar Magnetic Fields: Origins and Coronal Effects, (Ed.) J. O. Stenflo, vol. 102 of IAU Symposium, pp. 79–83

Nordlund, Å., Stein, R. F., 1990, Solar Magnetoconvection, in Solar Photosphere: Structure, Convection, and Magnetic Fields, (Ed.) J. O. Stenflo, vol. 138 of IAU Symposium, p. 191

Okamoto, T. J., Tsuneta, S., Lites, B. W., Kubo, M., Yokoyama, T., Berger, T. E., Ichimoto, K., Katsukawa, Y., Nagata, S., Shibata, K., Shimizu, T., Shine, R. A., Suematsu, Y., Tarbell, T. D., Title, A. M., 2008, Emergence of a Helical Flux Rope under an Active Region Prominence, Astrophys. J. Lett., 673, L215–L218

Okunev, O. V., Kneer, F., 2005, Numerical modeling of solar faculae close to the limb, Astron. Astrophys., 439, 323–334

Ossendrijver, M., 2003, The solar dynamo, Astron. Astrophys. Rev., 11, 287–367

Parker, E. N., 1978, Hydraulic concentration of magnetic fields in the solar photosphere. VI - Adiabatic cooling and concentration in downdrafts, Astrophys. J., 221, 368–377

Pneuman, G. W., Solanki, S. K., Stenflo, J. O., 1986, Structure and merging of solar magnetic fluxtubes, Astron. Astrophys., 154, 231–242

Rabin, D., 1992, Spatially extended measurements of magnetic field strength in solar plages, Astrophys. J., 391, 832–844

Rachkowsky, D. N., 1967, The reduction for anomalous dispersion in the theory of the absorption line formation in a magnetic field (in Russian), Izv. Krym. Astrofiz. Obs., 37, 56–61

Rees, D. E., Durrant, C. J., Murphy, G. A., 1989, Stokes profile analysis and vector magnetic fields. II - Formal numerical solutions of the Stokes transfer equations, Astrophys. J., 339, 1093–1106

Rezaei, R., Steiner, O., Wedemeyer-Böhm, S., Schlichenmaier, R., Schmidt, W., Lites, B. W., 2007, Hinode observations reveal boundary layers of magnetic elements in the solar photosphere, Astron. Astrophys., 476, L33–L36

Roberts, B., Webb, A. R., 1978, Vertical motions in an intense magnetic flux tube, Sol. Phys., 56, 5–35

Roberts, B., Webb, A. R., 1979, Vertical motions in an intense magnetic flux tube. III - On the slender flux tube approximation, Sol. Phys., 64, 77–92

Rüedi, I., Solanki, S. K., Livingston, W., Stenflo, J. O., 1992, Infrared lines as probes of solar magnetic features. III - Strong and weak magnetic fields in plages, Astron. Astrophys., 263, 323–338

Rutten, R. J., 2003, Utrecht Radiative Transfer Courses, in Stellar Atmosphere Modeling, (Eds.) I. Hubeny, D. Mihalas, K. Werner, vol. 288 of Astronomical Society of the Pacific Conference Series, p. 99

Schüssler, M., 1990, Theoretical Aspects of Small-Scale Photospheric Magnetic Fields, in Solar Photosphere: Structure, Convection, and Magnetic Fields, (Ed.) J. O. Stenflo, vol. 138 of IAU Symposium, p. 161

Schüssler, M., 1992, Small-Scale Photospheric Magnetic Fields, in NATO ASIC Proc. 373: The Sun: A Laboratory for Astrophysics, (Eds.) J. T. Schmelz, J. C. Brown, p. 191

Schüssler, M., 2001, Numerical Simulation of Solar Magneto-Convection, in Advanced Solar Polarimetry – Theory, Observation, and Instrumentation, (Ed.) M. Sigwarth, vol. 236 of Astronomical Society of the Pacific Conference Series, p. 343

Schüssler, M., Knölker, M., 2001, Magneto-Convection, in Magnetic Fields Across the Hertzsprung-Russell Diagram, (Eds.) G. Mathys, S. K. Solanki, D. T. Wickramasinghe, vol. 248 of Astronomical Society of the Pacific Conference Series, p. 115

Schüssler, M., Vögler, A., 2006, Magnetoconvection in a Sunspot Umbra, Astrophys. J. Lett., 641, L73–L76

Schüssler, M., Vögler, A., 2008, Strong horizontal photospheric magnetic field in a surface dynamo simulation, Astron. Astrophys., 481, L5–L8

Schüssler, M., Shelyag, S., Berdyugina, S., Vögler, A., Solanki, S. K., 2003, Why Solar Magnetic Flux Concentrations Are Bright in Molecular Bands, Astrophys. J. Lett., 597, L173–L176

Seares, F. H., 1913, The Displacement-Curve of the Sun's General Magnetic Field, Astrophys. J., 38, 99

Shelyag, S., Schüssler, M., Solanki, S. K., Berdyugina, S. V., Vögler, A., 2004, G-band spectral synthesis and diagnostics of simulated solar magneto-convection, Astron. Astrophys., 427, 335–343

Shibata, K., Tajima, T., Steinolfson, R. S., Matsumoto, R., 1989, Two-dimensional magnetohydrodynamic model of emerging magnetic flux in the solar atmosphere, Astrophys. J., 345, 584–596

Sigwarth, M., 2000, Dynamics of Solar Magnetic Fields – A Spectroscopic Investigation, Reviews of Modern Astronomy, 13, 45

Sigwarth, M., Balasubramaniam, K. S., Knölker, M., Schmidt, W., 1999, Dynamics of solar magnetic elements, Astron. Astrophys., 349, 941–955

Skumanich, A., Lites, B. W., 1987, Stokes profile analysis and vector magnetic fields. I - Inversion of photospheric lines, Astrophys. J., 322, 473–482

Sobel'man, I. I., 1972, Introduction to the Theory of Atomic Spectra, Pergamon Press, London

Solanki, S. K., 1986, Velocities in solar magnetic fluxtubes, Astron. Astrophys., 168, 311–329

Solanki, S. K., 1987, The Photospheric Layers of Solar Magnetic Flux Tubes, Ph.D. Thesis

Solanki, S. K., 1989, The origin and the diagnostic capabilities of the Stokes V asymmetry observed in solar faculae and the network, Astron. Astrophys., 224, 225–241

Solanki, S. K., 1993, Smallscale Solar Magnetic Fields - an Overview, Space Science Reviews, 63, 1–188

Solanki, S. K., 2001, Small-scale Photospheric Structure of the Solar Magnetic Fields outside Sunspots, in Magnetic Fields Across the Hertzsprung-Russell Diagram, (Eds.) G. Mathys, S. K. Solanki, D. T. Wickramasinghe, vol. 248 of Astronomical Society of the Pacific Conference Series, p. 45

Solanki, S. K., 2003, Sunspots: An overview, Astron. Astrophys. Rev., 11, 153–286

Solanki, S. K., Pahlke, K. D., 1988, Can stationary velocity fields explain the Stokes V asymmetry observed in solar magnetic elements?, Astron. Astrophys., 201, 143–152

Solanki, S. K., Stenflo, J. O., 1985, Models of solar magnetic fluxtubes - Constraints imposed by Fe I and II lines, Astron. Astrophys., 148, 123–132

Solanki, S. K., Steiner, O., Uitenbroeck, H., 1991, Two-dimensional models of the solar chromosphere. I - The CA II K line as a diagnostic: 1.5-D radiative transfer, Astron. Astrophys., 250, 220–234

Solanki, S. K., Steiner, O., Bünte, M., Murphy, G., Ploner, S. R. O., 1998, On the reliability of Stokes diagnostics of magnetic elements away from solar disc centre, Astron. Astrophys., 333, 721–731

Solanki, S. K., Inhester, B., Schüssler, M., 2006, The solar magnetic field, Reports on progress in physics, 69, 563Ű668

Spruit, H. C., 1979, Convective collapse of flux tubes, Sol. Phys., 61, 363–378

Spruit, H. C., 1981, Equations for thin flux tubes in ideal MHD, Astron. Astrophys., 102, 129–133

Spruit, H. C., Roberts, B., 1983, Magnetic flux tubes on the sun, Nature, 304, 401–406

Stein, R. F., Nordlund, A., 1998, Simulations of Solar Granulation. I. General Properties, Astrophys. J., 499, 914

Stein, R. F., Nordlund, Å., 2003, Radiative Transfer in 3D Numerical Simulations, in Stellar Atmosphere Modeling, (Eds.) I. Hubeny, D. Mihalas, K. Werner, vol. 288 of Astronomical Society of the Pacific Conference Series, p. 519

Steiner, O., 2000, The formation of asymmetric Stokes V profiles in the presence of a magnetopause, Sol. Phys., 196, 245–268

Steiner, O., 2005, Radiative properties of magnetic elements. II. Center to limb variation of the appearance of photospheric faculae, Astron. Astrophys., 430, 691–700

Stenflo, J. O., 1973, Magnetic-Field Structure of the Photospheric Network, Sol. Phys., 32, 41–63

Stenflo, J. O. (Ed.), 1994, Solar magnetic fields: polarized radiation diagnostics, vol. 189 of Astrophysics and Space Science Library

Stenflo, J. O., Solanki, S. K., Harvey, J. W., 1987, Center-to-limb variation of Stokes profiles and the diagnostics of solar magnetic fluxtubes, Astron. Astrophys., 171, 305–316

Strous, L. H., 1994, Dynamics in Solar Active Regions: Patterns in Magnetic-Flux Emergence, Ph.D. thesis, Utrecht University.

Strous, L. H., Zwaan, C., 1999, Phenomena in an Emerging Active Region. II. Properties of the Dynamic Small-Scale Structure, Astrophys. J., 527, 435–444

Strous, L. H., Scharmer, G., Tarbell, T. D., Title, A. M., Zwaan, C., 1996, Phenomena in an emerging active region. I. Horizontal dynamics., Astron. Astrophys., 306, 947

Thomas, J. H., Weiss, N. O. (Eds.), 1992, Sunspots: Theory and observations; Proceedings of the NATO Advanced Research Workshop on the Theory of Sunspots, Cambridge, United Kingdom, Sept. 22-27, 1991

Thompson, M. J., Christensen-Dalsgaard, J., Miesch, M. S., Toomre, J., 2003, The Internal Rotation of the Sun, Annual Rev. Astron. Astrophys., 41, 599–643

Trujillo Bueno, J., Shchukina, N., Asensio Ramos, A., 2004, A substantial amount of hidden magnetic energy in the quiet Sun, Nature, 430, 326–329

Unno, W., 1956, Line Formation of a Normal Zeeman Triplet, Publications of the Astronomical Society of Japan, 8, 108–125

van Noort, M., Rouppe van der Voort, L., Löfdahl, M. G., 2005, Solar Image Restoration By Use Of Multi-frame Blind De-convolution With Multiple Objects And Phase Diversity, Sol. Phys., 228, 191–215

Vernazza, J. E., Avrett, E. H., Loeser, R., 1973, Structure of the Solar Chromosphere. Basic Computations and Summary of the Results, Astrophys. J., 184, 605–632

Vernazza, J. E., Avrett, E. H., Loeser, R., 1976, Structure of the solar chromosphere. II - The underlying photosphere and temperature-minimum region, Astrophys. J. Suppl. Series, 30, 1–60

Vögler, A., 2003, Three-dimensional simulations of magneto-convection in the solar photosphere, PhD thesis, Universität Göttingen

Vögler, A., Schüssler, M., 2003, Studying magneto-convection by numerical simulation, Astronomische Nachrichten, 324, 399–404

Vögler, A., Schüssler, M., 2007, A solar surface dynamo, Astron. Astrophys., 465, L43–L46

Vögler, A., Shelyag, S., Schüssler, M., Cattaneo, F., Emonet, T., Linde, T., 2005, Simulations of magneto-convection in the solar photosphere. Equations, methods, and results of the MURaM code, Astron. & Astrophys., 429, 335–351

Weiss, N. O., 1966, The Expulsion of Magnetic Flux by Eddies, Royal Society of London Proceedings Series A, 293, 310–328

Wiehr, E., 1978, Concerning the existence of a lower limit of solar magnetic fields, Mitteilungen der Astronomischen Gesellschaft Hamburg, 43, 134–136

Yelles Chaouche, L., Solanki, S. K., Rouppe van der Voort, L., van Noort, M., 2008, Spectropolarimetric diagnostics at the solar photosphere near the limb, in 5th Solar Polarization Workshop, Astronomical Society of the Pacific Conference Series, (Submitted)

Zakharov, V., 2006, Diagnostic of the solar photosphere with high spatial resolution using CH, CN and continuum spectral bands, PhD thesis, Universität Göttingen

Zwaan, C., 1987, Elements and patterns in the solar magnetic field, Annual Rev. Astron. Astrophys., 25, 83–111

Zwaan, C., Brants, J. J., Cram, L. E., 1985, High-resolution spectroscopy of active regions. I - Observing procedures, Sol. Phys., 95, 3–14

Acknowledgements

I would like to address my sincere thanks to my supervisor Sami Solanki for his guidance and support through this thesis. I am indebted to him for all the great science I learned through our discussions and stimulating interaction.
I wish to thank my university supervisor Franz Kneer for all his help and for all the lively discussions during the group's seminars and beyond.
Very special thanks to my second supervisor Manfred Schüssler for the zillions of things I learned from him and for the great environment in the MHD group.
I would like to thank my supervisors for offering me a stimulating environment and a great day-by-day scientific and human experiences.
Thanks to the MHD tribe for many many things I learned and shared with them, and for all the fun we have in this group ...TGIF Yes!
A special hearty hug to all the friends...Thanks to you, the last three and half years have been full of great experiences!
Special thanks to Dieter Schmitt. I will never forget two things : Dieter's reassuring face just before my interview at the IMPRS, and the second thing and not the least is the IMPRS retreats...Thanks Dieter!

Lebenslauf

Name:	Lotfi Yelles Chaouche
Geburt:	18.02.1976 in Tlemcen, Algerien
Staatsangehörigkeit:	Algerisch
Schulbildung:	10/1990 bis 06/1993: Lycee Ahmed ben Zekri, Tlemcen
Studium:	10/1993 bis 07/1998: Physikstudium an der Universität in Tlemcen D.E.S. (High Studies Diploma in physics) 11/1999 bis 01/2004: Master in Physik an der Universität in Tlemcen 01/2005 bis 01/2008: Doktorand der International Max Planck Research School on Physical Processes in the Solar System and Beyond, am Max-Planck-Institut für Sonnensystemforschung in Katlenburg-Lindau